THE ORDER-DISORDER TRANSFORMATION AND MICROSTRUCTURE EVOLUTION IN NICKEL-ALUMINIUM INTERMETALLICS AFTER HEAVY-ION IRRADIATION

THÈSE N° 2281 (2000)

PRÉSENTÉE AU DÉPARTEMENT DE PHYSIQUE

ÉCOLE POLYTECHNIQUE FÉDÉRALE DE LAUSANNE

POUR L'OBTENTION DU GRADE DE DOCTEUR ÈS SCIENCES

PAR

Pedro Miguel RODRIGUES DE ALMEIDA

Ingénieur physicien, Université Technique, Lisbonne, Portugal
de nationalité portugaise

acceptée sur proposition du jury:

Dr M. Victoria, directeur de thèse
Dr C. Abromeit, rapporteur
Dr M. Döbeli, rapporteur
Prof. F. Lévy, rapporteur
Dr R. Schäublin, rapporteur
Prof. M. Q. Tran, rapporteur

Lausanne, EPFL
2000

Dedicado a meu pai, por ter sido sempre quem mais longe viu.

(24/03/2000)

In memoriam.

(16/04/2000)

L'unico vero realista è il visionario.

— *F. F.*

Abstract

Nickel-aluminium intermetallics constitute interesting systems for the study of irradiation-induced phase transformations (order $\rightarrow$ disorder, amorphization) and production of defects. Irradiation of ordered intermetallics may induce disorder or amorphization depending on the projectile characteristics, irradiation conditions and chemical and physical properties of the target. The behavior of the various intermetallic compounds of the nickel-aluminium system with respect to electron and ion irradiation has been extensively studied in the recent past. In more recent years, however, significant interest has driven the motivation for modelling these processes using molecular dynamics computer simulations. These results have demonstrated the feasibility of simulating cascade damage in pure metals and intermetallics and led to the partial corroboration of phenomenological data which has been compiled from a set of experiments. In this frame, and in spite of the numerous efforts previously done, little information has been collected in order to perform a comparative study on the behavior of NiAl and Ni_3Al under heavy-ion irradiation in a consistent approach. The present study reports on:

- the synthesis of stoichiometric and ordered intermetallic thin films as proper irradiation media, which has evolved into a subject of substantial complexity. It is remarkable, nevertheless, that very few systems have been studied regarding the microstructure and growth modes of intermetallics on metallic substrates. In this context, the granular-heteroepitaxial inverse Nishiyama-Wassermann $(\bar{2}11)[\bar{2}11]_{B2} \parallel (\bar{1}10)[\bar{1}10]_{fcc}$ and the heteroepitaxial $(\bar{1}10)[\bar{1}10]_{L1_2} \parallel (\bar{1}10)[\bar{1}10]_{fcc}$ relationships have been lately demonstrated for NiAl and Ni_3Al grown onto nickel single-crystals at high temperature, respectively. Inherent to the deposition technique, and at the low substrate temperature regime, is the formation of defect structures and polycrystalline materials which are not the most convenient for post-irradiation microstructure assessment. Therefore, special attention has been given to bulk single-crystals which have been irradiated and prepared in cross-section for transmission electron microscopy observations;

- the numerical link between previous molecular dynamics results and current transmission electron microscopy image simulation, in order to establish under cascade damage conditions which type of defects are created and how do NiAl and Ni_3Al intermetallics compare regarding the effect of primary ion energy and damage accumulation. The former has been seen to undergo an amorphous transformation upon a 15 keV-nickel recoil, which has not been registered for the latter. These results have been valuable in order to understand structural differences under cascade damage production and to validate molecular dynamics computer simulations from a microscopist point of view;

and

- the microstructure investigation using transmission electron microscopy of heavy-ion irradiated NiAl and Ni₃Al samples, thus establishing a set of physical parameters (defect visibility, disordered zone and defect densities, and respective mean sizes) to be directly compared in a self-consistent approach to the results obtained through image simulation of damaged intermetallics. A direct crystalline-to-amorphous transformation has been seen not to occur either at liquid nitrogen or room temperature for the former intermetallic, as predicted from molecular dynamics results. Instead, a defect accumulation driven mechanism should be active. Microstructural evolution under heavy-ion irradiation must be thought on the basis of the disordered zone to defect cluster densities ratio, ρ_d/ρ_c, in order to compare both intermetallics in a self-consistent approach due to different fluences (or doses), and primary ion energies. Being ρ_d/ρ_c an estimator of irradiation-induced disordering efficiency, it is now arguable that at the high energy regime this ratio decreases with increasing primary ion energy. Aronin's exponential law $S = S_0\exp(-\varepsilon\Phi)$, which is characterized by the initial long-range order value S_0, the dose in dpa Φ, and the disordering efficiency ε, does not explicit any knowledge on the nature of ε. This parameter has been measured for 6 MeV-nickel primary ions in Ni₃Al, yielding a value in the range of 10.0±0.7 /dpa. Further research must be undertaken in order to establish an experimental value for equivalent irradiation conditions in NiAl. The disordering efficiency ε is certainly a function of the disordered zone to defect cluster densities ratio, $\varepsilon = f(\rho_d/\rho_c)$. Further validation of such a relation would be of paramount importance in order to understand irradiation-induced disordering at high primary ion energies and to establish the fact that a less effective disordering process takes place in a regime of dominant subcascade formation.

Résumé

Les intermétalliques nickel-aluminium constituent des systèmes intéressants pour l'étude des transformations de phase telles que la transition ordre $\rightarrow$ désordre ou l'amorphisation et la production de défauts. L'irradiation d'intermétalliques ordonnés peut induire du désordre ou une amorphisation selon les caractéristiques du projectile, les conditions d'irradiation et les propriétés chimiques et physiques de la cible. Le comportement des différents composés intermétalliques du système nickel-aluminium sous irradiation électronique et ionique a été étudié de manière extensive par le passé. Dans les dernières années cependant, un fort intérêt a conduit à la modélisation de ces processus par l'utilisation de simulations en dynamique moléculaire. Ces résultats ont démontré la faisabilité de la simulation de la cascade de défauts dans les métaux purs et dans les intermétalliques et a conduit à la corroboration partielle des données phénoménologiques qui ont été compilées à partir d'un ensemble d'expériences. Dans ce cadre, et malgré les nombreux efforts effectués jusqu'ici, peu d'information a été collectée dans le dessein d'effectuer une étude comparative dans le comportement de NiAl et de Ni_3Al sous irradiation d'ions lourds selon une approche consistante. La présente étude reporte sur:

- La synthèse de couches minces intermétalliques ordonnés et stoechiométriques comme cible de l'irradiation, qui a évolué au long de ce travail comme un sujet d'une complexité substantielle. Il est remarquable cependant que si peu de systèmes aient été étudiés à propos de leurs microstructures et leurs modes de croissance sur substrat métallique. Dans ce contexte, les relations cristallographiques hétéroépitaxiale inverse de Nishiyama-Wassermann $(\bar{2}11)[\bar{2}11]_{B2} \parallel (\bar{1}10)[\bar{1}10]_{fcc}$ et hétéroépitaxiale simple de type $(\bar{1}10)[\bar{1}10]_{L1_2} \parallel (\bar{1}10)[\bar{1}10]_{fcc}$ ont été démontrées pour NiAl et Ni_3Al dans leur croissance sur des monocristaux de nickel, respectivement. Malheureusement, ce type de déposition à ces régimes de température de substrat relativement basses conduit à une structure de défauts et à une polycristallinité du matériau qui n'est pas des plus adaptée pour l'étude de la microstructure de dégâts induits par irradiation. C'est pourquoi par la suite une attention particulière a été apportée à l'étude de monocristaux massifs qui ont été irradiés et préparés en section transverse pour l'observation en microscopie électronique à transmission;

- Le lien entre les résultats de simulations en dynamique moléculaire et la microscopie électronique à transmission à travers des simulations d'image, afin d'établir quels types de défauts sont créés sous irradiation et comment les intermétalliques NiAl et Ni_3Al peuvent être comparés par rapport à l'effet de l'énergie primaire des ions et de l'accumulation des défauts. NiAl a présenté une amorphisation lors d'un impact de Ni à 15 keV qui n'a pas été observée dans Ni_3Al. Ces résultats sont très intéressants pour comprendre les différences de réponse structurale entre ces deux matériaux

sous production de défauts par cascade et pour valider les résultats de dynamique moléculaire d'un point de vue microscopiste;

et

- L'investigation de la microstructure avec la microscopie électronique à transmission d'échantillons de NiAl et de Ni_3Al irradiés avec des ions lourds, établissant ainsi un ensemble de paramètres physiques (visibilité des défauts, densité des zones désordonnées et des défauts, et taille moyenne respective) à comparer dans une approche consistante aux résultats des intermétalliques endommagés à travers des simulations d'images. Il apparaît qu'une transition directe cristal-amorphe dans NiAl n'a pas lieu que ce soit à l'azote liquide ou à température ambiante, mais qu'elle est plutôt due à un mécanisme d'accumulation de défauts. L'évolution microstructurale sous irradiation peut être envisagée à travers le rapport entre la densité de zones désordonnées et la densité d'agglomérats de défauts, ρ_d/ρ_c, afin de comparer les deux intermétalliques selon une approche comparable au vu de la différence des fluences, et donc des doses, et de l'énergie primaire des ions. Ce rapport est donc considéré comme un estimateur de l'efficacité du désordre induit par irradiation. Il peut être argué cependant que, dans le régime des hautes énergies, ce rapport décroît lorsque l'énergie primaire des ions croît. La loi exponentielle d'Aronin $S = S_0 \exp(-\varepsilon \Phi)$, qui est caractérisée par la valeur initiale du désordre S_0, la dose en dpa Φ, et l'efficacité de désordre ε ne rend pas compte explicitement sur la nature d'epsilon. Ce paramètre a été mesuré pour le Ni_3Al irradiés avec des ions de nickel de 6 MeV, donnant une valeur de 10.0±0.7 /dpa. Des recherches doivent être conduites maintenant afin d'établir la valeur expérimentale pour NiAl dans des conditions d'irradiation équivalentes. L'efficacité de désordre ε est certainement une fonction du rapport entre la densité de zones désordonnées et la densité d'agglomérats de défauts, $\varepsilon = f(\rho_d/\rho_c)$. Une validation d'une telle relation serait essentielle afin de comprendre le désordre induit par irradiation par des ions de haute énergie et pour établir le fait qu'un processus moins efficace de désordre apparaît dans ce régime d'énergie dominé par la formation de sous-cascades.

Contents

Chapter 1

Introduction

1.1   Intermetallic compounds

An intermetallic is a compound of two or more elements which have a strong affinity for each other. Although the bonding is still metallic in nature there is an additional ionic character that is due to the electronegativity difference between the different elements. In the extreme case where the added element is a strongly electronegative non-metal (sulphur, oxygen, chlorine), a true chemical compound is formed and the material no longer possesses the metallic qualities of an alloy (Cottrell 1962).

The attraction between dissimilar atoms induces the crystal to adopt a structure that accommodates the atomic bonding preferences. An intermetallic compound is a phase which crystallizes with a structure different than that of their components (Girgis 1983) and does not have a range of homogeneity extending to a pure component, thus they are described as intermediate phases. It is possible to differentiate between two types of intermetallic compounds, Berthollides and Daltonides. The former are intermetallic phases with a certain range of homogeneity where the point position is not restricted to one of the atomic species. The latter are intermetallic phases without any homogeneity range, thus each point position is occupied by only one atomic species. In principle, intermetallics need not have anything in common with the properties of the composing elements (Buschow 1977).

The atomic arrangements in intermetallic compounds are called ordered structures, meaning that each element has a preferred position in the crystal structure. An ordered distribution of the different atomic species over the lattice sites prompts the formation of two or more interpenetrating sublattices, resulting in a larger unit cell or superlattice (Cottrell 1962).

1

1.2 Ordered arrangements of atoms

The study of the relationship between order in a system and its physical properties is of great theoretical and practical importance (Bragg & Williams 1934, Bethe & Wills 1935, Bragg & Williams 1935, Birchenall 1952, Corey & Lisowsky 1967, Hughes et al. 1971, Aoki & Izumi 1975, Visnov et al. 1980). In an equilibrium system the main ordering mechanism is provided by the interatomic cohesive forces and the major disordering sources arise from thermal energy.

In a perfect crystal of a pure material it is possible to identify the position of the nearest neighbors of any central atom with certainty and to specify the position of sites many hundreds of atomic distances away. The introduction of a second type of element into the system increases its complexity, being it then possible to distinguish several system cases (Birchenall 1952). The specific case of superlattice formation, when the two types of atoms segregate to distinguishable sets of sites which themselves constitute interpenetrating sublattices, giving rise either to a B2 (Figure 1.1(a)) or L1$_2$ (Figure 1.1(b)) structure, will be referred here.
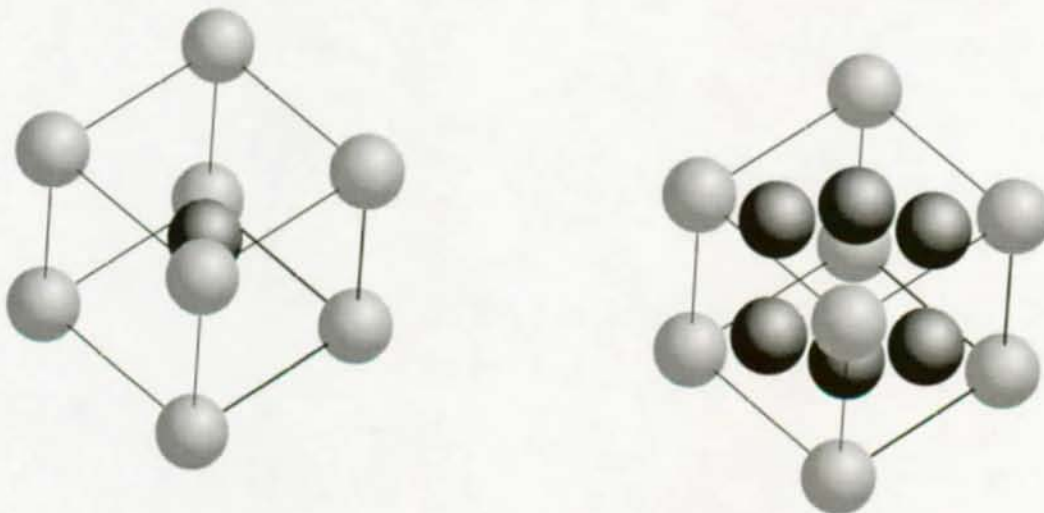
(a) B2

(b) L1$_2$

Figure 1.1: Atomic arrangements in generic (a) AB and (b) A$_3$B compounds with superlattice structures of type B2 and L1$_2$, respectively. Dark spheres represent A atoms and light spheres represent B atoms.

In a periodic lattice ω we might define the degree of long-range order S as:

$$S = \frac{P_{X\omega} - c_X}{1 - c_X} \qquad (1.1)$$

where $P_{X\omega}$ is the probability that an ω position is occupied by an element of type X, and c_X its atomic concentration (Bragg & Williams 1934).

The solution of equation 1.1 for the B2 structure (generic AB compound) determines the following set of probability distributions as functions of S:

$$P_{A\alpha} = \frac{1+S}{2}, \ P_{B\beta} = \frac{1+S}{2}, \ P_{A\beta} = \frac{1-S}{2}, \ P_{B\alpha} = \frac{1-S}{2} \qquad (1.2)$$

where α and β are the sublattices of the atomic species A and B. This set of probability distributions is plotted in Figure 1.2. It is worth to note that $P_{A\alpha} = P_{B\beta}$ and that $P_{A\beta} = P_{B\alpha}$, which means that the α and β sublattices are equivalent.

For the L1$_2$ structure (generic A$_3$B compound), the solution of equation 1.1 determines the following set of distributions:

$$P_{A\alpha} = \frac{3+S}{4}, \ P_{B\beta} = \frac{1+3S}{4}, \ P_{A\beta} = \frac{3-3S}{4}, \ P_{B\alpha} = \frac{1-S}{4}. \qquad (1.3)$$

This set of probability distributions is plotted in Figure 1.3. It is worth to note that $P_{A\alpha} \neq P_{B\beta}$ and that $P_{A\beta} \neq P_{B\alpha}$, which means that the α and β sublattices are not equivalent.

Let P_m^{AB} be the fraction of sites in the mth shell round an A atom occupied by B atoms. We might define the degree of short-range order α_m as:

$$\alpha_m = \frac{P_m^{AA} - c_A}{1 - c_A} \qquad (1.4)$$

where P_m^{AA} is the fraction of atoms of type A surrounded by an element of the same species in the mth shell, and c_A its atomic concentration (Haasen 1996).

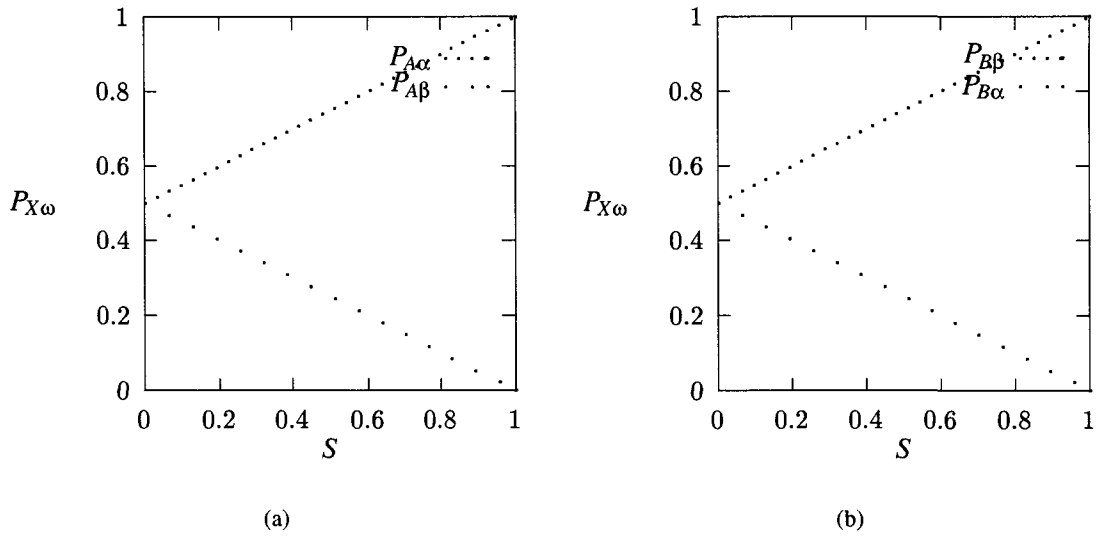(a)   (b)

Figure 1.2: $P_{X\omega}$ distributions (a) $P_{A\alpha}$, $P_{A\beta}$ and (b) $P_{B\beta}$, $P_{B\alpha}$ for the B2 superlattice.
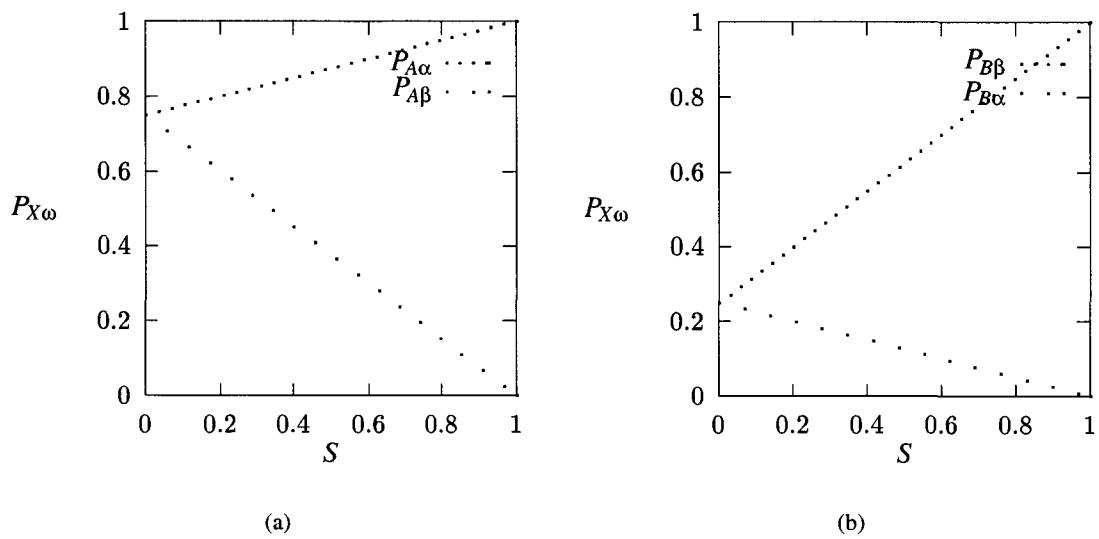

(a)   (b)

Figure 1.3: $P_{X\omega}$ distributions (a) $P_{A\alpha}$, $P_{A\beta}$ and (b) $P_{B\beta}$, $P_{B\alpha}$ for the L1$_2$ superlattice.

In the special case of nearest neighbors, $m = 1$, the sign of α_1 determines limiting cases of the atomic configuration:

$$\alpha_1 = 0, \quad P_1^{AA} = c_A \quad \text{statistical arrangement of nearest neighbors;}$$

$$\alpha_1 = 1, \quad P_1^{AA} = 1 \quad \text{statistical clustering;}$$

$$\alpha_1 \leq 0, \quad P_1^{AA} = 0 \quad \text{perfect short-range order.}$$

In the ordered B2 structure the concentration of both atomic species is equal and both sublattices are equivalent; each atom is surrounded by eight first neighbors of opposite type. In the ordered L1$_2$ structure the concentration of the atomic species is given by the stoichiometric coefficients of the compound. The sublattices are not equivalent and an atom of type A has 8 A and 4 B type nearest neighbors whereas a B atom has 12 A type nearest neighbors.

In a random distribution the B2 superlattice would reduce to a body centered cubic (bcc) structure in which each site is filled either by atoms of type A or B at equal probability. In this type of structure any atom has 4 A and 4 B type nearest neighbors. Likewise, the L1$_2$ superlattice would reduce to a face centered cubic (fcc) structure in which each site is occupied according to a probability proportional to the compound stoichiometry. In this type of arrangement all the atoms have 9 A and 3 B type nearest neighbors.

The particular solutions α_1 of equation 1.4 for the limiting cases of $S = 1$ and $S = 0$ in a B2 structure are $\alpha_1 = -1$ and $\alpha_1 = 0$, respectively. In a similar way, and for the same limiting cases in a structure of type L1$_2$, these values are $\alpha_1 = -1/3$ and $\alpha_1 = 0$.

1.3 Detection of order: F-contrast method

As the long-range order parameter S is proportional to the geometrical structure factor of the unit cell and therefore to the intensity of superlattice reflections (Jenkins et al. 1976, Jenkins & English 1982, English & Jenkins 1987), a quantification is possible by evaluating the ratio of selected superlattice and fundamental reflections (Müller 1997, Ewert 1998).

The geometrical structure factor F_{hkl} is defined as:

$$F_{hkl} = \sum_j f_j \exp\left[-i2\pi(u_j h + v_j k + w_j l)\right] \tag{1.5}$$

where f_j is the scattering power of the jth atom, $(u_j v_j w_j)$ its position in the unit cell, and (hkl) a set of reflections for a given crystal lattice (Kittel 1966). This factor need not be a real value for the intensity of the scattered wave involves only the product of the geometrical structure factor and its complex conjugate.

If the kinematical theory, which assumes that the amplitude of scattered waves is a small fraction of the incident wave, holds and the exact Bragg reflection condition is suitable for both a superlattice and a fundamental reflection, then the long-range order parameter S might be derived from the geometrical structure factor exactly.

The solution of equation 1.5 for the B2 structure (generic AB compound) is derived as follows:

$$F_{hkl} = S(f_B - f_A) \quad \text{when } h+k+l = \text{odd integer;}$$
$$F_{hkl} = f_B + f_A \quad \text{when } h+k+l = \text{even integer.}$$

For this structure, the long-range order parameter S is given by:

$$S^2 = \left(\frac{f_B + f_A}{f_B - f_A}\right)^2 \frac{I_s}{I_f} \tag{1.6}$$

where I_s and I_f are the intensities of the superlattice and fundamental reflections, and f_A and f_B the scattering power of the atoms A and B, respectively.

In a similar way, the solution of equation 1.5 for the L1$_2$ structure (A$_3$B compound) is derived as follows:

$$F_{hkl} = S(f_B - f_A) \quad \text{when } hkl \text{ have mixed parity;}$$
$$F_{hkl} = f_B + 3f_A \quad \text{when } hkl \text{ have the same parity.}$$

For this structure, the long-range order parameter S is given by:

$$S^2 = \left(\frac{f_B + 3f_A}{f_B - f_A}\right)^2 \frac{I_s}{I_f} \tag{1.7}$$

where I_s and I_f are the intensities of the superlattice and fundamental reflections, and f_A and f_B the scattering power of the atoms A and B, respectively.

These values are found on the basis of the F-contrast method which is of paramount importance in detecting contrast between ordered and disordered material (Schulson 1979). Quantitative examination of disordering with a cooled CCD camera attached to a transmission electron microscope has been successfully reported (Kimoto & Saito 1994).

1.4 Radiation damage

When incident upon a crystalline target, an energetic particle colliding with a lattice atom transfers kinetic energy. The atom which receives this energy is termed the primary knock-on atom (PKA). If the kinetic energy is sufficiently large, typically of 25 eV, the PKA is dislodged from its normal lattice site, leaving a vacancy and forming an interstitial. This pair of point defects is called a Frenkel defect. If energetic enough, the PKA may cause secondary knock-on events. The whole process, from the formation of the PKA to the dissipation of the kinetic energy to a level below which Frenkel defects are no longer produced, is termed a displacement or collision cascade.

Upon creation, the cascade region is comprised of undisplaced atoms, vacancies and of interstitials. The vacancies are concentrated more or less within the core, called the depleted zone, and the interstitials, within the periphery. The cascade occurs within approximately 1 ps, and the deposited kinetic energy is dissipated within 10 ps. The kinetic energy of the atoms in the cascade effectively increases the volume within which spontaneous vacancy/interstitial recombination occurs. This effect results in a defect production efficiency less than unity. If the moving interstitial has insufficient kinetic energy to escape from the vacancy left by the knocked-on atom, then a replacement collision might occur, so termed because it changes the identity of the displaced atoms, but not the total number. Under fast-neutron and heavy-ion irradiation, replacement collisions outnumber displacement collisions. Replacement collisions occur both within the cascade region and beyond the perimeter. In the latter case, a focused replacement collision sequence, termed a dynamic crowdion, might occur, resulting in interstitial atoms traveling large distances in relation to the size of the cascade region.

In analyzing the behavior of reactor materials, it is necessary to know the rate at which the atoms of a target are displaced from their lattice positions (Norgett et al. 1975). The number of Frenkel pairs N_d generated in the collisional phase of the cascade is given by:

$$N_d = \frac{\kappa(E - \widehat{Q})}{2E_d} = \frac{\kappa\widehat{E}}{2E_d} \tag{1.8}$$

where E is the energy of the PKA, $\widehat{Q}$ the total energy lost in the cascade by electron excitation, $\widehat{E}$ the damage energy available for atomic displacement, and κ is a constant independent of energy (except for E near $2E_d$), insensitive to the target material and temperature, approximately equal to 0.8 (Robinson & Torrens 1974, Norgett et al. 1975). It should be noted, however, that due to a recombination mechanism the number of Frenkel defect pairs that actually survive in the initial cascade event is considerably less than the calculated number.

Collision cascades occur at various points within a target when exposed to a flux of energetic particles. Initially, the resulting cascades are separate entities, and their number density increases linearly with fluence. Eventually, these regions overlap and then essentially fill in the irradiated volume. At this stage, it becomes appropriate to evaluate the number of times each atom has been displaced, or displacements per atom (dpa), rather than displacements per cascade. The number of displacements per atom G is defined as:

$$G = N_d \sigma_s \phi t \tag{1.9}$$

where N_d is the number of Frenkel defect pairs generated per cascade, σ_s the scattering cross-section, ϕ the flux of incoming particles, and t the irradiation time.

The displacement rate K is defined as:

$$K = \frac{G}{N_d \sigma_s t} \tag{1.10}$$

and consequently equation 1.9 can be rewritten in the equivalent form:

$$\Phi = Kt \tag{1.11}$$

where Φ is the irradiation fluence, K the displacement rate as defined in equation 1.10, and t the irradiation time.

From a fundamental point of view, the study of radiation damage in intermetallics offers an interesting challenge. Anti-site defects need to be considered in addition to Frenkel defect pairs (Figure 1.4). A
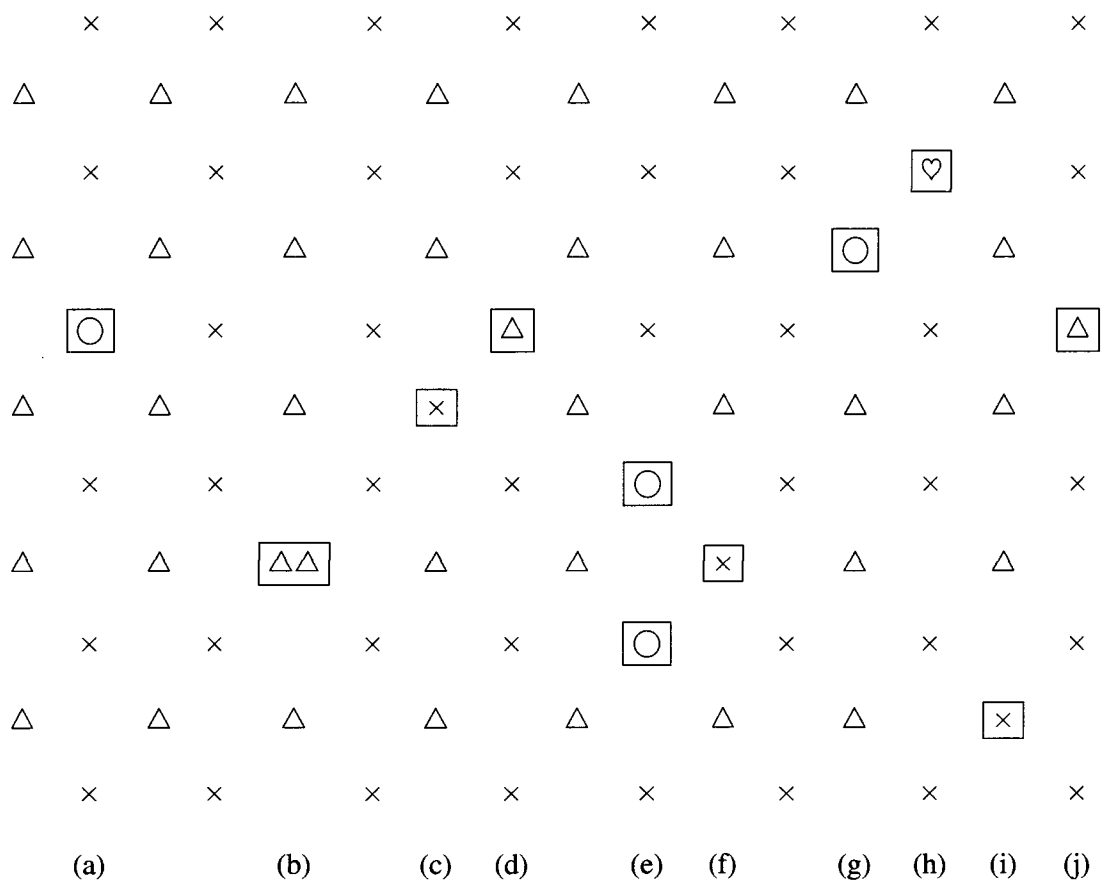

Figure 1.4: Typical point defects in a binary ordered intermetallic: (a) vacancy ($\bigcirc$); (b) split interstitial ($\triangle\triangle$); (c,d) bound pair of antisite defects ($\times\triangle$); (e,f) bound triple defect consisting of two vacancies and one antisite atom ($\bigcirc\bigcirc\times$); (g,h) vacancy-impurity ($\bigcirc\heartsuit$); (i,j) unbound pair of antisite defects ($\times\triangle$). Many other types of defects are possible (de Novion 1994).

review of the long-range ordering and disordering of solid solutions under irradiation is available elsewhere (Schulson 1979, Howe 1994). A functional relationship between the degree of long-range order S and the irradiation time t, using probabilistic arguments might be written as (Aronin 1953):

$$S = S_0 \exp(-\varepsilon K t) \tag{1.12}$$

where S_0 is the initial degree of long-range order and ε is a parameter which is a measure of the effectiveness with which the incident particle disorders the target material.

The mechanisms through which irradiation-induced ordering, disordering, and amorphization take place can be described as follows (Schulson 1979, Howe 1994, Motta 1997):

- Ordering corresponds to an increase in the probability that an atom A occupies an α lattice position and an atom B a β site. This change in atomic sitting involves the thermally-activated migration of irradiation-induced vacancies and therefore the phenomenon might be suppressed if the temperature of irradiation is sufficiently low and accelerated if the temperature is raised above ambient. It also occurs under irradiation conditions where isolated Frenkel defect pairs are generated (electron irradiation) as well as when there are displacement cascades (heavy-ion and neutron irradiation);

- Disordering is the rearrangement of atoms of one type into the sublattice of the other. Five possible mechanisms have been proposed to account for this phenomenon: thermal spikes, replacement collisions, plastic spikes, collapse of cascades to vacancy loops, and a random vacancy/interstitial (V/I) recombination. The predominant mechanism is dependent upon the nature of the irradiation. Presumably, the thermal spike, the replacement collisions, and the random recombination are the main mechanisms;

- Amorphization corresponds to the complete rearrangement of atoms into a structure having no long-range periodicity. It is yet not well understood how such a structure may form and why is it stable during irradiation at low temperature. The density of irradiation-induced defects within the damaged region is an important parameter. Two mechanisms have been proposed: direct crystalline-to-amorphous ($C \xrightarrow{a} A$) transformation, and overlap of displacement cascades. The former is characterized by discrete amorphous regions which are produced directly within certain collision cascades by the rapid cooling from the very high spike temperatures at which localized melting occurs. The latter is characterized by exceeding a critical defect density.

1.5 The nickel-aluminium system

The nickel-aluminium system has a phase diagram with extensive regions of homogeneity and contains five intermetallic compounds and two fcc solid solutions under thermodynamic equilibrium (Predel 1991, Ehrhart 1991, Mankins & Lamb 1992). It is also reported, in addition, the existence of two non-equilibrium compounds (Delavignette et al. 1972, Reynaud 1976, Lequeux 1979, Ellner et al. 1989) and a martensite (Ball 1967, Rosen & Goebel 1968, Smialek & Hehemann 1973, Robertson & Wayman 1984, Hangen et al. 1996, Wolff & Sauthoff 1996). The first is obtained by precipitation of substitutional nickel atoms in compounds above 54 at.% Ni. The second is obtained in aluminium rich compounds due to the ordering of vacancies in a triangular arrangement in the (111) nickel planes. The last one is found in 63 at.% Ni samples in the as-quenched condition and in greater quantity after aging. This martensitic phase has received a considerable interest due to its ordered CuAu I structure (Rosen & Goebel 1968, Enami & Nenno 1971) and also for the observation of shape memory effect (Enami & Nenno 1971, Chakravorty & Wayman 1976a, Chakravorty & Wayman 1976b). The stability, geometry, prototype, and lattice parameters of these phases are summarized in Table 1.1.

Table 1.1: Crystal geometry and lattice parameters of intermediate phases.

Phase	Stability	Geometry	Prototype	a [nm]	b [nm]	c [nm]
η	metastable	orth		0.640	0.756	0.956
$NiAl_3$	equilibrium	orth	$NiAl_3$	0.6612	0.7367	0.4812
Ni_2Al_3	equilibrium	rhomb	Ni_2Al_3	0.4363		0.4812
Ni_3Al_4	non-equilibrium	cub	Ni_3Ga_4	1.1408		
$NiAl$	equilibrium	cub	$CsCl$	0.2887		
Ni_3Al_2	metastable	bct		0.2668		0.3244
63 at.% Ni	martensite	fct	CuAu I	0.3788		3.209
Ni_5Al_3	equilibrium	orth	Pt_5Ga_3			
Ni_2Al	non-equilibrium	hex				
Ni_3Al	equilibrium	cub	Cu_3Au	0.357		

Of special interest are the equilibrium phases NiAl and Ni_3Al, with melting temperatures of 1911 and 1668 K, respectively. The former compound is said to have a B2 superlattice (Figure 1.1(a)) which can be seen as the combination of two interpenetrating simple cubic sublattices. NiAl is an ordered intermetallic stable within a large range of chemical composition, 42.0–53.4 at.% Al. Its long-range order is preserved within the range of existence of this phase and is found to be virtually complete up to 1273 K (Hughes et al. 1971, Visnov et al. 1980). The latter is a phase in the region 23–27 at.% Al and is said to have a superlattice structure of type $L1_2$ (Figure 1.1(b)) which can be understood by the interpenetration of four simple cubic sublattices; three of which are occupied by Ni atoms and one by Al atoms. Complete

long-range order is present up to 1603 K (Stoeckinger & Neumann 1970). It is reported the existence an allotropic phase of this compound which has a stable tetragonal unit cell of type DO_{22} in the temperature range of 973 K to 1373 K (Ramesh 1992).

1.6 Irradiation experiments

Irradiation of ordered intermetallics may induce a new crystalline structure, disorder, and amorphization depending on the projectile characteristics, irradiation conditions, and the chemical and physical properties of the target. This microstructural evolution might result from a variety of effects including the addition of a new atomic species into the target (implantation), the displacement of atoms from their original sites in collision cascades (mixing), the increase in thermal diffusion coefficient (radiation-enhanced diffusion), and the flowing of defects to sinks (radiation-induced segregation).

The concepts of implantation and mixing have a common ground (Matteson & Nicolet 1983). As processes, they differ mostly in emphasis. In implantation, the interest is focused on modifying the target by addition of the impinging species whereas in mixing, the chemical properties of the impinging species are not essential for the process but might be important as an implanted impurity. The fact that a primary particle has been introduced into the target is incidental. To underline the distinction between implantation and mixing, the experimental procedure of exposing a target to a beam of energetic particles is classified as an *implantation* when the addition of the specific chemical species of the beam is the primary aim, and as an *irradiation* when it is the mixing process that is primarily sought.

In order to understand the formation of irradiation-induced phases and to establish functional relationships between the irradiation parameters and the amount of defects and disorder created, various of the nickel-aluminium intermetallic compounds have been extensively studied (Nelson et al. 1972, Liu & Mitchell 1983, Potter 1983, Matteson & Nicolet 1983, Liu et al. 1983, Brimhall et al. 1983, Nastasi et al. 1983, Hung et al. 1983, Liu 1985, Jaouen et al. 1985, Brimhall & Simonen 1986, Thomé et al. 1987, Nastasi et al. 1987, Liu 1987, Liu et al. 1987, Was & Eridon 1987, Rivière et al. 1987, Jaouen, Rivière & Delafond 1987, Jaouen, Ruault, Bernas, Rivière & Delafond 1987, Nastasi & Mayer 1991, Alexander et al. 1991, Dimitrov et al. 1992a, Dimitrov et al. 1992b, Nastasi & Mayer 1994, Bui et al. 1995, Abromeit et al. 1995, Schäublin & Gotthardt 1996, Müller et al. 1997, Motta 1997, Ewert et al. 1998, Hessler 1999).

The seminal works of Liu et al. (1983), Liu (1985), Liu (1987), and Liu et al. (1987) evidenced a structural difference rule according to which an amorphous binary alloy is formed under mixing when the two constituent elements have a different structure, and is on the basis of a more sophisticated phenomeno-

logical model to predict the possibility of glass formation which is based on the characteristic parameters of maximum possible amorphization range, closely related to the solid solubilities, and the heat of formation of the system. The amorphization mechanism stems from the frustration of the competition between two different structures towards crystallization.

The works of Liu & Mitchell (1983), Brimhall et al. (1983), Jaouen et al. (1985), Brimhall & Simonen (1986), Nastasi et al. (1987), Thomé et al. (1987), Jaouen, Rivière & Delafond (1987), Jaouen, Ruault, Bernas, Rivière & Delafond (1987), Was & Eridon (1987), and Nastasi & Mayer (1991) introduced the concept of a critical defect density after which the structure transforms into the amorphous state. The premise is that if the total free energy of the defect crystalline state becomes higher than that of the amorphous state, a spontaneous transformation should occur. The stability of crystalline and amorphous phases during irradiation of intermetallic systems may be understood as a competitive process between free energy changes, point defect mobility, strain accumulation via antisite defects, and chemical disorder.

The studies of Jenkins et al. (1976), Jenkins & English (1982), and English & Jenkins (1987), have been of fundamental importance in order to characterize displacement cascade damage in ordered alloys using transmission electron microscopy. This series of investigations established the mechanism of cascade collapse into dislocation loops. Identification of disordered regions and quantification of long-range order has been done using the F-contrast method (Section 1.3). The distinction between structure factor contrast and strain field contrast allowed the identification of both disordered regions and dislocation loops. A disordered region might have (or not) an associated dislocation loop, whereas a dislocation loop has always a disordered region associated with it. Kimoto & Saito (1994) have recently reported quantitative examination of radiation-induced disordering and Bui et al. (1995) confirmed the cascade collapse mechanism into a vacancy loop. It has also been found that the probability of forming a dislocation loop from a displacement cascade increases as the size of the disordered region increases.

Kinetic models of irradiation-induced ordering and disordering in intermetallics (Liu & Mitchell 1983, Potter 1983) have been applied to the study of phase stability under irradiation (Abromeit et al. 1995), and to the reordering of disordered compounds to understand the role of point defect mobility in the microstructure evolution (Abromeit & Naundorf 1996). Further refinements have been introduced as a correction due to the surface influence on the production and development of displacement cascades (Müller et al. 1997).

Irradiation-induced reactions (formation of a new crystalline phase, order-disorder, and amorphization) may be generally (or partially) formulated as:

$$C \overset{n}{\rightarrow} C' \overset{d}{\rightarrow} D \overset{a}{\rightarrow} A \tag{1.13}$$

where C is the ordered crystalline phase, C' the new ordered crystalline phase, D the disordered phase, and A the amorphous phase.

It is clear that the stages of formation of a new crystalline phase and amorphization might not occur. Furthermore, amorphization might occur directly in a reaction of type $C \overset{a}{\rightarrow} A$. The amorphization reaction is triggered only under a narrow window of irradiation conditions and not for all of the nickel-aluminium intermetallics. A thermodynamical and kinetical treatment has been reviewed by Nastasi & Mayer (1991).

Due to their importance as second phase in superalloys (structural materials) and as model compounds for fundamental studies in radiation damage, the two intermediate phases NiAl and Ni_3Al will be referred. The former transforms via a $C \overset{d}{\rightarrow} D$ reaction under non-cascade production and, accordingly to Spaczér (1995), through a $C \overset{a}{\rightarrow} A$ reaction at temperatures below 100 K under cascade damage. The latter may only transform via a $C \overset{d}{\rightarrow} D$ reaction, even at temperatures as low as 80 K under cascade producing damage.

1.7 Computer simulations

The use of digital computers to simulate the behavior of assemblies of atoms under energetic particle irradiation has been greatly boosted by the many new research results obtained on the effects of neutron irradiation on the properties of matter, by the needs of nuclear fission power technology, or by the more speculative ones of fusion power development. A chronological review is found elsewhere (Robinson 1994).

Different approaches have been adopted to simulate radiation effects in solids. The binary collision approximation (BCA) has its roots in analytical theories of the stopping power of energetic particles in matter. Two classes of BCA computer models must be distinguished. In one of these, typified by MARLOWE (Robinson & Torrens 1974), the locations of potential target atoms are determined by a well-defined crystal structure. Stochastic methods play at most an auxiliary role in this code, supplying the initial particle positions or directions, and local disorder. Because of the regular structure, there are several important types of correlations among collisions in these models, of which channeling and linear

collision sequences are the best well known. Targets in the other class of BCA models are structureless. In these Monte Carlo (MC) codes, stochastic methods are used to locate potential target atoms or to determine impact parameters, flight distances, and scattering angles. There are no correlations between target sites, except those imposed by the material density. In MC codes, the number of atoms is not usually conserved, since there are no definite sites to identify the origins of atoms. The best known MC models are the family of TRIM codes (Biersack & Haggmark 1980). These models are, however, limited to the description of the collisional phase of the cascade process, which lasts for about 0.1 ps. Moreover, the lack of a many-body potential function excludes the simulation of the thermal spike and the cascade quenching, the processes immediately following the collisional phase.

In the molecular dynamics (MD) method the equations of motion of crystallites of a few hundred atoms are integrated until an initial perturbation is dissipated. The MD method was seriously constrained by computer limitations to the simulation of small numbers of individual events at low kinetic energies. Hardware developments have relaxed such limitations: MD codes can now follow collision cascades involving a million atoms for simulated times of hundreds of picoseconds.

In the MD method, a trajectory (configurations as a function of time) of the molecular system is generated by simultaneous integration of Newton's equations of motion for the N atoms in the system:

$$\frac{d^2 \vec{r}_i(t)}{dt^2} = m_i^{-1} \vec{F}_i \tag{1.14}$$

$$\vec{F}_i = -\frac{\partial V(\vec{r}_i, \ldots, \vec{r}_N)}{\partial \vec{r}_i} \tag{1.15}$$

where $\vec{F}_i$ is the force on the ith atom, m_i its mass, $\vec{r}_i$ its position, t is the time, and $V(\vec{r})$ is the potential.

This type of simulation requires the evaluation of the gradient of the potential energy $V(\vec{r})$, which therefore must be a differentiable function of the atomic coordinates $\vec{r}_i$. The integration of equation 1.14 is performed in small time steps Δt, typically of a few femtoseconds. Static equilibrium quantities can be obtained by averaging over the trajectory, which must be of sufficient length to form a representative ensemble of the state of the system. Another asset of MD simulation is that non-equilibrium properties can be studied by keeping the system in a steady non-equilibrium state. A more general form of equation 1.14 might be written through the addition of two terms:

$$\frac{d^2\vec{r}_i(t)}{dt^2} = m_i^{-1}\vec{F}_i + m_i^{-1}\vec{R}_i - \gamma_i\frac{d\vec{r}_i(t)}{dt} \tag{1.16}$$

where $\vec{R}_i$ is a stochastic force and γ_i is a friction coefficient.

The stochastic term introduces energy into the system, whereas the friction coefficient will induce a viscous force and therefore will remove energy from it. The condition for zero loss energy is written as follows (van Gunsteren & Berendsen 1990):

$$\langle \vec{R}_i^2 \rangle = 6m_i\gamma_i k_B T_r \tag{1.17}$$

where $\langle \vec{R}_i^2 \rangle$ is the mean-square value of the stochastic force, k_B the Boltzmann constant, and T_r the reference temperature of the system. This formulation can be applied to establish a coupling of the individual atomic motion to a heat bath.

The molecular dynamics program MOLDY6 has been developed for simulating crystals with large numbers of atoms, in particular for studying collision cascades in order to understand the evolution of the radiation damage produced by fast neutrons (Finnis 1988). Particular features of the program include flexible periodic boundary conditions, possibility to use embedded atom type potentials (Daw et al. 1993), 4-value Gear predictor-corrector algorithm, vectorized link-cell method of neighbor counting, and automatic updating of the size of the time step.

This program has been modified by de la Rubia & Guinan (1990) to include a fully vectorized algorithm to calculate the forces between atoms and named MOLDY-CASK. In addition, the program also implements several types of isotropic many-body interatomic potentials as well as three-body potentials for semiconductors. Another aspect of interest in the new version of the program is the introduction of the model of electronic losses and electron heat transport in cascades of Caro & Victoria (1989).

Molecular dynamics computer simulations have been very successful in providing a clear representation of the different stages occurring in a cascade: the collisional phase, the thermal spike, the quenching and the collapse. These results have shown the liquid-like structure of the cascade during the thermal spike, the quenching into disordered zones and defect clusters (de la Rubia 1989), and the loss of about 80% of the defects created in the collisional phase (Komarov 1992, Spaczér et al. 1994a). However, computational constraints impose severe limitations in the number of atoms that can be followed, and

therefore precludes the simulation of high-energy cascades (Caro et al. 1990, Alurralde et al. 1991, Alurralde et al. 1993).

To circumvent this limitation, and based on the profile of the energy deposited obtained using the BCA model, the diffusion of energy is followed by solving a simplified version of the heat transfer equation for a liquid-like material implemented in a code named THESPIK (Alurralde et al. 1991, Alurralde et al. 1993) as follows:

$$\frac{\partial Q}{\partial t} = \vec{\nabla} \cdot \frac{\xi}{\rho} \vec{\nabla} Q \tag{1.18}$$

where Q is the heat, t is the time, ξ is the thermal conductivity, and ρ is the density. The discretization of equation 1.18 in a cubic lattice of constant a might be written as:

$$\begin{aligned}
Q(x,y,z,t+\Delta t) = {} & \frac{\xi \Delta t}{\rho a^2} \{ Q(x-a,y,z,t) + Q(x+a,y,z,t) + \\
& Q(x,y-a,z,t) + Q(x,y+a,z,t) + \\
& Q(x,y,z-a,t) + Q(x,y,z+a,t) + \\
& (\frac{\rho a^2}{\xi \Delta t} - 6) Q(x,y,z,t) \}
\end{aligned} \tag{1.19}$$

where x, y, and z are the space coordinates, Δt is the time step, and a is the discretization parameter. The quantities ξ and ρ are functions of Q, and therefore of the spatial coordinates and time. Averaging these quantities over the nearest neighbor cells, and selecting an appropriate time step, equation 1.19 may be rewritten in a more simple form (Caro et al. 1990):

$$\Delta t = \langle \frac{\rho a^2}{7\xi} \rangle \tag{1.20}$$

$$Q(x,y,z,t+\Delta t) \quad = \quad \frac{1}{7}\{Q(x-a,y,z,t) + Q(x+a,y,z,t) + \qquad\qquad (1.21)$$

$$Q(x,y-a,z,t) + Q(x,y+a,z,t) +$$

$$Q(x,y,z-a,t) + Q(x,y,z+a,t) +$$

$$Q(x,y,z,t)\}$$

This approximation is valid provided the variation of the heat dependent parameters in equation 1.20 is small enough in order to justify the average.

An estimation of the molten volume from cascade damage using this approach compares very well with the MD prediction for the same event (Caro et al. 1990). Furthermore, the liquid droplet model (LDM) allows a thermodynamic description of the cascade and therefore permits the evaluation of the cascade geometry on parameters like ion-mixing, life time and volume of the melt. This is done in an energy range which is not covered by MD simulations, representing then a useful technique to qualitatively study the effects of radiation damage in solids.

The majority of MD results available on the nickel-aluminium intermetallic system are described in the works of Caro & Victoria (1990), de la Rubia, Caro & Spaczér (1993), de la Rubia, Caro, Spaczér, Janaway & Guinan (1993), de la Rubia et al. (1994), Spaczér et al. (1994b), Spaczér et al. (1994a), Spaczér, Caro, Victoria & de la Rubia (1995), Spaczér, Caro & Victoria (1995), Gao & Bacon (1995a), Gao & Bacon (1995b), Zhu et al. (1995), Spaczér (1995), and Spaczér et al. (1997).

Spaczér (1995) has studied in details the disordering and amorphization mechanisms of nickel-aluminium compounds using MD simulations under a variety of irradiation conditions. Of remarkable interest is the role of the electron-phonon coupling (Caro & Victoria 1989) on the disordering kinetics and amorphous transformation of these intermetallics. It has been found that in NiAl, a 15 keV PKA cascade induces no amorphization for a strong coupling, while a weak coupling led to it (Spaczér, Caro & Victoria 1995, Spaczér, Caro, Victoria & de la Rubia 1995). It has been concluded from MD simulations of 5 keV cascades in Ni$_3$Al that the bulk of the disordered region corresponds to a scaled fraction of the molten volume (de la Rubia, Caro & Spaczér 1993). In the same manner it has been shown from cascade simulation with PKA energies up to 5 keV in Ni$_3$Al that the regions containing 90% of the final anti-site defects have approximately the same size as the molten regions at the beginning of the heat spike (Gao & Bacon 1995a, Gao & Bacon 1995b). It was demonstrated in NiAl that the core of the cascade has high chemical disorder and does not relax back to the original structure after melting (Zhu et al. 1995).

Molecular dynamics methods, although numerically powerful, are not easily compared to experimental observations. Several attempts have been made in order to link molecular dynamics cascade damage results to transmission electron microscopy (TEM) observations with relative success (Kapinos & Bacon 1995, Almazouzi et al. 1998).

1.8 Motivation

In the nickel-aluminium system, research is motivated by an increasing industrial interest to develop special intermetallics for advanced engineering applications, including low density wear-resistant materials, high temperature structural materials, low-expansion alloys, soft magnetic alloys, shape memory alloys (Mankins & Lamb 1992, Miracle 1993, Ng et al. 1998) and state-of-the-art microelectronics, where interconnects and transition-metal aluminides on compound semiconductors are of paramount importance (Ishida et al. 1992, Harper & Rodbell 1997).

From a fundamental point of view these intermetallics constitute interesting systems for the study of irradiation-induced phase transformations (order → disorder, amorphization) and production of defects (Jenkins et al. 1976, Jenkins & English 1982, English & Jenkins 1987, Eridon & Was 1988, Larsen et al. 1992, Spaczér, Caro, Victoria & de la Rubia 1995, Spaczér, Caro & Victoria 1995, Abromeit et al. 1995, Spaczér et al. 1997, Müller et al. 1997, Ewert et al. 1998, Müller et al. 1999).

The results which have been reported so far can be divided into two groups, namely, the microstructural evolution under cascade producing irradiation in bulk intermetallics, and the irradiation-induced phase transformation in intermetallic thin films. These results have been analyzed in order to assess the disordering process (disordered zone and defect cluster morphology, defect yield, sink strength estimation, long-range order estimation, cascade collapse mechanisms, surface effects), and the defect accumulation and phase transformation phenomena (implantation, ion-mixing, stable and metastable compound formation, amorphization).

Irradiation of ordered intermetallics may induce disorder or amorphization depending on the projectile characteristics, irradiation conditions and chemical and physical properties of the target. The behavior of the various intermetallic compounds of the nickel-aluminium system with respect to electron and ion irradiation has been extensively studied in the recent past. Experiments have shown the partial disordering of NiAl and the complete disordering of Ni_3Al by electron irradiation at low temperature (Liu & Mitchell 1983). In the case of the NiAl compound, irradiation with light-ions has produced partial disorder (Rivière et al. 1987), whereas the use of heavy-ions has induced amorphization at low temperatures

(Jaouen et al. 1985, Thomé et al. 1987), which appears to be in agreement with molecular dynamics simulations. However, at the same temperature, heavy-ion irradiations of Ni_3Al layered samples have induced no amorphization (Brimhall et al. 1983, Hung et al. 1983). The majority of the mentioned experiments refers to multilayered samples. These samples are not very adequate to study the amount of ion-mixing, defect production and phase transformation with fluence (or dose) and energy density deposition, in a convenient way. For this reason, a bilayer structure would permit an in-depth study of these phenomena.

In more recent years, however, significant interest has driven the motivation for modelling these processes using molecular dynamics computer simulations (Caro & Victoria 1990, de la Rubia, Caro & Spaczér 1993, de la Rubia, Caro, Spaczér, Janaway & Guinan 1993, de la Rubia et al. 1994, Spaczér et al. 1994b, Spaczér et al. 1994a, Spaczér, Caro, Victoria & de la Rubia 1995, Spaczér, Caro & Victoria 1995, Spaczér 1995, Gao & Bacon 1995a, Gao & Bacon 1995b, Zhu et al. 1995, Spaczér et al. 1997, Almazouzi et al. 1998, Almazouzi et al. 1999).

These results have demonstrated the feasibility of simulating cascade damage in pure metals and intermetallics and led to the partial corroboration of phenomenological data which has been compiled from a set of experiments. Furthermore, it has been shown that in ordered NiAl a 15 keV-Ni recoil primary knock-on atom induces amorphization when a weak coupling between the electron and phonon systems is used, while in Ni_3Al the same conditions induces only local disordering (Spaczér, Caro & Victoria 1995, Spaczér, Caro, Victoria & de la Rubia 1995). Disordered and amorphized regions have been identified using molecular dynamics analysis tools.

Although numerically powerful, these methods of analysis are not easily compared to experimental observations. Therefore, an attempt must be made here to apply transmission electron microscopy techniques such as high resolution and conventional microscopy to investigate the above mentioned molecular dynamics samples by using a novel approach based on the multislice technique that allows to simulate transmission electron micrographs.

In this context, and in spite of the numerous efforts previously done, little information has been collected in order to perform a comparative study on the behavior of NiAl and Ni_3Al under heavy-ion irradiation. In so being, three mandatory groups of problems arose and have been studied:

- How do we synthesize stoichiometric and ordered intermetallic thin films as proper irradiation media, being able to evaluate microstructural artifacts?

- How do we establish a numerical link between molecular dynamics computer simulations of cas-

cade damage and transmission electron microscopy imaging of defect clusters, disorder, and amorphization?

- What are the basic aspects and structural differences in nickel-aluminium intermetallics under heavy-ion irradiation and how do they behave regarding primary ion energy, fluence (or dose), disordering, and defect accumulation?

1.9 Organization

The dissertation has been divided so that questions are addressed and studied in a functional and self-contained structure as follows:

- Chapter 1 reviews all the general concepts from basic physics definitions (ordered intermetallics, radiation damage, the nickel-aluminium system) to advanced measurement techniques (detection of order, F-contrast method) and computer simulation results (molecular dynamics and image simulation of irradiation-induced damage);

- Chapter 2 describes bulk single-crystalline specimen preparation, intermetallic thin film synthesis by r.f.-magnetron sputtering, microstructure characterization using transmission electron microscopy, secondary ion mass spectrometry, scanning tunneling microscopy, and chemical analysis. Furthermore, irradiation-induced damage simulations are presented in order to derive general purpose irradiation parameters;

- Chapter 3 introduces the origin of image formation in transmission electron microscopy (diffraction and phase contrast modes), the physics and methodology behind image simulation of thick specimens, the definition of imaging modes in virtual transmission electron microscopy, and the high resolution and diffraction contrast image simulation studies conducted in damaged intermetallics and pure metals;

- Chapter 4 presents the irradiated microstructure of both layered (control group) and bulk nickel-aluminium intermetallics, disordered zone and defect cluster size distributions and densities, comparative structural studies, and a novel quantitative long-range order measurement technique in cross-sectional transmission electron microscopy;

- Chapter 5 sets the final conclusions on the assessment of the order-disorder transformation and microstructure evolution in nickel-aluminium intermetallics under heavy-ion irradiation.

A complementary document on the imaging of defects produced by radiation damage and on many-beam dynamical calculation of conventional transmission electron microscopy contrasts is available (Appendix A).

Chapter 2

Specimen preparation and characterization

2.1 Intermetallic single-crystals

A single-crystal is a phase in which a periodic arrangement of atoms is reproduced into one single grain, therefore, it has a simplified microstructure (Van Vlack 1989). Single-crystalline samples are concrete representations of the more abstract mathematical models which define their topological properties. Such a mathematical representation is shown for both NiAl and Ni_3Al in Figures 1.1(a) and 1.1(b).

Single-crystalline samples of NiAl (100) and Ni_3Al (110) of purity 99.999% have been manufactured by Material-Technologie & Kristalle GmbH in the form of rods 2.5 cm in length and 1.0 cm in diameter. They have been analyzed at the Swiss Federal Laboratories for Materials Testing and Research using both x-ray fluorescence (XRF) and inductively coupled plasma optical emission spectrometry (ICP-OES). It has been found that among nickel and aluminium also traces of silicon and titanium were present. Chemical analysis of both intermetallics is summarized in Table 2.1.

Table 2.1: Chemical composition of the as-received intermetallic single-crystals as per ICP-OES.

Material	Expected [wt%]	Expected [at.%]	Measured [wt%]	Equivalent [at.%]
NiAl	$Ni_{68.5}Al_{31.5}$	$Ni_{50.0}Al_{50.0}$	$Ni_{68.7}Al_{31.3}$	$Ni_{50.1}Al_{49.9}$
Ni_3Al	$Ni_{86.7}Al_{13.3}$	$Ni_{75.0}Al_{25.0}$	$Ni_{86.6}Al_{13.4}$	$Ni_{74.9}Al_{25.1}$

These intermetallic single-crystals have been cut by spark erosion into discs of 0.1 cm thickness and 1.0 cm in diameter and have been polished using a series of silicon-carbide abrasive papers. A mirror-like

polishing has been performed using a 0.05 μm non-crystallizing colloidal silica suspension on a lap cloth.

2.2   Intermetallic thin films

The growth of oriented crystals during condensation onto metallic substrates has been studied in the past decades for a great number of bilayer systems, in particular for pure metals onto metals (Smith 1995, Machlin 1995). Research work has been published on the nickel-aluminium thin film deposition onto cleaved rock-salt (Kizuka et al. 1994, Schryvers et al. 1998, Yandouzi et al. 1998), semiconductors (Ishida et al. 1992, Van Swygenhoven et al. 1994), and in a limited scope onto nickel (Ng et al. 1998) where the thin film microstructure is transformed in a post-deposition annealing process. Although studies of the deposition conditions and its influence on the thin film crystalline structure and chemical composition exist (Kizuka et al. 1994, Schryvers et al. 1998, Yandouzi et al. 1998, Ng et al. 1998), there is no systematic work relating these parameters to the thin film morphology, interface chemistry and epitaxial modes of growth.

Zone models (Thornton 1977, Thompson 1990), which are used to predict the thin film microstructure as a function of primary deposition parameters such as the substrate temperature and the inert gas pressure, are quite useful for sorting out experimental results and for establishing starting points for the relationships between the physical vapor deposition (PVD) process and the microstructure. This approach is applied here in conjunction with a condensation regime analysis (Matthews 1975a, Matthews 1975b), which considers the surface energy balance between the substrate, the interface (transition layer) and the forming layer.

The major difficulties associated with the sputter deposition of intermetallic thin films are the control of the stoichiometry (Bunshah 1994) and the growth of ordered individual grains in a stable superlattice microstructure (Kizuka et al. 1994). This chapter reports on the synthesis and microstructural properties of r.f.-magnetron sputtered NiAl and Ni$_3$Al thin films onto n-type silicon (100) and nickel (110) substrates. Furthermore, it presents a detailed description of general purpose irradiation parameters.

2.2.1   Deposition

The NiAl and Ni$_3$Al thin films have been deposited in a sputtering system with two planar, confocal magnetron sources (Wu 1996). The most important deposition parameters are the target composition, working pressure, r.f. power, target-substrate distance, and especially the substrate temperature, T_s. Two

sputtering targets allow to control the chemical composition through calibration of their deposition rates. The alloy targets are homogeneous mixtures (hot-pressed) of $Ni_{75\ at.\%}Al_{25\ at.\%}$ and of $Ni_{50\ at.\%}Al_{50\ at.\%}$, with a purity of 99.9%. A second target of nickel (purity 99.99%) is used to adjust the chemical composition of the deposited film. The targets are water cooled discs, 50 mm in diameter, and controlled independently, making an angle of 5° with respect to the substrate normal.

Intermetallics of both types have been deposited onto silicon (100) and nickel (110) substrates in similar working conditions. The substrate temperature can be controlled from room temperature (RT) to about 800 K, using for this purpose a radiant heater placed behind the holder. Prior to the deposition the chamber was evacuated to a residual pressure of about 10^{-6} Pa, and backed out for 6 hours at 453 K. The target-substrate distance was fixed at 85 mm according to previous tests (Wu 1996). The substrate holder was rotating at 10 rpm. For T_s higher than RT the substrates were pre-heated for about 2 hours.

The target power conditions during the deposition and the substrate temperatures are summarized in Table 2.2. The argon pressure during the deposition was 0.67 Pa. After five minutes pre-sputtering the deposition rate fluctuated by less than 5% indicating a steady-state of yield of the elemental constituents of the targets (Glocker & Shah 1995). A calibration is presented in Figure 2.1 for both materials.

The use of a secondary nickel target hinders the plasma in the deposition chamber, due to its magnetic properties (Window & Sharples 1985), and therefore reduces the total deposition rate by a factor of up to 20%. The main reason to co-sputter this element is to correct the thin film chemical composition at the stoichiometry within 1 to 2 at.%.

Table 2.2: Thin film deposition parameters.

Sample Id.	T_s [K]	Target No. 1	power [W]	Target No. 2	power [W]
NiAl/Si #1	673	$Ni_{50\ at.\%}Al_{50\ at.\%}$	80	Ni	15
Ni_3Al/Si #2	673	$Ni_{75\ at.\%}Al_{25\ at.\%}$	80	Ni	15
Ni_3Al/Si # 3	303	$Ni_{75\ at.\%}Al_{25\ at.\%}$	40	Ni	160
Ni_3Al/Si # 4	523	$Ni_{75\ at.\%}Al_{25\ at.\%}$	40	Ni	80
NiAl/Ni #H1	708	$Ni_{50\ at.\%}Al_{50\ at.\%}$	80	Ni	80
Ni_3Al/Ni #H2	675	$Ni_{75\ at.\%}Al_{25\ at.\%}$	80	Ni	80

2.2.2 Thickness measurements

Thickness measurements have been made in-situ using a Maxtek quartz crystal oscillator. The results were in good agreement with ex-situ measurements using an Alphastep stylus profiler. Test thicknesses between 200 nm and 1.5 μm were chosen for both NiAl and Ni_3Al as it is intended to irradiate the thin
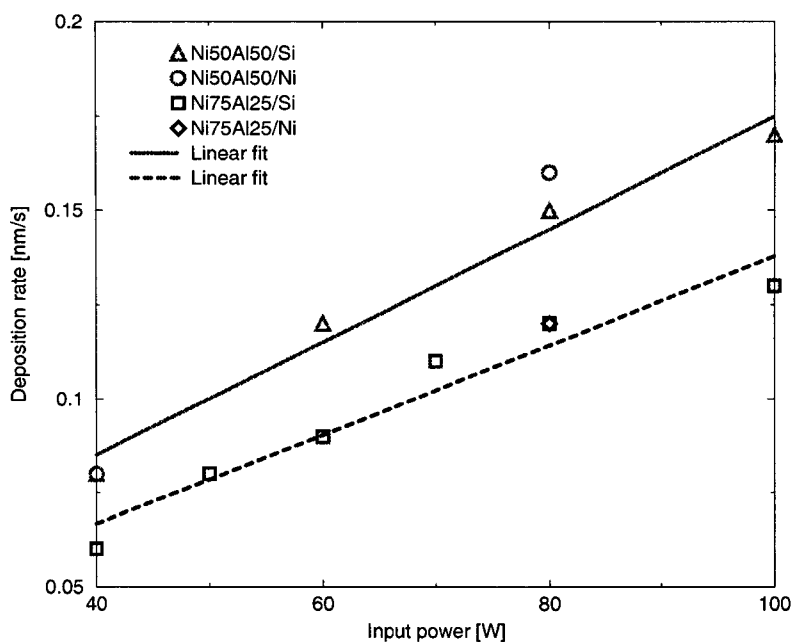
Figure 2.1: Dependency of deposition rate with target power for NiAl and Ni$_3$Al.

films with energetic ions and therefore their thicknesses should be in accordance with the projected range of the incoming ions.

2.2.3   Chemical analysis

Single-crystalline samples of both intermetallics have been analyzed with conventional wet chemical tests and further used as calibrated standards. This analysis confirms the stoichiometric ratio and high-purity (99.999%) of the samples and therefore these will be used for comparisons with the thin films measured by x-ray energy dispersive spectrometry (EDS).

Chemical analyses of the thin films and of the calibrated standards have been performed in a Philips XL30 FEG SEM using EDS. For the NiAl samples an acceleration voltage of 10 kV and a take-off angle of 35.8° have been used. For the Ni$_3$Al samples an acceleration voltage of 15 kV has been used with the same take-off angle.

A set of 3 different measurements per sample reproduced the same values within an experimental error of 0.5 at.%, indicating that the films are chemically homogeneous (Table 2.3). These results are in agreement with the ones obtained for the single-crystals and therefore the thin films are considered to have a stoichiometric chemical composition.

Table 2.3: Chemical composition of the as-sputtered samples and of the intermetallic standards.

Sample Id.	Chemical composition	Analysis method
NiAl/Si #1	$Ni_{50.59\ at.\%}Al_{49.41\ at.\%}$	EDS
Ni_3Al/Si #2	$Ni_{73.71\ at.\%}Al_{26.29\ at.\%}$	EDS
Ni_3Al/Si #3	$Ni_{74.88\ at.\%}Al_{25.12\ at.\%}$	EDS
Ni_3Al/Si #4	$Ni_{74.80\ at.\%}Al_{25.20\ at.\%}$	EDS
NiAl X'tal #5	$Ni_{50.22\ at.\%}Al_{49.78\ at.\%}$	Wet-chemical
NiAl X'tal #6	$Ni_{52.43\ at.\%}Al_{47.57\ at.\%}$	EDS
Ni_3Al X'tal #7	$Ni_{74.82\ at.\%}Al_{25.18\ at.\%}$	Wet-chemical
Ni_3Al X'tal #8	$Ni_{73.79\ at.\%}Al_{26.21\ at.\%}$	EDS

2.2.4 Microstructure of thin film on silicon

Transmission electron microscopy (TEM) using a Philips CM20 operating at 200 kV has been used to investigate the general microstructure, the crystalline structure, texture and the chemical order (presence of superlattice reflections) using selected area diffraction (SAD) and nano-diffraction (ND). Cross-sectional samples have been observed using a JEOL 2010 operated at 200 kV.

A 0.5 μm thick NiAl thin film deposited onto silicon at 673 K and observed in a planar-view geometry, where the incident electron beam is parallel to the film surface normal (Leifer 1997), is seen to crystallize in a structure with grains of 60 nm in diameter (Figures 2.2(a) and 2.2(b)). The presence of Moiré fringes from overlapping grains indicate that several grains superpose along the film thickness. The structure is compact (no visible cavities at the grain boundaries) with individual grains well delimited by high-angle grain boundaries. The preferential growth in the $\langle 110 \rangle$ direction is confirmed by SAD (Figure 2.2(c)).

When a planar-view specimen is tilted along a high angle (Figure 2.3(a)) a quasi-cross sectional projection is observed, showing a structure with non-equiaxed (elongated) grains oriented along a preferential crystallographic direction perpendicular to the film substrate. These grains are 150 nm long and show interference fringes at the border. The morphology difference between these two regions of the same sample (in Figures 2.2(a) and 2.3(a)) is due to nucleation and to the texturing effect, which develops a structure with small grains at the interface film/substrate and leads through coalescence to larger, elongated grains. In agreement with the extended zone model of Movchan-Demchishin, for a reduced temperature T_s/T_m of 0.35, a regime of high surface diffusion (called Z2) becomes significant and drives columns having tight grain boundaries (Smith 1995). The bright-field/dark-field pair micrographs (Figures 2.2(a) and 2.2(b)) confirm the typical grain size distribution, the Moiré interference fringes, and the well delimited grains with tight boundaries. The contrast distribution also indicates the texturing of the film (in the $\langle 110 \rangle$ direction). In SAD, spotty diffraction rings (Figure 2.2(c)) indicate that the thin film
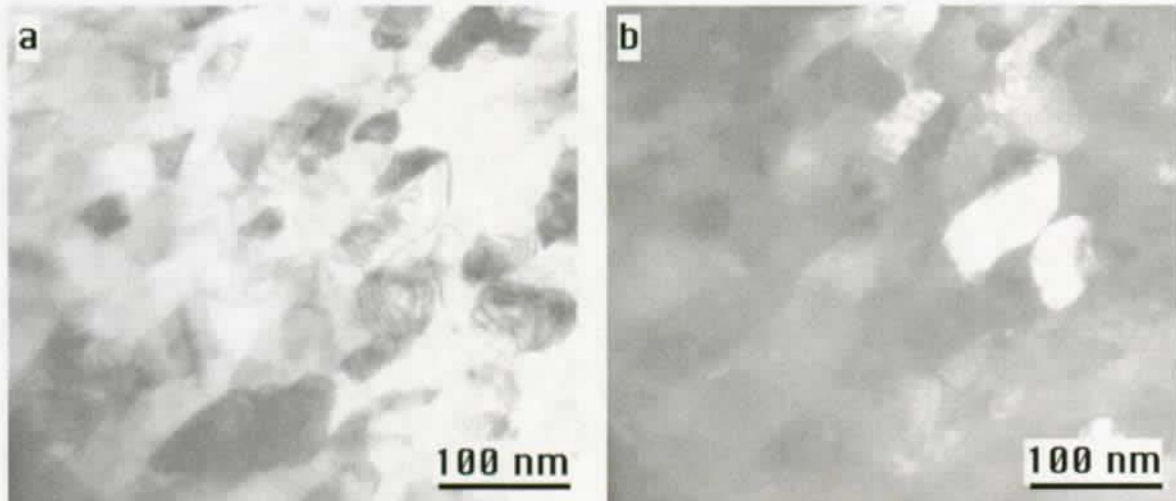
(a) BF

(b) DF (110)
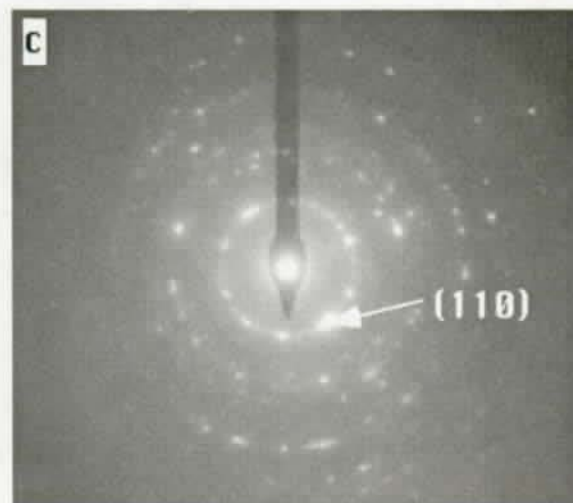
(c) SAD

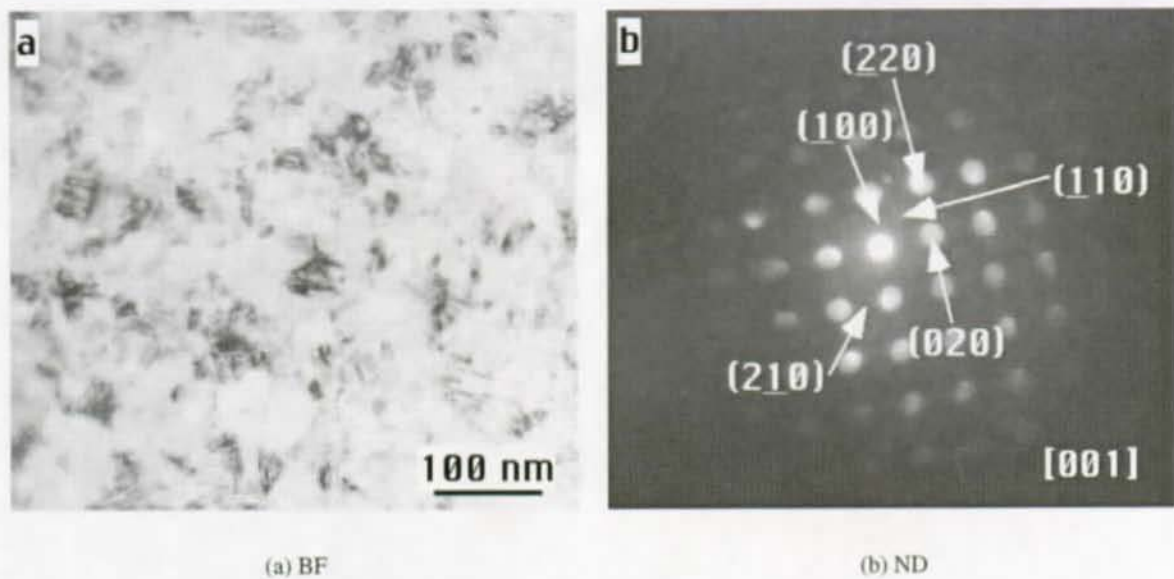Figure 2.2: Microstructure of a NiAl thin film deposited at 673 K imaged in (a) BF (b) DF (110) and (c) SAD modes.

has grown with a fraction of elongated crystallites about 3 times larger than the average grain size. The chemical order is identified from ND patterns. The (100) and (111) superlattice reflections are clearly visible in this [011] zone axis (ZA) ND (Figure 2.3(b)). These reflections are in agreement with those calculated for a NiAl crystal (Stadelmann 1987). The lattice parameter determined from the ND pattern using a (200) reflection spot, $a = 0.287$ nm, is in agreement with the bulk $a = 0.2887$ nm (Predel 1991).

(a) BF   (b) ND
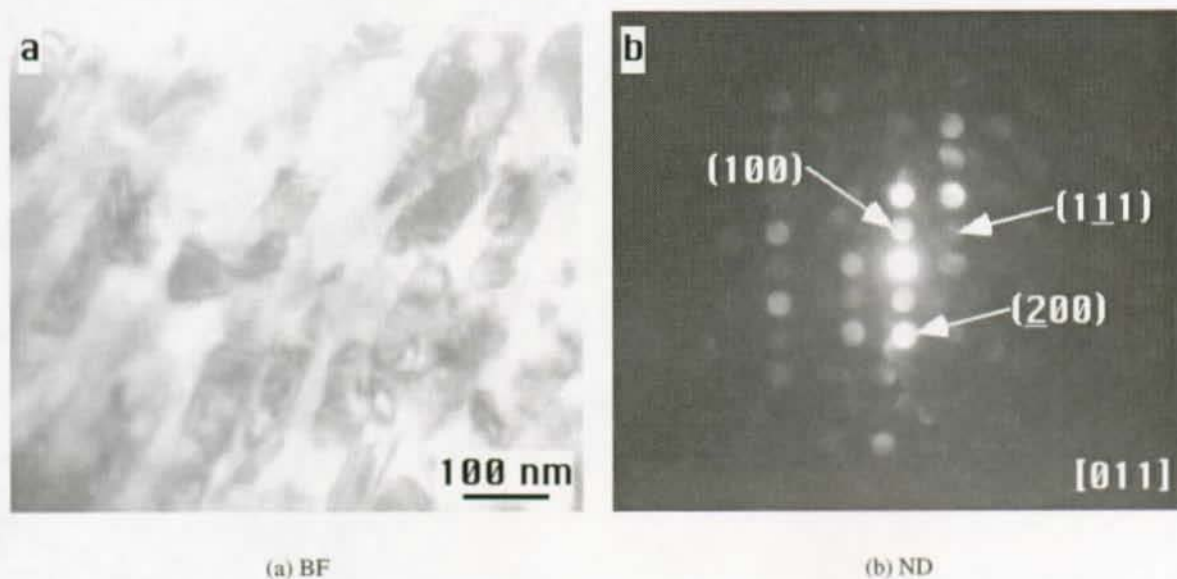
Figure 2.3: Microstructure of a NiAl thin film deposited onto silicon at 673 K tilted to a high angle showing (a) a non-equiaxed elongated grain structure and (b) ND pattern ([011] ZA).

For a 0.5 μm thick Ni$_3$Al thin film deposited onto silicon at 673 K, a bright-field/dark-field pair (Figures 2.4(a) and 2.4(b)) shows that the grain size is 45 nm in average (Figure 2.4(a)) with poorly delimited grain boundaries (Figure 2.4(b)). The contrast indicates the existence of a defect structure, possibly stacking-faults, inside the crystallites (Figure 2.5(a)), and planes of crystallographic discontinuity at the grain boundaries (Thornton 1977). The thin film is strongly textured in the $\langle 111 \rangle$ direction (Figure 2.4(c)). The spotty diffraction rings (Figure 2.4(c)) indicate large coalesced grains of about 100 nm. The reduced temperature (T_s/T_m) is in this case 0.4, and corresponds to a transition regime between ZT and Z2 (Smith 1995). In SAD patterns, (100) and (110) superlattice reflections are visible as the two diffraction rings close to the (111) ring (Figure 2.4(c)).

The (100), (110), and (210) superlattice reflections are visible in a ND micrograph with a [001] ZA (Figure 2.5(b)), in agreement with the simulated diffraction patterns. The existence of a (210) superlattice reflection identifies the crystal structure as being of type L1$_2$. The lattice parameter calculated from the (111) and (200) reflections, $a = 0.360$ nm, is in close to the bulk value $a = 0.357$ nm (Predel 1991).

A cross-sectional view, in which the electron beam is parallel to the interface (Leifer 1997), shows the
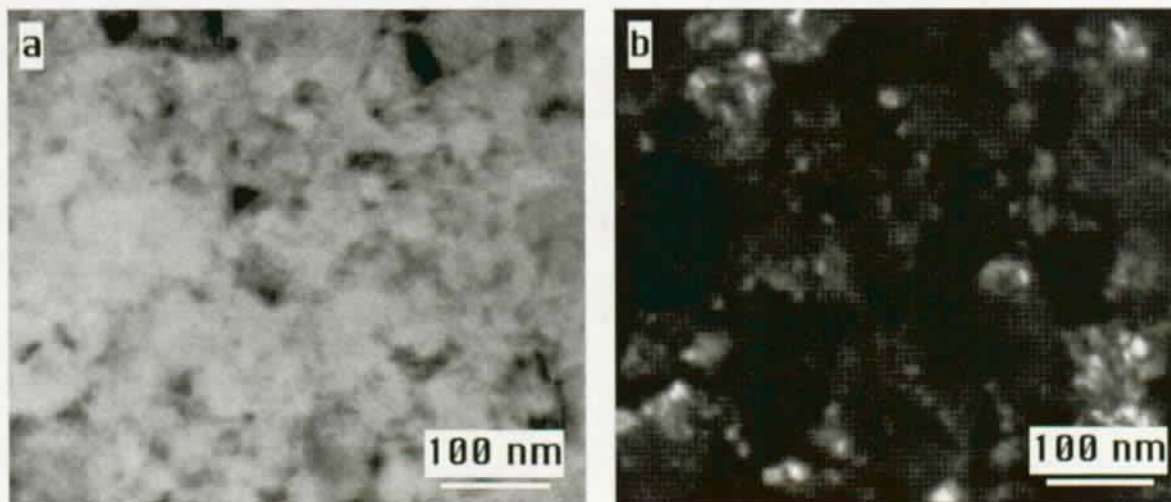
(a) BF

(b) DF (111)
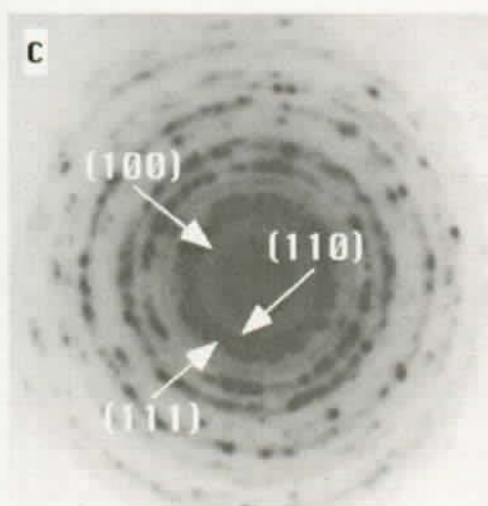
(c) SAD

Figure 2.4: Microstructure of a Ni$_3$Al thin film deposited at 673 K imaged in (a) BF (b) DF (111) and (c) SAD modes.

(a) BF   (b) ND

Figure 2.5: Microstructure of a Ni₃Al thin film deposited onto silicon at 673 K showing (a) a defect pattern inside the crystallites and (b) ND pattern ([001] ZA).

interface region between the silicon (100) substrate and the Ni₃Al thin film (Figure 2.6(a)) deposited with low growth rate at RT (in order to minimize the lattice mismatch strain (Smith 1995)). The reduced temperature is 0.16, corresponding to a growth zone of type Z1 where the low deposition rate favors the development of a fiber texture morphology. In the SAD pattern the presence of satellites on the (111) diffraction ring (Figure 2.6(b)) indicates that the film is textured in the ⟨111⟩ direction. A bright-field/dark-field pair (Figures 2.6(c) and 2.6(d)) evidences the structure of the thin film in cross-section with a sequence of stacking faults. The very fine interference Moiré fringes denote that the film is composed of several grains in thickness, possibly indicating micro twinning formation during deposition. A peak analysis from Figure 2.6(b) allows the detection of the (112) peak due to chemical order just before the (202) peak. The lattice parameter calculated from the (111) and the (112) diffraction rings, $a = 0.357$ nm, is in agreement with the bulk value.

2.2.5 Microstructure of thin film on nickel

Cross-sectional specimens of NiAl and Ni₃Al thin films deposited onto nickel have been prepared with focused ion beam (FIB) milling (Kuroda et al. 1998) due to the difficulties of mechanically polishing the metallic substrate down to a thickness of about 100 nm. The specimens are covered with a protective coating of gold and platinum to avoid sputtering of the intermetallic layer. They are cut and mounted onto copper rings and milled to the desired thickness using a gallium source operated at 30 kV. These samples have been observed using a JEOL 2010 transmission electron microscope (TEM) operated at

(a) X-TEM

(b) SAD

(c) BF
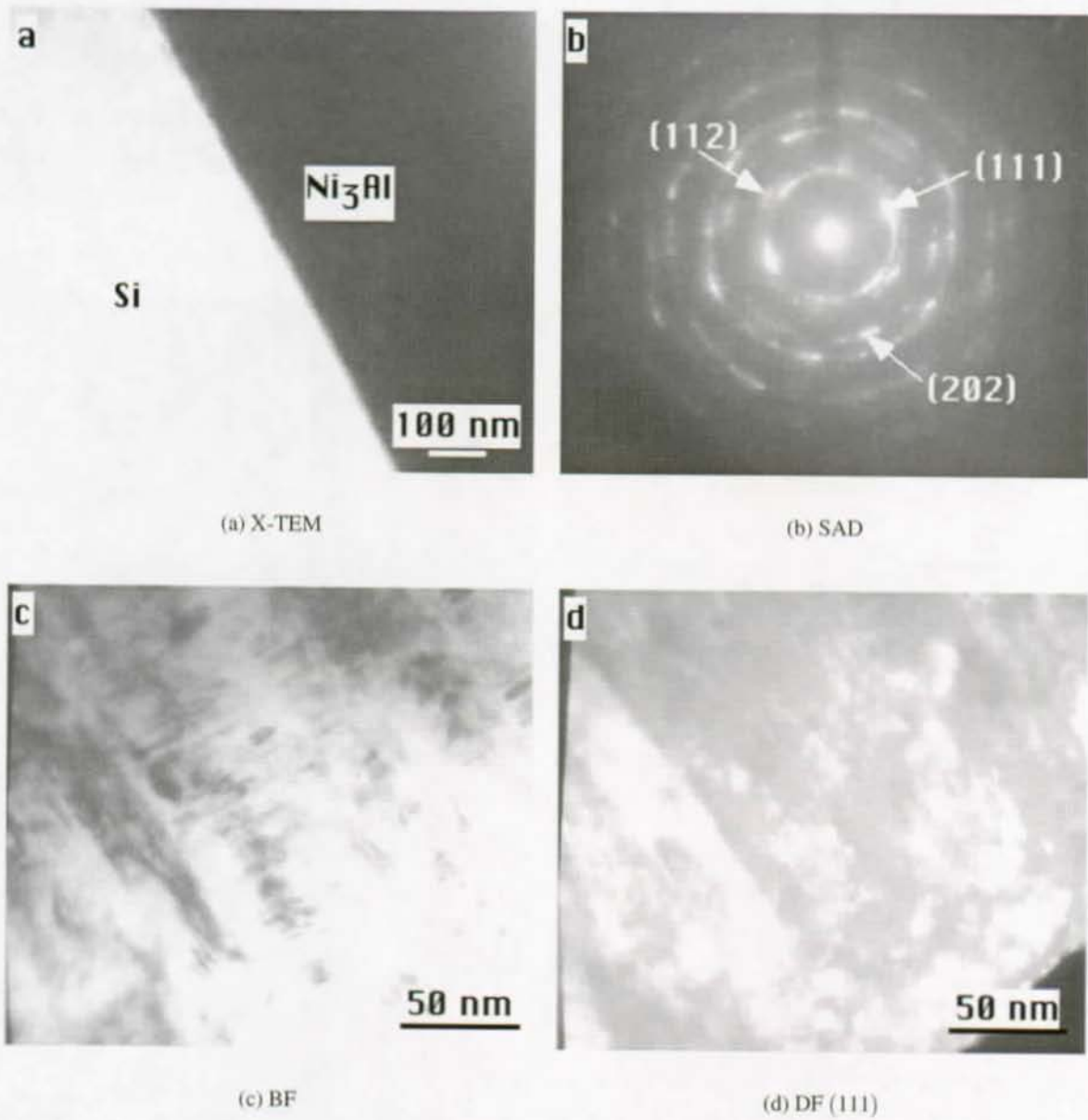
(d) DF (111)

Figure 2.6: Microstructure of a Ni₃Al thin film deposited at RT imaged in (a) X-TEM (b) SAD (c) BF and (d) DF (111) modes.

200 kV.

The microstructure of a 1.8 μm NiAl thin film deposited onto nickel (110) at high temperature is shown in cross-sectional view tilted to a [112] ZA (Figure 2.7(a)).

A subpopulation of the grains exhibit a granular-heteroepitaxial (Machlin 1995) inverse Nishiyama-Wassermann (NW) relationship $(\bar{2}11)[\bar{2}11]_{B2} \parallel (\bar{1}10)[\bar{1}10]_{fcc}$. This relation is established after analysis of the SAD pattern (Figure 2.7(b)) where the substrate diffraction vector $\vec{g}_1 = 1/2[\bar{2}20]_{fcc}$ in a [112] ZA is parallel to the thin film diffraction vector $\vec{g}_1 = [\bar{2}11]_{B2}$ in a [111] ZA, being both perpendicular to the interface. Tilting the sample to a [110] ZA confirms the chemically ordered structure of the intermetallic by the presence of the $\{100\}$, $\{111\}$ and $\{122\}$ planes ($h + k + l = $ odd).

(a) BF (b) SAD
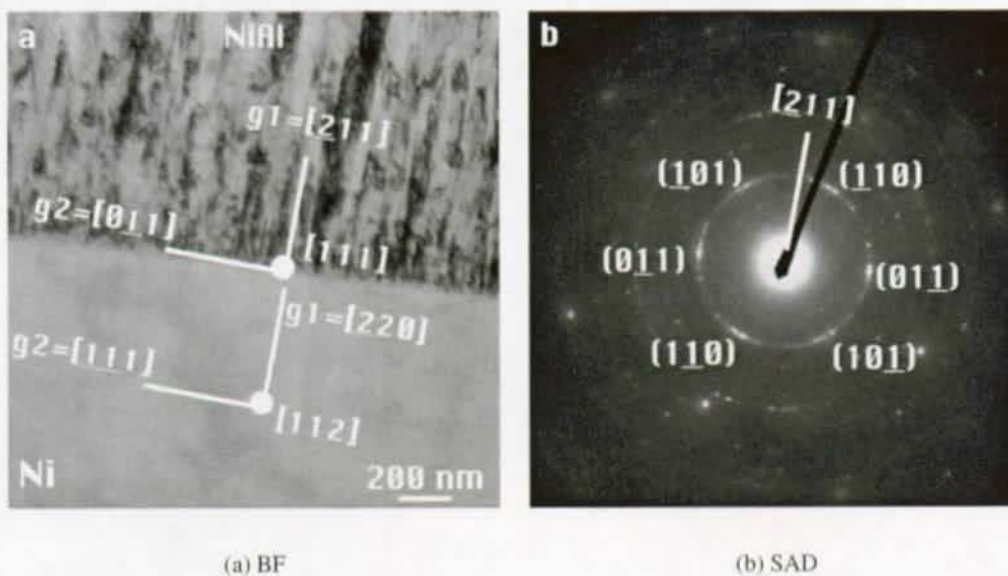
Figure 2.7: Microstructure of 1.8 μm NiAl/nickel (110) bilayer deposited at 675 K imaged in (a) BF and (b) SAD ([111] thin film ZA $\parallel$ [112] substrate ZA.)

The reduced temperature (T_s/T_m) is 0.37, corresponding to a regime of type Z2. The lattice mismatch is 5.3%, being the lattice parameter ratio thin film to substrate equal to 0.8202. These values are in agreement with the optimal ratio and misfit limit defined in the rigid lattice approximation (van der Merwe 1982, Hellwig et al. 1998) for the NW orientation relation. This type of regime results in the microstructure being dominated by heteroepitaxially aligned grains due to the interface energy minimization of in-plane grain rotations (Thompson 1990). The thin film is composed by grains exhibiting the inverse NW relationship and by polycrystalline grains of small size. As evaluated from the (110) reflections, the thin film lattice parameter, $a = 0.2886$ nm, is in agreement with the bulk value.

The general microstructure of a 1.8 μm Ni$_3$Al thin film deposited onto nickel (110) at high tempera-

ture is shown in cross-section (Figure 2.8(a)) tilted to a [112] ZA. A heteroepitaxial growth relation of $(\bar{1}10)[\bar{1}10]_{L1_2} \parallel (\bar{1}10)[\bar{1}10]_{fcc}$ is established after the analysis of the SAD pattern (Figure 2.8(b)) where the substrate diffraction vector $\vec{g}_1 = 1/2[\bar{2}20]_{fcc}$ is parallel to the single-crystalline thin film diffraction vector $\vec{g}_1 = [\bar{1}10]_{L1_2}$ in a [112] ZA, being both perpendicular to the interface. The {110} family of planes (hkl, mixed even and odd) confirms the chemically structured phase of the intermetallic.

(a) BF   (b) SAD
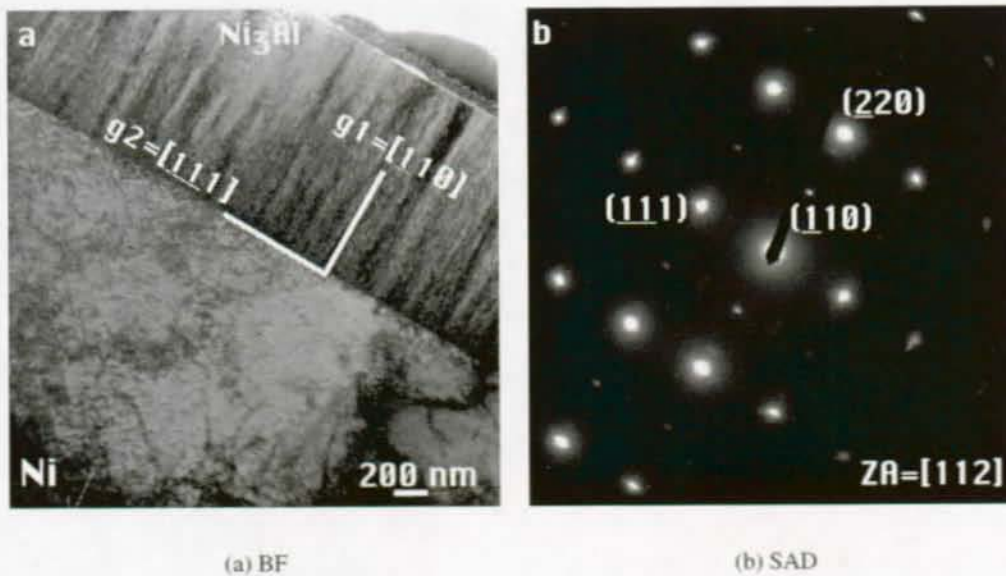
Figure 2.8: Microstructure of 1.8 μm Ni$_3$Al/nickel (110) bilayer deposited at 675 K imaged in (a) BF and (b) SAD ([112] thin film ZA $\parallel$ [112] substrate ZA.)

The reduced temperature (T_s/T_m) is 0.4, and corresponds to a growth zone between types ZT and Z2. However, the lattice mismatch is minimal (1.4%) under the above mentioned orientation relation and therefore prompts a coherent growth. As evaluated from the (110) and the (220) reflections, the thin film lattice parameter, $a = 0.356$ nm, is in agreement with the bulk value.

2.2.6 Interface characterization

Secondary ion mass spectroscopy (SIMS) measurements have been made with an Atomika 4000 apparatus, eroding an area of 100 μm $\times$ 100 μm by scanning an O_2^+ ion beam of 10 μm diameter at 10 keV.

The SIMS profile of a Ni$_{50.59 \text{ at.\%}}$Al$_{49.41 \text{ at.\%}}$ sample, 0.5 μm in thickness, deposited at 673 K on a silicon (100) substrate has been measured at an estimated average sputtering rate of 0.1 nm/s to a depth of about 0.8 μm (Figure 2.9). The ratio of the oxygen background signal to the intensities of the elemental constituents is of the order of 10^{-4}. There is no significant increase of the oxygen content at the interface region. The depth resolution, which includes both the surface roughness and the cascade mixing, is

estimated as 25 nm by fitting the trailing part of the intensity signal of nickel-58 to a Gaussian distribution function of standard deviation σ, and assuming that this statistical value is one-half of the depth resolution (Czanderna 1975, Liebl 1975, Hofmann 1992).

The SIMS profile of a $Ni_{74.80\ at.\%}Al_{25.20\ at.\%}$ sample, 0.5 μm in thickness, deposited at 523 K on a silicon (100) substrate corresponds to a depth of about 0.7 μm with an average sputtering rate of 0.08 nm/s (Figure 2.10). The relative intensity of the oxygen background to the elemental species of the thin layer is 1.40×10^{-4}. The depth resolution is estimated as 30 nm. The elemental signal intensity of both nickel and aluminium is constant throughout the deposited layer, thus indicating a homogeneous compound. The transition from a flat to a stiff slope in the elemental constituents intensities at the film interface indicates a non-diffused interface with an oxygen content almost as low as the sensitivity of the mass spectrometer.

2.2.7 Surface characterization

Scanning tunneling microscopy (STM) has been performed with an Omicron apparatus operating in constant current mode after cleaning the samples in HF.

For the as-sputtered $Ni_{50.59\ at.\%}Al_{49.41\ at.\%}$ deposited at 673 K, the lateral grain size is in average 23 nm, with values as large as 50 nm (Figure 2.11). The crystallites are formed by small sub-grains with sizes ranging from 5 to 10 nm showing cavities between their boundaries, which is typical of a bcc crystalline lattice (Wu 1996).

For the as-sputtered $Ni_{74.88\ at.\%}Al_{25.12\ at.\%}$ sample deposited at room temperature (RT), the lateral grain size is estimated as 36 nm (Figure 2.12). The grains are well formed polygons delimited by high-angle grain boundaries, showing no cavities. The average surface roughness is in both cases of about 1 nm (root mean square value).

2.3 Irradiation parameters

Intermetallic samples of both NiAl and Ni_3Al have been irradiated with nickel ions in a Tandem accelerator at the Swiss Federal Institute of Technology Zurich. In this facility, single charged positive nickel ions are produced at 700 keV and double charged positive nickel ions are produced at 6 MeV. For the range of ionic currents used in this work the displacement rate is estimated as 10^{-4} dpa/s. The samples were prepared following the procedures described in section 2.1, masked, and irradiated at liquid nitro-
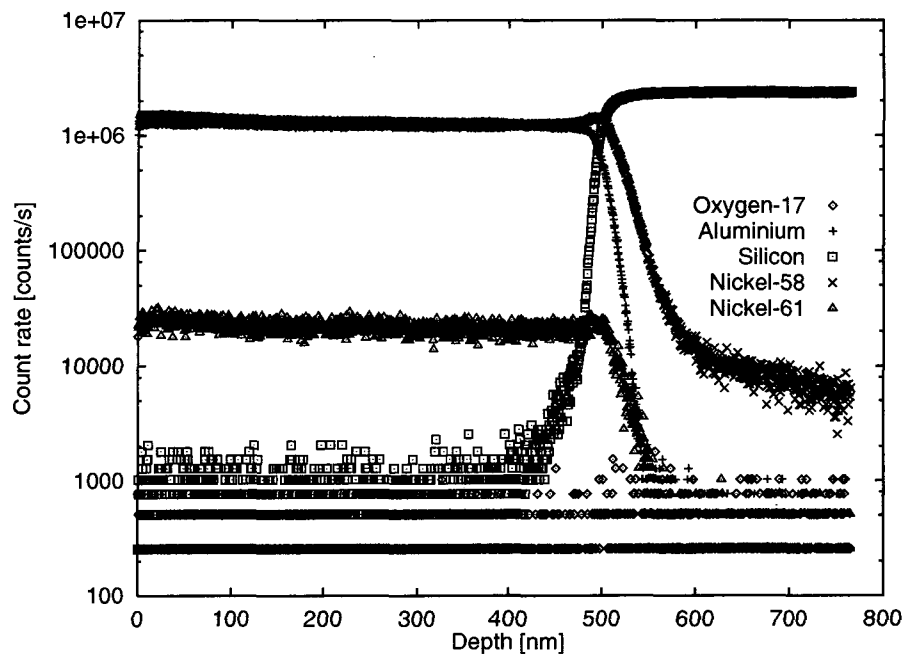
Figure 2.9: SIMS profile of a NiAl thin film deposited at 673 K.
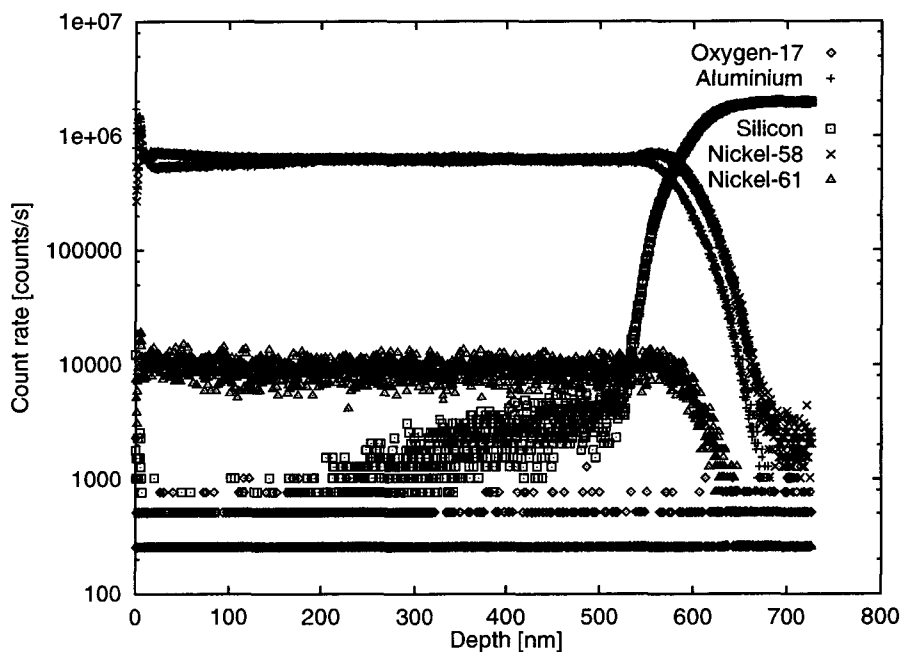
Figure 2.10: SIMS profile of a Ni_3Al thin film deposited at 523 K.
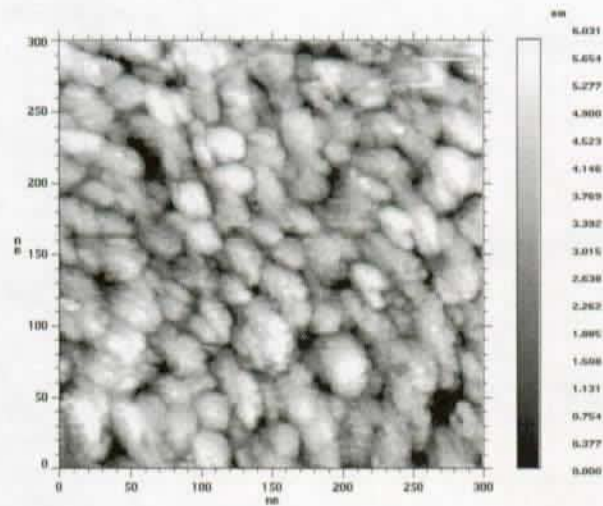
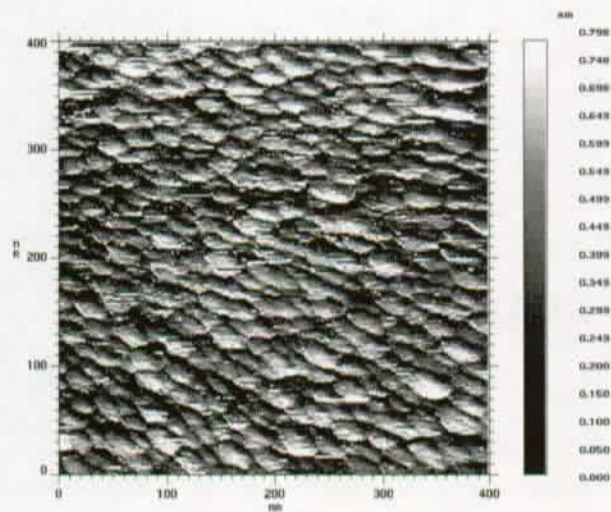Figure 2.11: STM analysis of the surface of a NiAl thin film deposited at 673 K.

Figure 2.12: STM analysis of the surface of a Ni_3Al thin film deposited at RT.

gen or room temperature (RT) either with 700 keV or 6 MeV primary energy ions and fluences up to 10^{15} cm^{-2}.

A set of Monte Carlo computer simulations has been performed with TRIM to obtain the damage distributions as functions of depth which are then used to calculate the displacement cross-sections and to estimate the equivalent doses in displacements per atom (dpa). The target properties are resumed in Table 2.4 and have been deployed as input parameters in these computer simulations. Displacement energies have been reported in the work of Zhu et al. (1995).

Table 2.4: Target properties for Monte Carlo simulation using TRIM.

Mater.	Density [g/cm^3]	At. density [m^{-3}]	Disp. energy [eV]	Structure
NiAl	5.9	8.3×10^{28}	37	Amorphous
Ni$_3$Al	7.5	8.8×10^{28}	40	Amorphous

The damage distributions corresponding to the number of displaced atoms versus depth in NiAl and Ni$_3$Al have been calculated for a total number of 5000 incoming ions in order to achieve statistical confidence.

At the low energy regime, primary energy ions of 700 keV induce a number of displacement events as shown for NiAl and Ni$_3$Al in Figures 2.13(a) and 2.14(a), respectively. At the high-energy regime, primary energy ions of 6 MeV create a number of displacements as shown for NiAl and Ni$_3$Al in Figures 2.15(a) and 2.16(a), respectively. The distributions include primary ion displacements, recoil displacements, and the total number of displacements. Recoil displacements represent almost the totality of the events.

Displacement cross-section distributions corresponding to the above mentioned cases can be evaluated from the displacement curves through the convolution with the specific atomic volume, $\Omega = a^3/\mathcal{N}$, where a is the lattice parameter of the intermetallic and $\mathcal{N}$ is the number of atoms in the cell. Specific atomic volumes for both intermetallics are shown in Table 2.5.

Table 2.5: Specific atomic volumes.

Mater.	a [nm]	$\mathcal{N}$ [at.]	Ω [nm^3]
NiAl	0.2887	2	0.01203
Ni$_3$Al	0.357	4	0.01137

The cross-section distributions for NiAl and Ni$_3$Al are shown in Figures 2.13(b) and 2.14(b) in the low primary ion energy regime (700 keV), and in Figures 2.15(b) and 2.16(b) in the high primary ion energy

regime (6 MeV). The maximum value of the displacement cross-section, σ_d, and the projected range, R_p, are reported in Table 2.6 and are used for ballistic information and fluence conversion in dpa.

Table 2.6: Maximum displacement cross-section and projected range.

Mater.	σ_d [m^2]		R_p [nm]	
	700 keV-nickel	6 MeV-nickel	700 keV-nickel	6 MeV-nickel
NiAl	1.48×10^{-19}	9.52×10^{-20}	250	1660
Ni$_3$Al	1.54×10^{-19}	1.03×10^{-19}	210	1440

Table 2.7 presents an irradiation matrix relating fluence, dose, and nickel ion concentration for both intermetallics under 700 keV or 6 MeV primary energy ions. These values are calculated for the maximum displacement cross-section. At the low primary ion energy regimes (Figures 2.13(b) and 2.14(b)) the displacement cross-section is almost constant within the projected range of the incoming ions whereas at the high primary ion energy regimes (Figures 2.15(b) and 2.16(b)), the displacement cross-section increases almost a decade.

Table 2.7: Irradiation matrix fluence × dose × nickel ion concentration.

Mater.	700 keV-nickel			6 MeV-nickel		
	Φ [cm^{-2}]	G [dpa]	C_i [appm]	Φ [cm^{-2}]	G [dpa]	C_i [appm]
NiAl	10^{15}	1.5	481	10^{15}	1.0	72.2
	10^{14}	0.15	48.1	10^{14}	0.10	7.22
	10^{13}	0.015	4.81	10^{13}	0.010	0.722
	10^{12}	0.0015	0.481	10^{12}	0.0010	0.0722
Ni$_3$Al	10^{15}	1.5	546	10^{15}	1.0	78.5
	10^{14}	0.15	54.6	10^{14}	0.10	7.85
	10^{13}	0.015	5.46	10^{13}	0.010	0.785
	10^{12}	0.0015	0.546	10^{12}	0.0010	0.0785

This phenomenon has its explanation in the different energy regimes and therefore in the different electronic and nuclear stopping behavior as shown for NiAl (Figure 2.17(a)) and Ni$_3$Al (Figure 2.17(b)). These curves might be interpreted as showing that below 700 keV primary energy nickel ions the electronic stopping is lower than the nuclear stopping prompting almost only elastic collisions. Above this threshold and mostly at the high-energy regime, this mechanism is reversed and the greatest amount of particle interactions is of inelastic nature.

2.4 Summary

Intermetallic sample preparation has been seen to be a subject of research in itself, the majority of the results having been published (de Almeida, Schäublin, Almazouzi, Victoria & Lévy 2000). The production of intermetallic thin films onto nickel (110) is a unique and elegant medium for the study of irradiation-induced phase transformations (order $\rightarrow$ disorder, amorphization) and defect production. Thin film deposition onto silicon (100) is meant as a calibration procedure due to the lack of similar ballistic and transport properties with regard to the intermetallic. Of main technological importance is the growth of these intermetallics onto silicon (100) as candidate interconnecting materials for the microelectronics industry.

Partially for the purpose of being candidate specimens for heavy-ion irradiation, intermetallic thin films of stoichiometric NiAl and Ni_3Al have been deposited onto nickel (110) single-crystalline substrates using r.f.-magnetron co-sputtering. The morphology and crystal structure of the thin films have been mostly studied by conventional transmission electron microscopy from planar-view and cross-sectional samples. Chemical order has been assessed using nano-diffraction techniques. The existence of superlattice reflections has confirmed a fully ordered structure in both intermetallics. Granular- and heteroepitaxial relations have been observed when sputtering onto nickel at high substrate temperature. A granular-heteroepitaxial mode of growth exhibiting the inverse Nishiyama-Wassermann relationship $(\bar{2}11)[\bar{2}11]_{B2} \parallel (\bar{1}10)[\bar{1}10]_{fcc}$ is observed in NiAl for the first time, whereas a single-crystalline heteroepitaxial growth relation of $(\bar{1}10)[\bar{1}10]_{L1_2} \parallel (\bar{1}10)[\bar{1}10]_{fcc}$ is achieved in Ni_3Al.
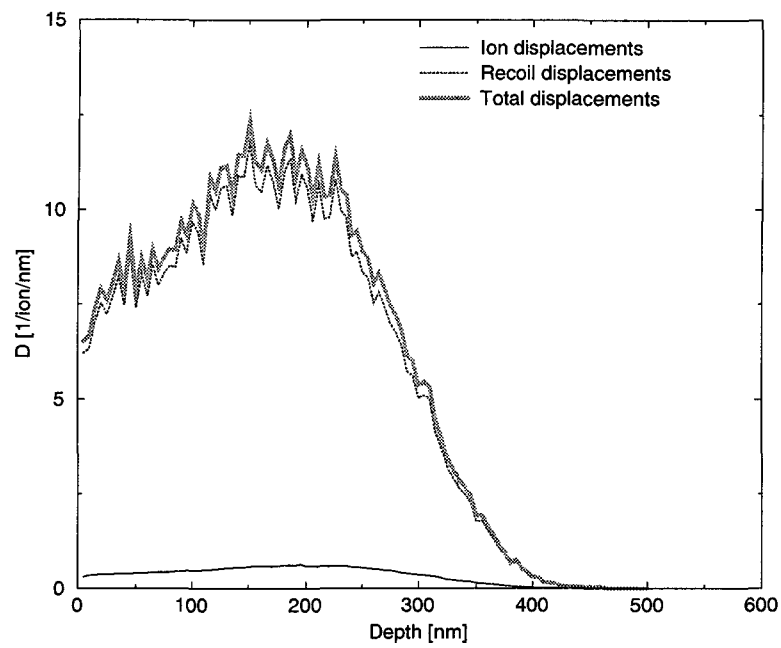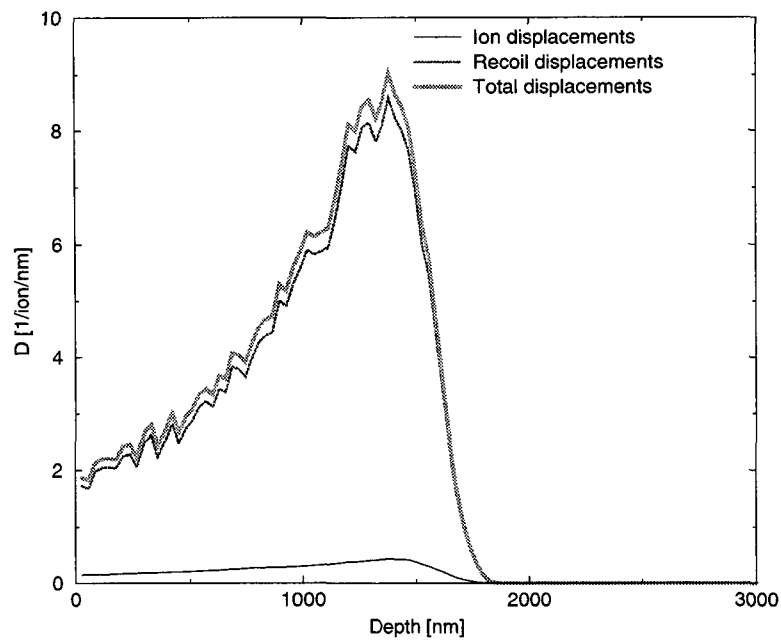
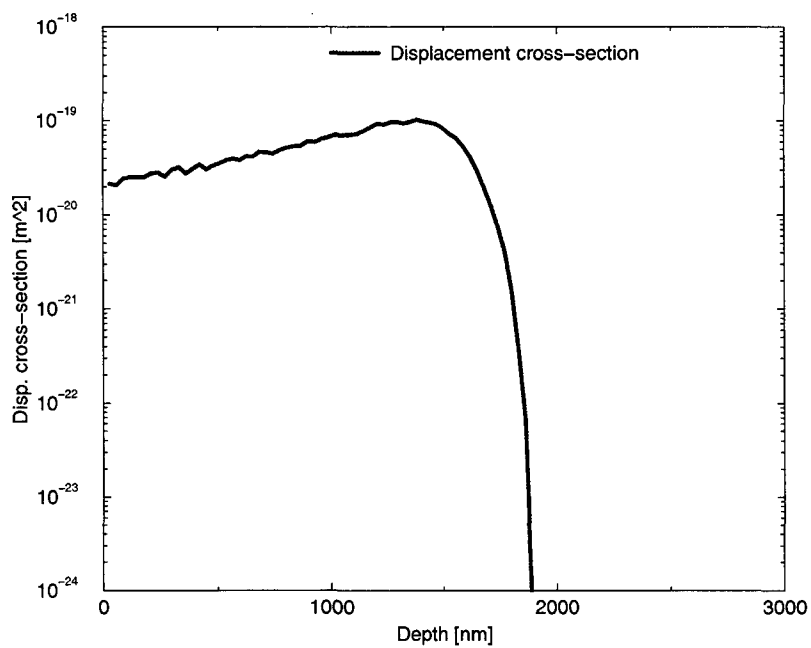(a) Displacement distributions
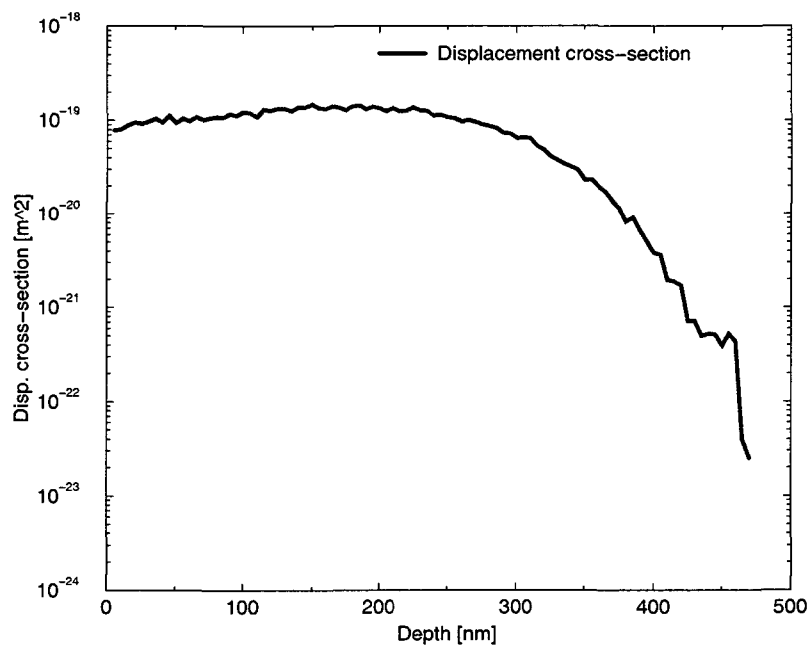
(b) Displacement cross-section

Figure 2.13: Monte Carlo computer simulations of the (a) displacement and (b) displacement cross-section distributions in NiAl for 700 keV-Ni primary ions.
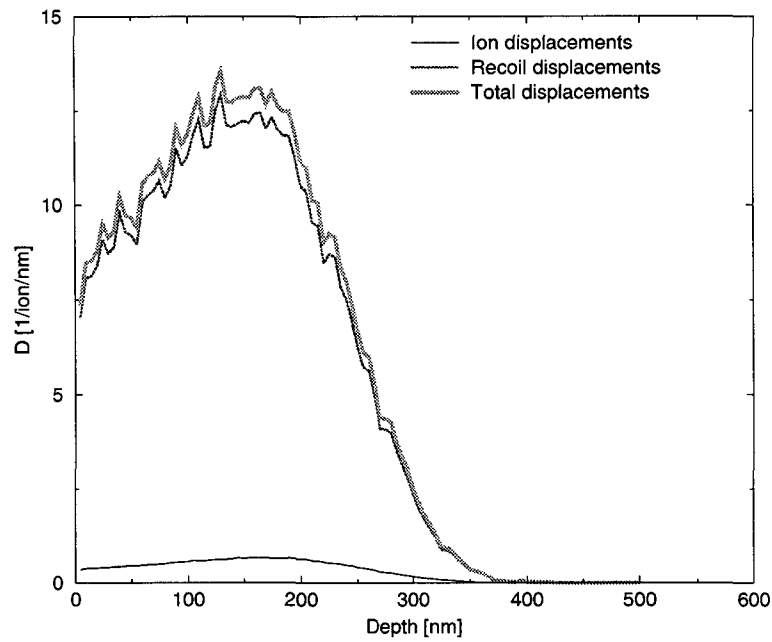
(a) Displacement distributions
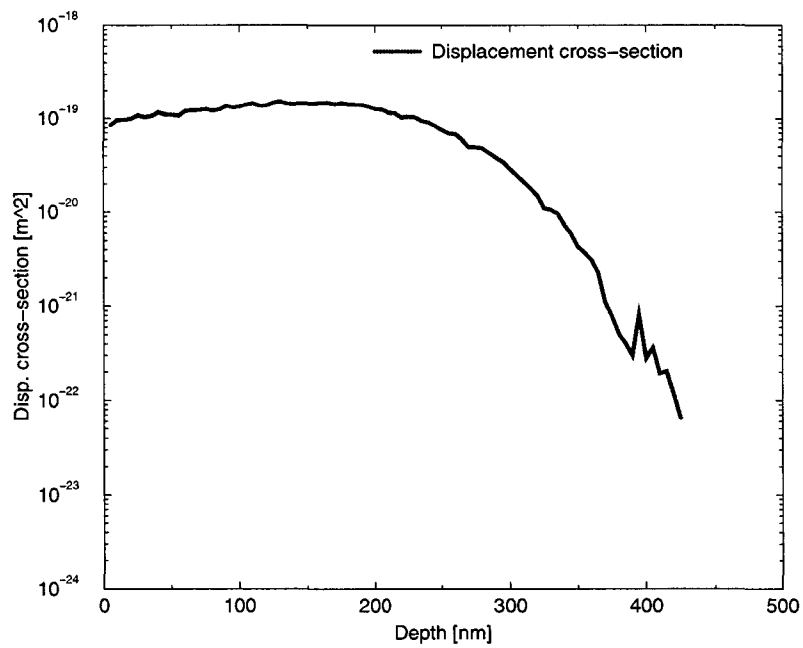
(b) Displacement cross-section

Figure 2.14: Monte Carlo computer simulations of the (a) displacement and (b) displacement cross-section distributions in Ni_3Al for 700 keV-Ni primary ions.
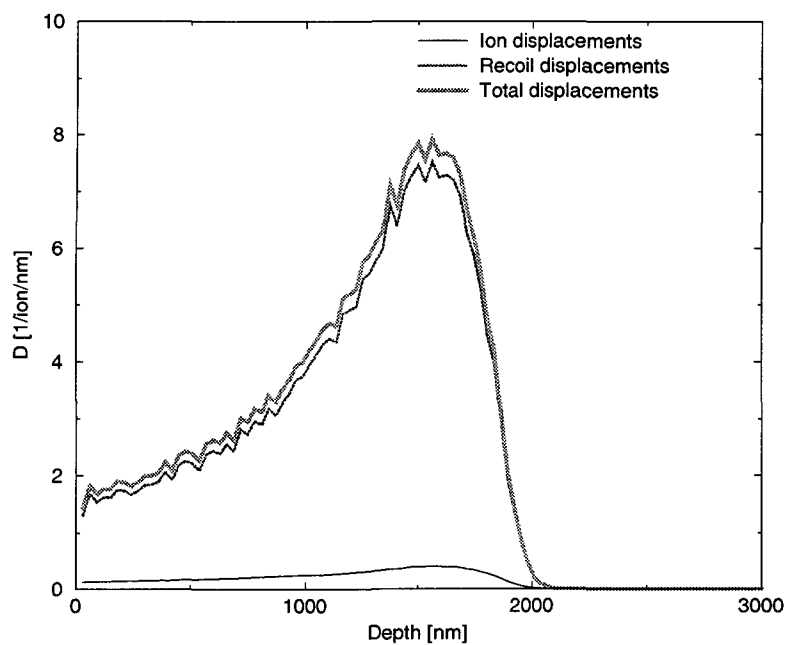
(a) Displacement distributions
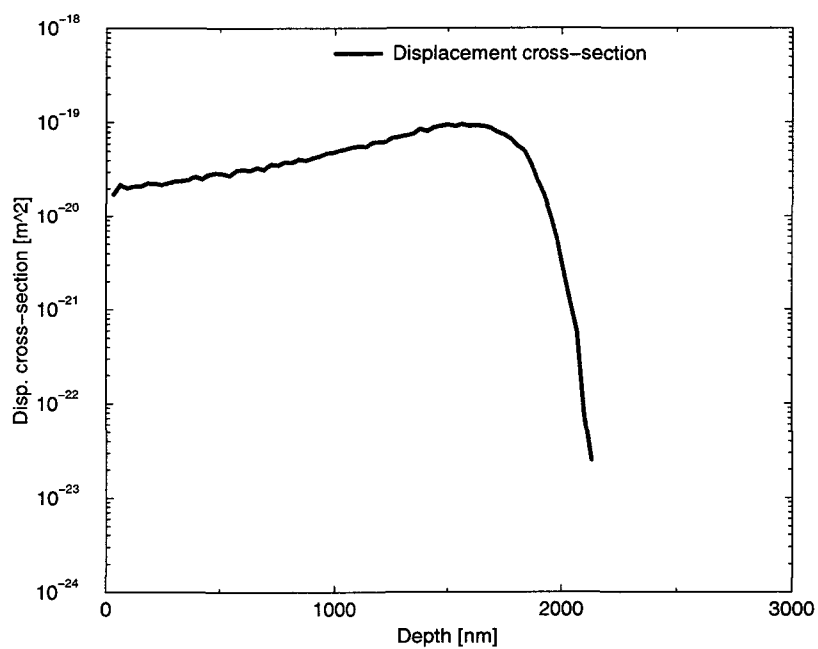
(b) Displacement cross-section

Figure 2.15: Monte Carlo computer simulations of the (a) displacement and (b) displacement cross-section distributions in NiAl for 6 MeV-Ni primary ions.

(a) Displacement distributions

(b) Displacement cross-section

Figure 2.16: Monte Carlo computer simulations of the (a) displacement and (b) displacement cross-section distributions in Ni_3Al for 6 MeV-Ni primary ions.
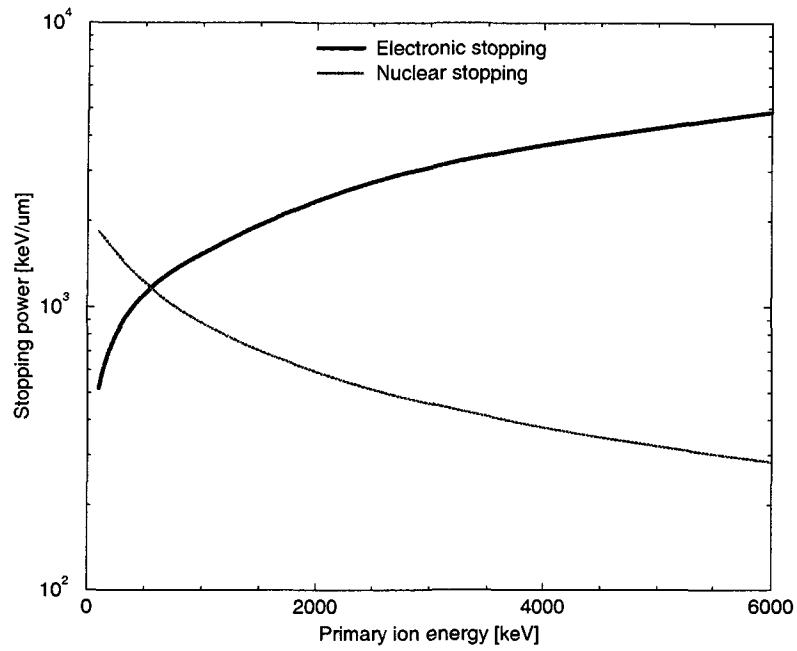
(a) Stopping power in NiAl
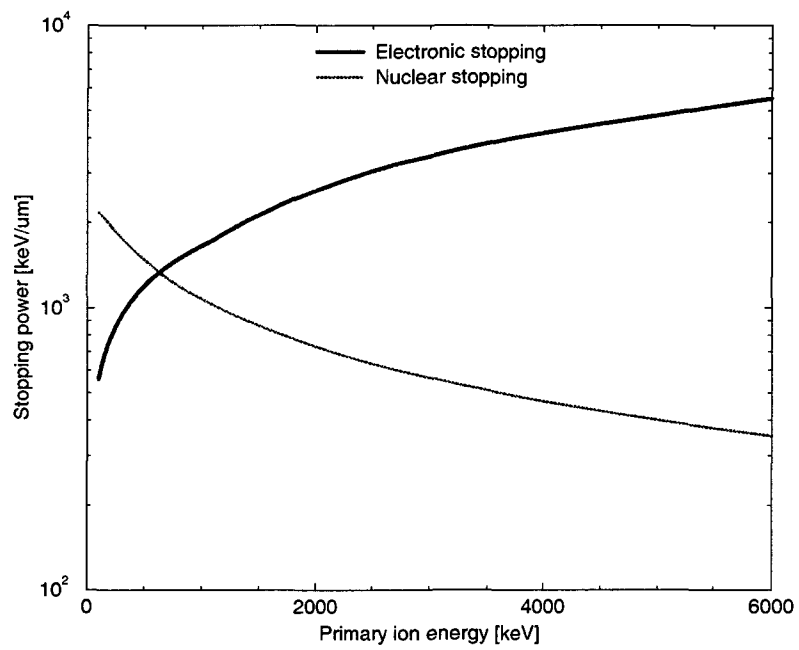
(b) Stopping power in Ni₃Al

Figure 2.17: Computer simulations of the electronic and nuclear stopping for (a) NiAl and (b) Ni₃Al.

Chapter 3

Transmission electron microscopy image simulation

Ars est celare artem.

3.1 The origin of image contrast

The microstructure of matter can only be studied through the interaction with particles, which carry information from the object to the observer. For this specific purpose, electrons are extremely useful since, as compared to other particles, they are easy to generate, to accelerate, to deflect, and to detect. Information from the bulk of the object is then obtainable by scattering with high-energy electrons (Hirsch et al. 1977), typically accelerated at 200 kV in modern microscopes (Van Dyck 1998).

There are two basic transmission electron microscopy (TEM) imaging modes in which information might be obtained during the scattering event. In high resolution TEM (HRTEM), phase contrast arises due to the interference of multiple electron waves which originate from the scattering of the incident electron beams by the sample. The differences in phase create either constructive or destructive interference and therefore constitutes a very fine mechanism to explore the atomic structure of thin samples. In phase contrast mode a number of selected beams are collected by the objective aperture after which they interfere to create a high resolution image of the lattice that can be modulated by the defocus. In conventional TEM (CTEM), Bragg diffraction is controlled by the crystalline structure and orientation of the sample. This type of imaging condition is used to create the so called conventional or diffraction contrast image by selecting a single transmitted or diffracted beam. This contrast is spatially restricted

47

Table 3.1: Steps in the simulation of TEM images of thick specimens using the multislice method.

Step 1 Divide the specimen into thin slices;

Step 2 Calculate the atomic projected potential $v_{zn}(x,y)$ for each slice;

Step 3 Calculate the transmission function $t_n(x,y) = \exp[i\sigma v_{zn}(x,y)]$ for each slice;

Step 4 Initialize the incident wave function $\psi_0(x,y) = 1$;

Step 5 Recursively transmit and propagate the wave function through each slice $\psi_{n+1}(x,y) = p_n(x,y,\Delta z) \otimes [t_n(x,y)\psi_n(x,y)]$ using fast Fourier transforms. Repeat until the wave function is all the way through the specimen;

Step 6 Fourier transform the wave function at the exit surface of the specimen $\Psi_n(k_x,k_y) = FT[\psi_n(x,y)]$;

Step 7 Multiply the transmitted wave function $\Psi_n(k_x,k_y)$ by the transfer function of the objective lens, $H_0(k)$ to get the image wave function in the back focal plane $\Psi_i(k_x,k_y) = H_0(k)\Psi_n(k_x,k_y)$;

Step 8 Inverse Fourier transform the image wave function $\psi_i(x,y) = FT^{-1}[\Psi_i(k_x,k_y)]$;

Step 9 Calculate the square modulus of the image wave function (in real space) to get the final image intensity $g(x,y) = |\psi_i(x,y)|^2 = |\psi_n(x,y) \otimes h_0(x,y)|^2$. ∎
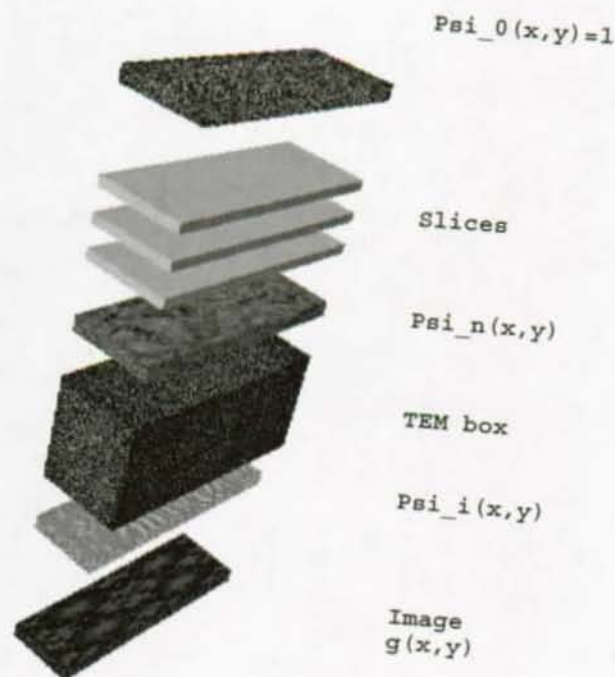
Figure 3.1: Conceptual representation of the multislice method.

due to scattering occurring only at Bragg angles.

3.2 Image simulation of thick specimens

Image simulation evaluates the electron micrograph from first principles. It starts from a basic quantum mechanical description of the interaction between the imaging electrons in the microscope and the atoms in the specimen. From this description the wave function of the imaging electrons might be calculated at any position in the microscope. If the optical parameters of the lenses in the microscope are known, then the two dimensional intensity distribution in the final electron micrograph might be calculated with high precision.

The multislice method was originally developed to simulate HRTEM images of perfect crystals (Cowley & Moodie 1957). The HRTEM and CTEM image simulation approaches used here are based on the multislice calculation and performed with the help of the EMS software (Stadelmann 1987). This technique allows to circumvent the deformable ion approximation (Hirsch et al. 1977) which was used with success in the case of well defined defects such as dislocations using the beam approach (Schäublin & Stadelmann 1993, Baluc & Schäublin 1996). In the case of unknown three dimensional defects, however, the deformable ion approximation may be invalidated because of both steep gradients in the surrounding strain field and changes in chemical composition and structure inside the defect relatively to the matrix. The difficulty of the multislice approach in simulating a CTEM image resides in the selection of the appropriate diffraction condition. The diffraction condition in CTEM, which is specified in a general way by the diffraction vector, the Laue circle center and the acceleration voltage, is selected by choosing the appropriate slicing direction. The slicing direction is chosen in order to excite the selected diffraction vector and to obtain slices that are periodic. Details on the method being available elsewhere (Kirkland 1998), only the basic elements are presented in Table 3.1 and Figure 3.1.

The specimen is to be divided into thin slices of equal thickness $\Delta z = z/n$, where z is the total thickness and n is the number of slices. The atomic projected potential $v_{zn}(x,y)$ for each slice is evaluated as follows:

$$v_{zn}(x,y) = V_s(x,y,n\Delta z)\Delta z \qquad (3.1)$$

where $V_s(x,y,n\Delta z)$ is the electrostatic potential for the nth slice. The specimen transmission function

$t_n(x,y)$ is defined as:

$$t_n(x,y) = \exp\left[\frac{i2\pi me\lambda}{h^2} V_{zn}(x,y)\right]$$
(3.2)

where m is the relativistic electron mass, e is the electron charge, λ is the electron wavelength, and h is the Planck constant. The wave function $\psi_0(x,y)$ for a plane wave traveling along the optic axis is written as:

$$\psi_0(x,y) = \exp\left(\frac{i2\pi z}{\lambda}\right)$$
(3.3)

where z is the propagation direction and λ is the electron wavelength. The propagation of the transmitted $\psi_{n+1}(x,y)$ wave function through the specimen is done by convoluting the propagation operator $p(x,y,\Delta z)$ with the transmitted wave function $t_n(x,y)\psi_n(x,y)$. The propagation operator is defined as follows:

$$p(x,y,\Delta z) = \frac{1}{i\lambda\Delta z}\exp\left[\frac{i\pi}{\lambda\Delta z}(x^2 + y^2)\right]$$
(3.4)

where x and y are the coordinates, λ is the electron wavelength, and Δz is the slice thickness. The exit wave function $\Psi_n(k_x, k_y)$ can be obtained by Fourier transforming the $\psi_n(x,y)$ function. The image wave function $\Psi_i(k_x, k_y)$ is obtained by multiplication of the objective lens transfer function $H_0(k)$ and $\Psi_n(k_x, k_y)$. The objective lens transfer function is defined as:

$$H_0(k) = \exp[i\chi(k)]A(k)$$
(3.5)

$$\chi(k) = \pi\lambda k^2[0.5C_s\lambda^2 k^2 - \Delta f]$$
(3.6)

$$A(k) = \begin{cases} 1 & ; \quad \lambda k = \alpha < \alpha_{max} \\ 0 & ; \quad \text{otherwise} \end{cases}$$
(3.7)

where $\chi(k)$ is the aberration function, $A(k)$ is the aperture function, k is the spatial frequency, λ is the

electron wavelength, C_s is the coefficient of the spherical aberration, Δf is the defocus, and α is the semi-angle at the objective lens. The image wave function in the real space can be calculated by inverse Fourier transforming $\Psi_i(k_x, k_y)$. The final image intensity distribution $g(x,y)$ is then equal to $|\psi_i(x,y)|^2$.

3.3 Virtual specimens and imaging modes

A virtual specimen is a mathematical representation of a crystalline structure. This representation mimics a small size crystal to be studied under the virtual microscope and includes the atomic positions of all chemical species. This structure must have a three dimensional periodic boundary.

The simplest procedure to build such a structure is to generate a three dimensional array of atoms corresponding to the repetition of a basic cell. This procedure might include (or not) the relaxation of the atomic positions based on a potential function. Output files corresponding to a set of fully ordered and a set of chemically disordered intermetallics have been prepared with the aid of CREATOR, a lattice generator software which describes all the atomic positions for a given crystal geometry, either mathematically relaxed or not. These well defined crystals are to be used as a calibration. The detailed description of these raw models is presented in Table 3.2.

Table 3.2: Raw models for image simulation calibration.

Material	Size [atoms]	Dimensions [nm³]	Disorder [at.%]	Radius [nm]
NiAl	128000	11.5×11.5×11.5	4.3	2.5
Ni₃Al	256000	14.3×14.3×14.3	2.2	2.5

The construction of a fully disordered lattice is achieved by generating the atomic positions at random in accord to the intermetallic stoichiometry. A disordered nucleus is geometrically embedded into the ordered matrix to model a partially disordered crystal. This operation encloses the disordered material within a known boundary and restricts it to a fraction of the total volume (Table 3.2). The knowledge of the exact geometry of this object enables the correlation between atomic lattice positions and the simulated image in both phase and diffraction contrast modes.

A more sophisticated approach to create an irradiation-induced disordered virtual specimen is to generate a relaxed crystal as an MD input and to introduce a PKA of appropriate direction and primary energy. This procedure simulates cascade damage evolution and it may be followed as a function of time. The simulation is interrupted after the quenching phase and the crystal is subsequently annealed in order to relax the post-mortem atomic structure. For this purpose a set of crystals were built and simulated
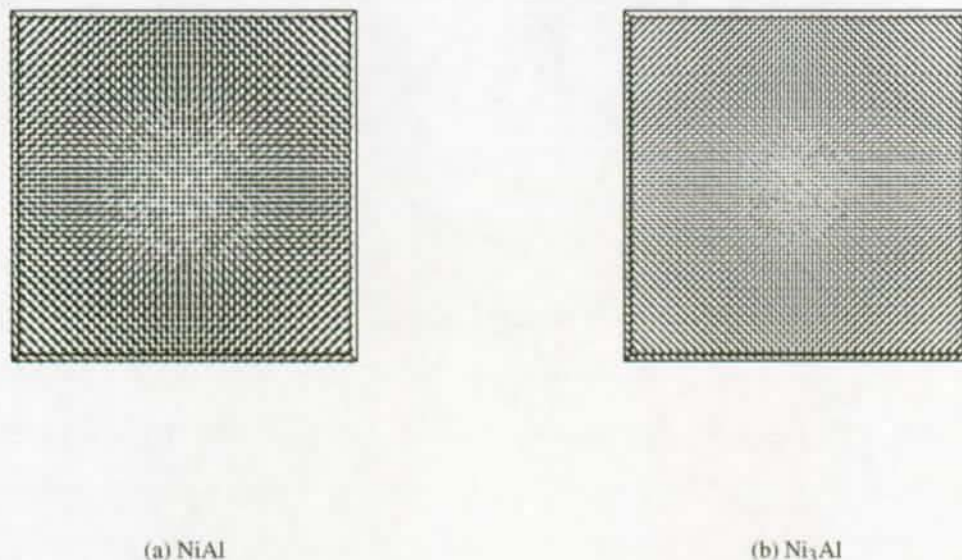
(a) NiAl   (b) Ni₃Al

Figure 3.2: Topological cut across the [001] direction in (a) NiAl and (b) Ni₃Al ordered matrices containing a disordered nucleus of 2.5 nm radius. Original crystal dimensions are $40 \times 40 \times 40$ unit cells.

under cascade damage production (Spaczér 1995, Almazouzi 1999). These virtual specimens are then sorted into an intermetallic group (Table 3.3) and a pure metallic group (Table 3.4), the purpose being to differentiate basic aspects of radiation damage in ordered compounds and pure metals.

Table 3.3: Cascade damage image simulation matrix in intermetallics.

Mater.	Size [at]	E_{PKA} [keV]	HRTEM		CTEM	
			Ap. [nm^{-1}]	Defocus [nm]	Ap. [nm^{-1}]	Condition
NiAl	194672	10	25.0	Scherzer	1.25	$\vec{g}(1.1\vec{g}), \vec{g}(3.1\vec{g})$
NiAl	128000	15	25.0	Scherzer	1.25	$\vec{g}(1.1\vec{g}), \vec{g}(3.1\vec{g})$
Ni₃Al	256000	10	25.0	Scherzer	1.25	$\vec{g}(1.1\vec{g}), \vec{g}(3.1\vec{g})$
Ni₃Al	256000	15	25.0	Scherzer	1.25	$\vec{g}(1.1\vec{g}), \vec{g}(3.1\vec{g})$

The virtual specimens containing atomic positions are cut perpendicularly to the electron beam direction in slices that are 0.2 nm thick. The multislice calculation using the EMS software is aimed at obtaining the wave function at the exit surface of the sample and the subsequent TEM image from the microscope optical parameters. The approach was applied successfully in the case of a 2 nm stacking fault tetrahedron in Cu (Schäublin et al. 1998) and a nanometric interstitial type dislocation loop in Al (Schäublin, Almazouzi, Osetsky & Victoria 2000) using weak-beam imaging (Cockayne et al. 1969). This methodology has been applied for the first time to the case of ordered intermetallics using both dark-field and

Table 3.4: Cascade damage image simulation matrix in pure metals.

Mater.	Size [at]	E_{PKA} [keV]	HRTEM Ap. [nm^{-1}]	HRTEM Defocus [nm]	CTEM Ap. [nm^{-1}]	CTEM Condition
Al	340736	10	25.0	Scherzer	2.50	$\vec{g}(3.1\vec{g})$
Ni	500000	30	25.0	Scherzer	2.50	$\vec{g}(3.1\vec{g})$

weak-beam imaging modes (de Almeida et al. 1999) and will be described here in detailed form.

The parameters used to derive the images in HRTEM are those that are close to both a common HRTEM observation and the characteristics of a modern microscope with an acceleration voltage of 200 kV (electron wavelength, $\lambda = 2.51$ pm). The beam semi-convergence is 1.0 mrad, the defocus spread 10 nm and the coefficient of the spherical aberration (C_s) 1.4 mm. The images were extracted from through focus series including the Scherzer defocus, $\Delta f = (1.5C_s\lambda)^{1/2} = 73.0$ nm, which results in the strongest crystal contrast, corresponding to a point-to-point resolution of $0.64(C_s\lambda^3)^{1/4} = 0.25$ nm. The objective aperture diameter of 25.0 nm^{-1} allows to obtain a high resolution image with a spatial frequency cut off at 0.08 nm. In the case of the CTEM images the sample was set in focus (no defocus). The C_s value, the defocus spread and the beam semi-convergence are not considered. The objective aperture diameter is chosen in order to select only one diffraction spot, either transmitted or diffracted. In the present case it appears that an objective aperture between 1.25 nm^{-1} and 2.50 nm^{-1} in diameter corresponds to the usual experimental condition, whereby the objective aperture size is about two thirds of the diffraction vector length (Table 3.5).

A dark-field (DF) or a weak-beam dark-field (WBDF) condition is obtained by tilting the virtual specimen from a [001] to a [015] zone axis (ZA), which means the specimen is only rotated along the x-axis making an off-set angle of 11° with the z-axis, and by exciting the corresponding diffraction vector through the intersection of the appropriate Laue circle. Tilting from a primary (Figures 3.3(a), 3.4(a), and 3.5(a)) to a non-primary ZA (Figures 3.3(b), 3.4(b), and 3.5(b)) is a first approximation to a virtual kinematical diffraction condition. In the case of ordered intermetallics (Figures 3.3 and 3.4), a diffraction vector corresponding to the superlattice reflection $\vec{g} = (100)$ is used in the DF mode whereas $\vec{g} = (200)$ is used in the WBDF $\vec{g}(3.1\vec{g})$ imaging condition. In the pure metal cases (e.g. Figure 3.5), due to the absence of chemical order, only the fundamental diffraction vector $\vec{g} = (200)$ is used in the WBDF imaging condition.

The sampling interval, Δx, should be between 1/4 and 1/3 of the real point-to-point resolution (Kirkland 1998). For the case of nickel, the maximum sampling rate achievable in a 512×512 discretization is

Table 3.5: Diffraction vector lengths.

| g [nm^{-1}]	NiAl	Ni$_3$Al	Al	Ni
(100)	3.46	2.80		
(200)	6.93	5.60	4.96	5.68

$k_{max} = N/2a_x = 15$ pixels/nm, where N is the number of pixels in the x-direction (or y), and a_x is the size of the sample. If the sampling is done at intervals of one third of the point-to-point resolution, 0.0833 nm, a rate of 12 pixels/nm is needed; if the sampling is chosen to be one quarter of the point-to-point resolution, 0.0625 nm, a sampling rate of 16 pixels/nm should be used and the sampling process must be scaled up by a factor 2 in each direction (1024×1024). Higher sampling increases the number of computations with N^2. Therefore, the sampling of the image defined for the fast Fourier transform (FFT) involved in the multislice calculation is then usually set to 512×512 pixels. For the sample sizes that are considered here (about a quarter of a million atoms) this sampling appears to be sufficient. The use of a higher sampling (1024×1024), together with the disadvantage of increasing the calculation time, resulted in approximately the same final image. The effect of sampling in CTEM imaging mode is not as sensitive as in HRTEM due to the choice of a smaller aperture diameter which works as a low-pass spatial filter in order to limit the number of diffracted beams.

3.4 HRTEM image simulation of intermetallics

Phase contrast image simulation of the purely disordered 2.5 nm radius sphere in NiAl and in Ni$_3$Al has been made using the virtual microscope parameters mentioned in section 3.3. The specimens have been oriented to a [001] ZA and the set of images has been extracted from through focus series (-20 nm up to 130 nm). Maximum contrast arises at Scherzer defocus (highest spatial frequency transfer) although it is clearly demonstrated here that a much lower defocus may be used in order to enhance the type of contrast produced by the crystal defects. In both intermetallics (Figures 3.6 and 3.7) it is possible to identify the disordered sphere, even though at intermediate defoci the contrast may significantly decrease. At lower defocus (Figures 3.6(a) and 3.7(a)) a particular type of contrast is formed in the interior of the disordered material ("orange-skin" type) which is used later on as reference when simulating irradiation-induced disorder by displacement cascades. At Scherzer defocus the information of the image is maximized although, as mentioned earlier, the local information embedded into the disordered sphere is reduced (Figures 3.6(b) and 3.7(b)).
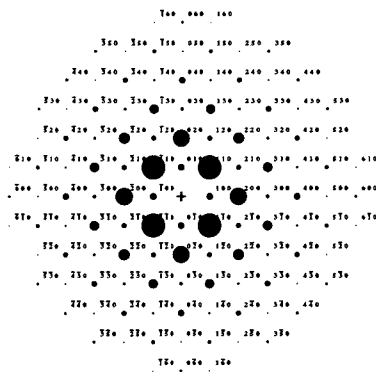
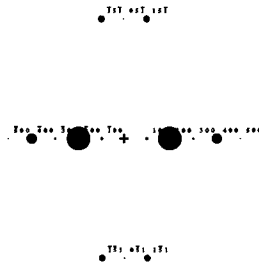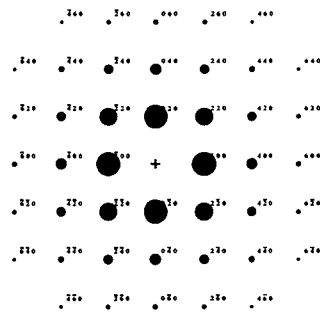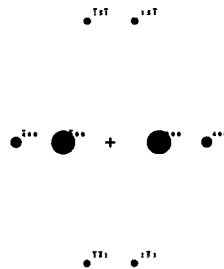(a) $\vec{g}_1 = (100) / \vec{g}_2 = (010) / \vec{g}_3 = (001) / [001]$ ZA
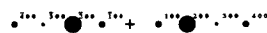
(b) $\vec{g}_1 = (100) / \vec{g}_2 = (05\bar{1}) / \vec{g}_3 = (010) / [015]$ ZA

Figure 3.3: Selected area diffraction (SAD) patterns for an ordered matrix of NiAl along the (a) [001] and (b) [015] zone axis (ZA).
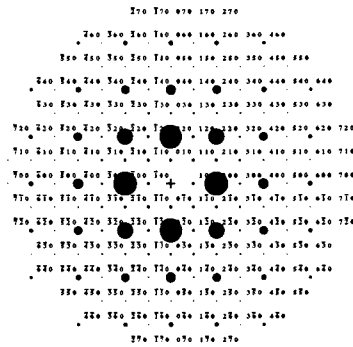
(a) $\vec{g}_1 = (100)$ / $\vec{g}_2 = (010)$ / $\vec{g}_3 = (001)$ / [001] ZA

(b) $\vec{g}_1 = (100)$ / $\vec{g}_2 = (05\bar{1})$ / $\vec{g}_3 = (010)$ / [015] ZA

Figure 3.4: Selected area diffraction (SAD) patterns for an ordered matrix of Ni_3Al along the (a) [001] and (b) [015] zone axis (ZA).

(a) $\vec{g}_1 = (100) / \vec{g}_2 = (010) / \vec{g}_3 = (001) / [001]$ ZA

(b) $\vec{g}_1 = (100) / \vec{g}_2 = (05\bar{1}) / \vec{g}_3 = (010) / [015]$ ZA

Figure 3.5: Selected area diffraction (SAD) patterns for a matrix of Ni along the (a) [001] and (b) [015] zone axis (ZA).

Molecular dynamics (MD) computer simulation has been used to produce the cascades in both inter-metallics (Spaczér 1995) under different irradiation conditions (Table 3.3). These virtual specimens were subsequently studied in phase contrast imaging mode and compared to the reference cases.

3.4.1   10 keV energy recoils

Under a 10 keV energy recoil NiAl shows a highly disordered region corresponding to the post-mortem cascade of comparable contrast as the chemically disordered sphere. At low defocus the object is perfectly visible (Figure 3.8(a)) whereas at Scherzer it almost disappears (Figure 3.8(b)). Under an equivalent recoil energy no remarkable effect is produced in Ni_3Al. At both defoci (Figures 3.9(a) and 3.9(b)), the damaged region remains almost undistinguished from the matrix, which means the amount of disorder induced in the crystalline lattice is barely detectable.

3.4.2   15 keV energy recoils

The damage produced under a 15 keV recoil in NiAl induces a disordered region visible in both defoci (Figures 3.10(a) and 3.10(b)) of contrast comparable to the raw model. Moreover, a dark contrast may indicate the presence of a structural defect in the lattice or the formation of a secondary phase. At an equivalent recoil energy there are no indications of a highly defected lattice in Ni_3Al nor of extensive disordered regions in both defoci (Figures 3.11(a) and 3.11(b)).

3.4.3   2×15 keV energy recoils: damage accumulation

Damage accumulation is of paramount importance in radiation studies. For this purpose a set of virtual specimens has been produced via two 15 keV energetic recoils and studied in phase contrast imaging mode. The damage induced in NiAl (no coupling and weak coupling cases) creates a region of high chemical disorder visible at both defoci (Figures 3.12(a), 3.12(b), 3.13(a), and 3.13(b)) of contrast comparable to the raw model. The dark contrast bordering the central region of the cascade is indicative of topological disorder, eventually of amorphization. Under an equivalent recoil energy there are no indications of a highly defected lattice in Ni_3Al. The object is visible in both defoci (Figures 3.14(a) and 3.14(b)) with a contrast equal to the reference case indicating an irradiation-induced chemically disordered region.

(a) -20 nm defocus   (b) Scherzer defocus, 73 nm
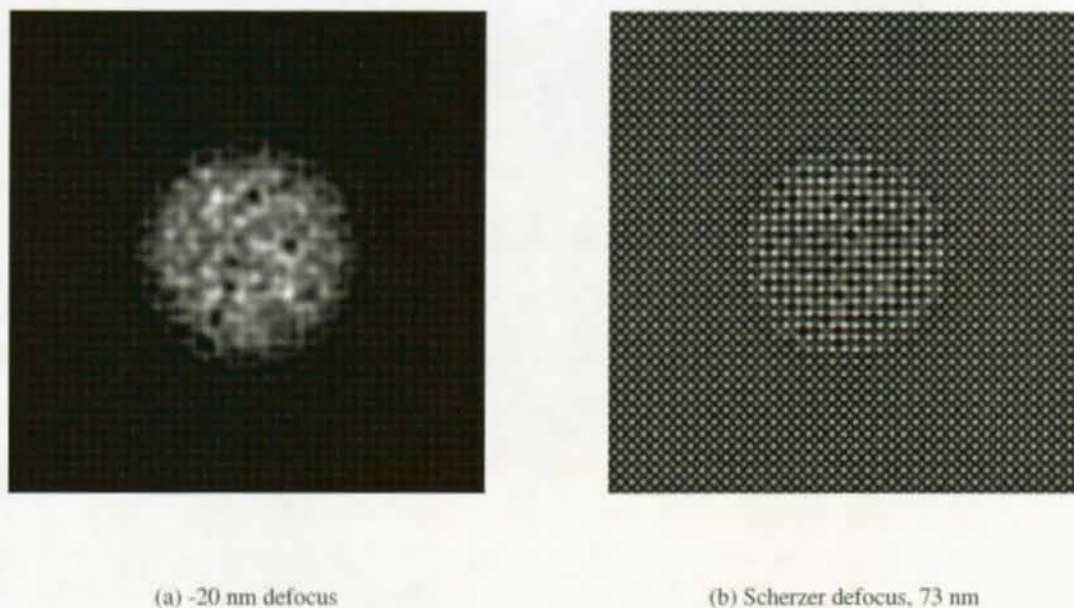
Figure 3.6: HRTEM image simulation showing the chemical disorder inside an ordered matrix of NiAl $40\times40\times40$ unit cells containing a disordered nucleus of 2.5 nm radius (4.3% atomic fraction) tilted to [001] ZA at (a) -20 nm defocus and (b) Scherzer defocus.
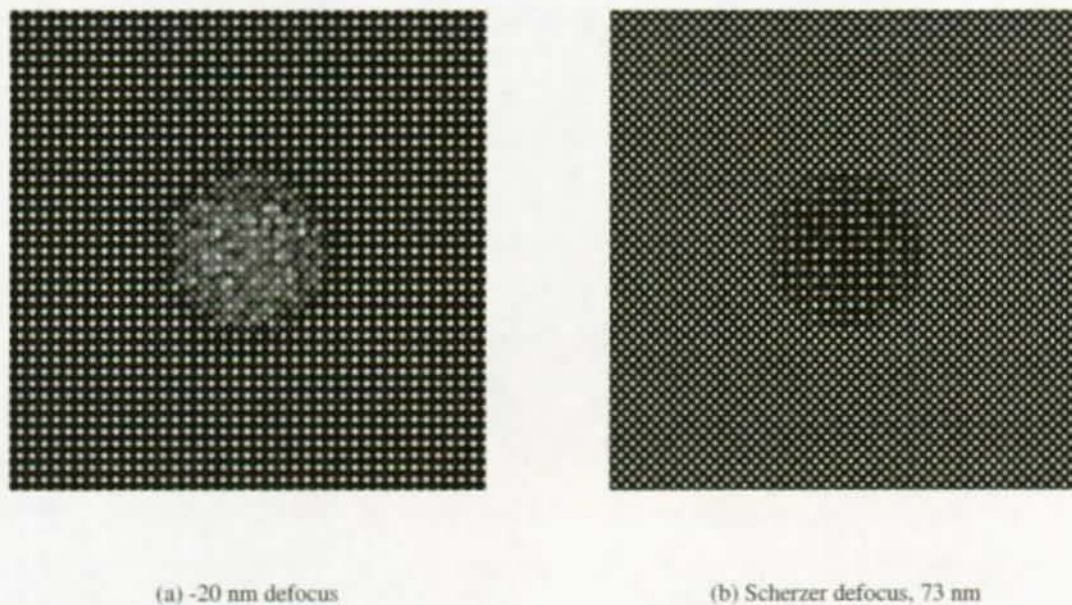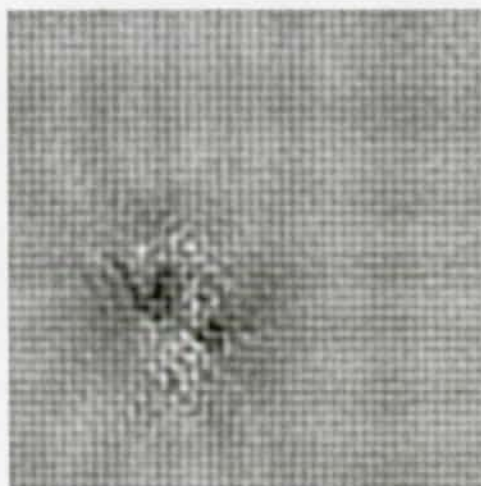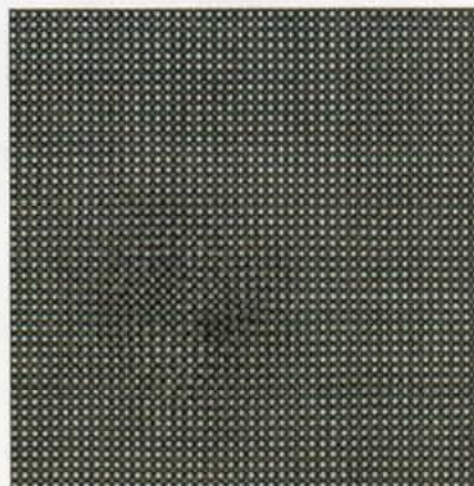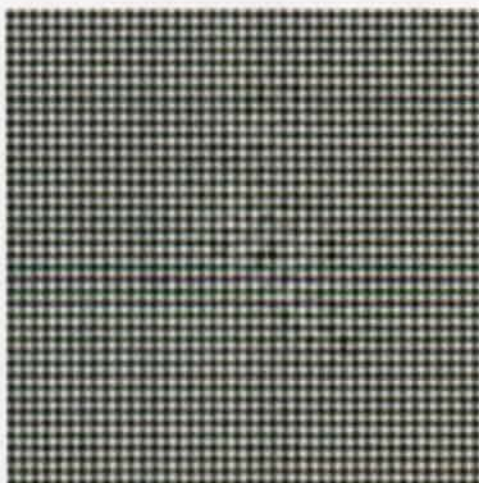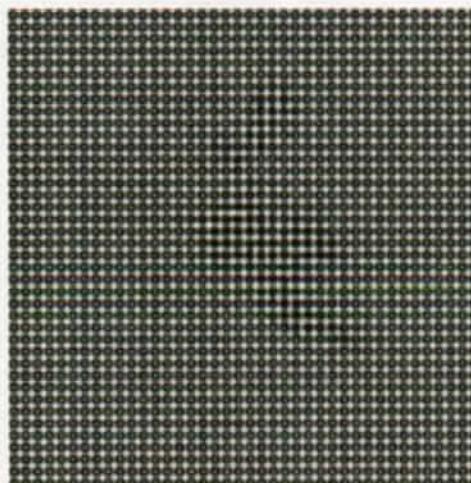

(a) -20 nm defocus   (b) Scherzer defocus, 73 nm

Figure 3.7: HRTEM image simulation showing the chemical disorder inside an ordered matrix of Ni_3Al $40\times40\times40$ unit cells containing a disordered nucleus of 2.5 nm radius (2.2% atomic fraction) tilted to [001] ZA at (a) -20 nm defocus and (b) Scherzer defocus.
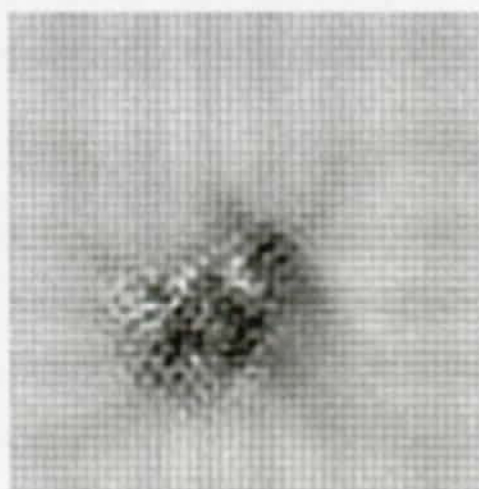
(a) -20 nm defocus   (b) Scherzer defocus, 73 nm

Figure 3.8: HRTEM image simulation of a cascade induced by a 10 keV PKA after 12.3 ps (weak coupling), inside a matrix of NiAl $46\times46\times46$ unit cells tilted to [001] ZA at (a) -20 nm defocus and (b) Scherzer defocus.

(a) -20 nm defocus   (b) Scherzer defocus, 73 nm

Figure 3.9: HRTEM image simulation of a cascade induced by a 10 keV PKA after 10.8 ps (weak coupling), inside a matrix of Ni_3Al $40\times40\times40$ unit cells tilted to [001] ZA at (a) -20 nm defocus and (b) Scherzer defocus.
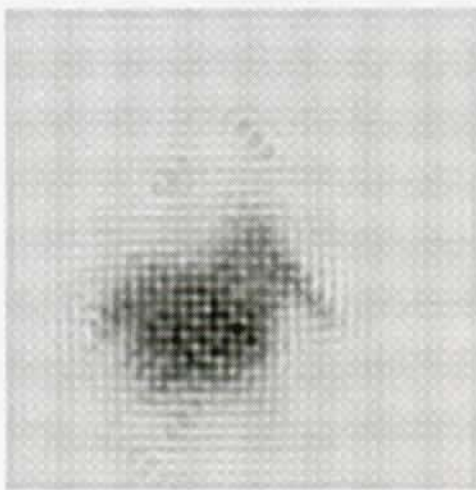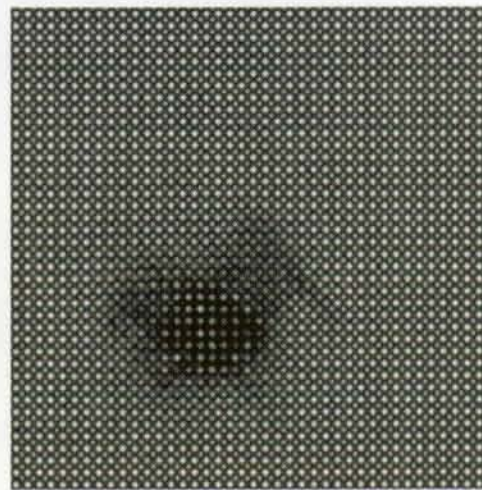
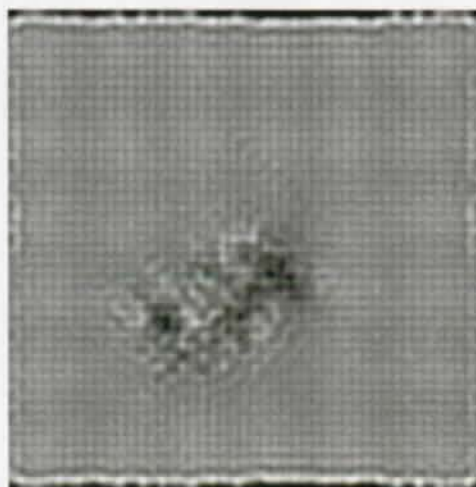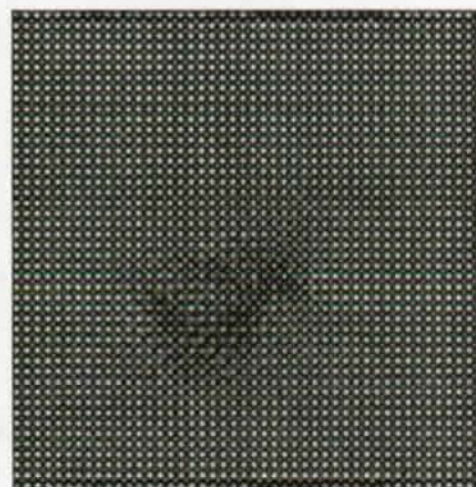(a) -20 nm defocus   (b) Scherzer defocus, 73 nm

Figure 3.10: HRTEM image simulation of a cascade induced by a 15 keV PKA after 13.0 ps (weak coupling), inside a matrix of NiAl $40 \times 40 \times 40$ unit cells tilted to [001] ZA at (a) -20 nm defocus and (b) Scherzer defocus.
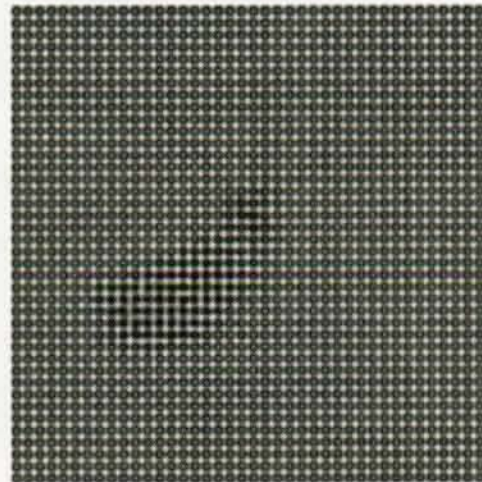
(a) -20 nm defocus   (b) Scherzer defocus, 73 nm

Figure 3.11: HRTEM image simulation of a cascade induced by a 15 keV PKA after 10.0 ps (weak coupling), inside a matrix of Ni_3Al $40 \times 40 \times 40$ unit cells tilted to [001] ZA at (a) -20 nm defocus and (b) Scherzer defocus.
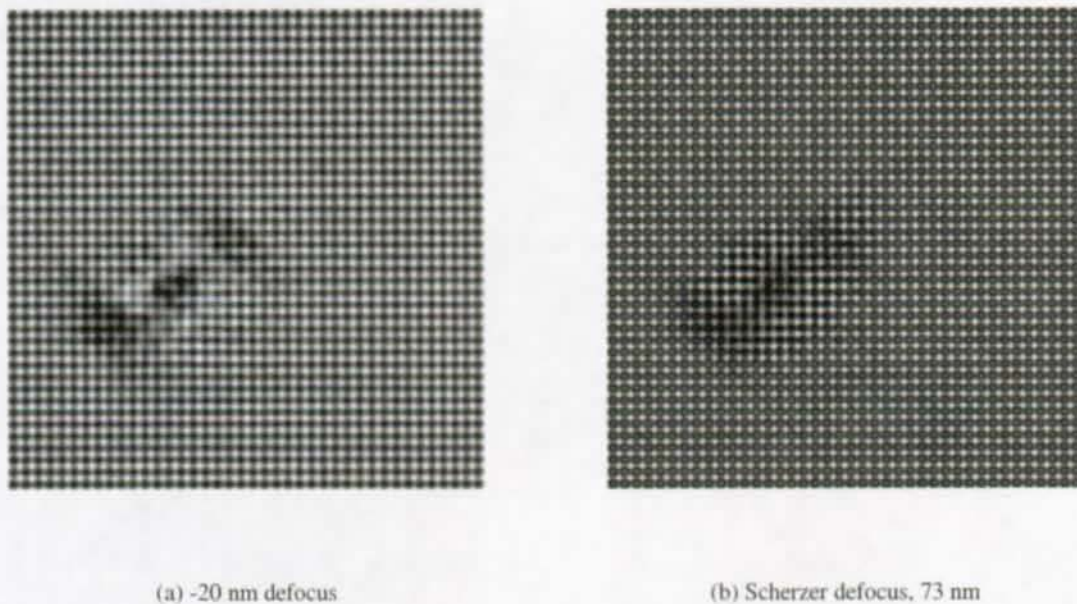
(a) -20 nm defocus

(b) Scherzer defocus, 73 nm

Figure 3.12: HRTEM image simulation of cascade damage induced by two 15 keV PKA's after 36.0 ps (no coupling), inside a matrix of NiAl $46 \times 46 \times 46$ unit cells tilted to [001] ZA at (a) -20 nm defocus and (b) Scherzer defocus.

(a) -20 nm defocus

(b) Scherzer defocus, 73 nm

Figure 3.13: HRTEM image simulation of cascade damage induced by two 15 keV PKA's after 20.0 ps (weak coupling), inside a matrix of NiAl $46 \times 46 \times 46$ unit cells tilted to [001] ZA at (a) -20 nm defocus and (b) Scherzer defocus.

(a) -20 nm defocus

(b) Scherzer defocus, 73 nm

Figure 3.14: HRTEM image simulation of cascade damage induced by two 15 keV PKA's after 13.0 ps (weak coupling), inside a matrix of Ni_3Al $40 \times 40 \times 40$ unit cells tilted to [001] ZA at (a) -20 nm defocus and (b) Scherzer defocus.

3.5   CTEM image simulation of intermetallics

To image irradiation-induced defects, the WBDF imaging condition is used to image strain fields of defect clusters (Cockayne et al. 1969). In irradiation-induced order-disorder studies of chemically ordered intermetallics it is mandatory to identify the disordered regions produced by the displacement cascade through a DF using a superlattice reflection (Hirsch et al. 1977).

The two intermetallics have been simulated using equivalent image conditions both in DF and WBDF imaging modes. The crystals have been tilted and cut to a [015] ZA in order to preserve the periodic boundary conditions of the box. The position of the diffraction vectors is determined by FFT in one of the crystal slices (a plane of 0.2 nm thickness). Further image tilt is achieved by shearing the crystal box so that a WBDF and a DF condition can be reached in the virtual microscope. The parameters that have been used in diffraction contrast imaging correspond to the ones mentioned in section 3.3. As means of reference an image simulation of chemical disorder inside an ordered matrix of Ni_3Al containing a disordered nucleus of 2.5 nm radius has been done in DF and WBDF imaging conditions (Figure 3.15). It can be seen that the chemically disordered sphere appears clearly as a dark contrast in the DF image (Figure 3.15(a)). The WBDF $\vec{g}(3.1\vec{g})$ imaging condition is intended to show that the sphere does not contain any defect cluster in its interior (Figure 3.15(b)). This means that only chemical disorder contributes to create the image contrast when using a superlattice reflection of type (100). The displacement cascades produced in both intermetallics were simulated in the virtual microscope using diffraction contrast mode.

3.5.1   10 keV energy recoils

Radiation damage induced via a 10 keV recoil creates a disordered region in both intermetallics which is readily identified (Figures 3.16(a) and 3.17(a)) under DF imaging mode using a superlattice reflection $\vec{g} = (100)$. These regions are directly related to the disordering induced by the cascade. During this fast process the displaced atoms can cluster and eventually form stable defects that survive after the cascade. The WBDF $\vec{g}(3.1\vec{g})$ imaging condition is simulated to identify lattice defects. It is possible to see that either in the case of NiAl (Figure 3.16(b)) or Ni_3Al (Figure 3.17(b)), defect clusters are formed both at the interior and at the exterior of the disordered regions. There is no evidence whatsoever of amorphization.

3.5.2 15 keV energy recoils

In the two intermetallics a disordered region is readily identified (Figures 3.18(a) and 3.19(a)) under DF imaging using a superlattice reflection $\vec{g} = (100)$. The WBDF $\vec{g}(3.1\vec{g})$ imaging condition is simulated to identify any type of defects. If a qualitative analysis is done in order to relate the disordered regions and the defects it is possible to see that in the case on NiAl the cluster is formed at the interior of the disordered region and that in Ni_3Al there are two defects outside the disordered zone. Moreover, under high-energy cascade production in NiAl, partial amorphization arises (Figure 3.18(c)) in accord to the analysis performed on MD computer simulations. The amorphous regions are small and are trapped inside the disordered region. The defect cluster is rather close to the amorphous material indicating that the maximum amount of damage occurs in a very restricted volume of the original cascade.

3.5.3 2×15 keV energy recoils: damage accumulation

The damage induced in the crystalline lattice via two 15 keV energetic recoils creates a region of chemical disorder in both intermetallics (Figures 3.20(a), 3.21(a), and 3.22(a)) independently of the electron-phonon coupling magnitude. The WBDF $\vec{g}(3.1\vec{g})$ imaging mode is simulated to identify any surviving defects in these intermetallics. A set of clusters is visible in each specimen (Figures 3.20(b), 3.21(b), and 3.22(b)) bordering the disordered region. Partial amorphization takes place in NiAl only when a weak coupling has been deployed (Figure 3.21(c)). There is no evidence of amorphization of Ni_3Al at an equivalent irradiation condition.
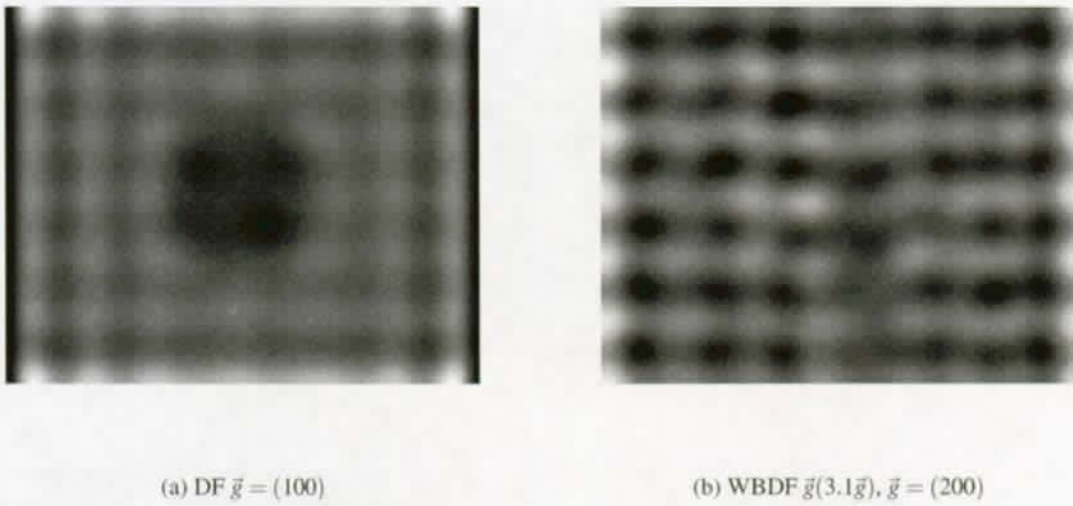
(a) DF $\vec{g} = (100)$

(b) WBDF $\vec{g}(3.1\vec{g})$, $\vec{g} = (200)$

Figure 3.15: CTEM image simulation showing the chemically disordered nucleus inside an ordered matrix of Ni_3Al $40\times40\times40$ unit cells (original box) cut and tilted to $[015]$ ZA on a (a) DF under chemical order reflection $\vec{g} = (100)$ and (b) WBDF $\vec{g}(3.1\vec{g})$, $\vec{g} = (200)$, showing the effect of the periodicity error.
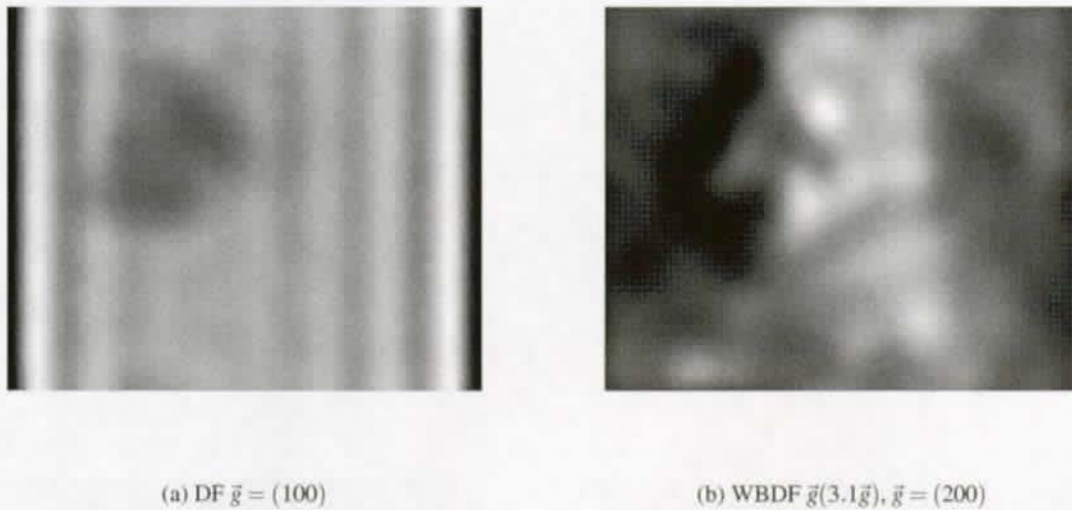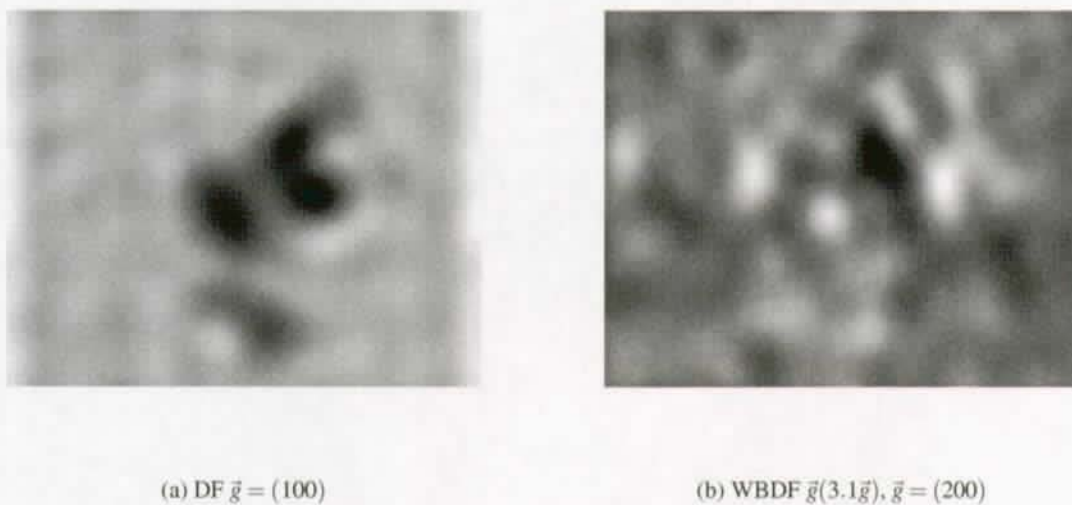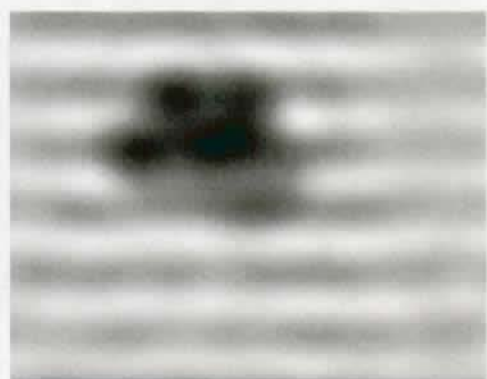
(a) DF $\vec{g} = (100)$ (b) WBDF $\vec{g}(3.1\vec{g})$, $\vec{g} = (200)$

Figure 3.16: CTEM image simulation of a cascade induced by a 10 keV PKA after 12.3 ps (weak coupling), inside a matrix of NiAl 46×46×46 unit cells (original box) cut and tilted to [015] ZA. (a) DF under chemical order reflection $\vec{g} = (100)$ and (b) WBDF $\vec{g}(3.1\vec{g})$, $\vec{g} = (200)$.

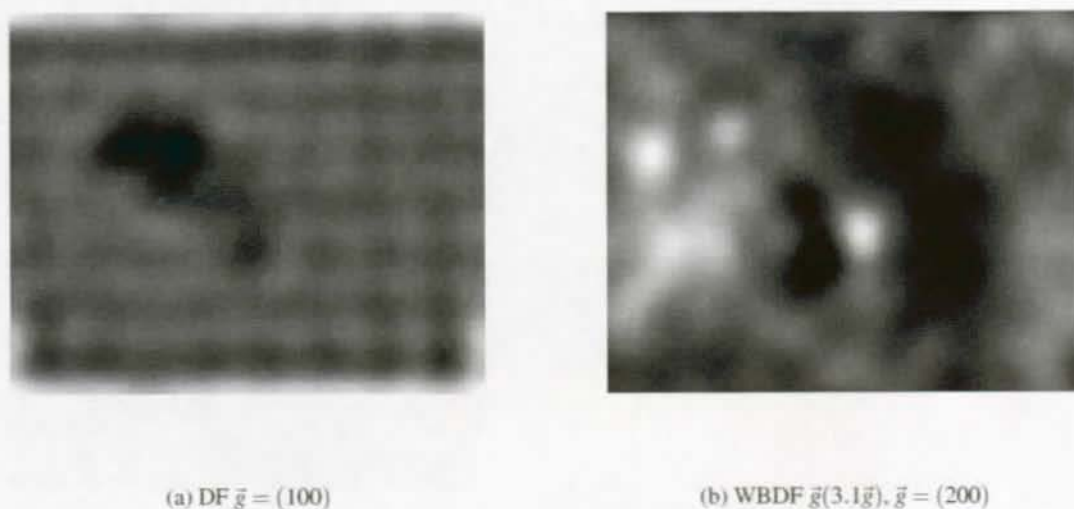(a) DF $\vec{g} = (100)$ (b) WBDF $\vec{g}(3.1\vec{g})$, $\vec{g} = (200)$

Figure 3.17: CTEM image simulation of a cascade induced by a 10 keV PKA after 10.8 ps (weak coupling), inside a matrix of Ni$_3$Al 40×40×40 unit cells (original box) cut and tilted to [015] ZA. (a) DF under chemical order reflection $\vec{g} = (100)$ and (b) WBDF $\vec{g}(3.1\vec{g})$, $\vec{g} = (200)$.

(a) DF $\vec{g} = (100)$

(b) WBDF $\vec{g}(3.1\vec{g})$, $\vec{g} = (200)$

(c) DF (using the amorphous diffraction ring)

Figure 3.18: CTEM image simulation of a cascade induced by a 15 keV PKA after 13.0 ps (weak coupling), inside a matrix of NiAl $40 \times 40 \times 40$ unit cells (original box) cut and tilted to [015] ZA. (a) DF under chemical order reflection $\vec{g} = (100)$, (b) WBDF $\vec{g}(3.1\vec{g})$, $\vec{g} = (200)$ and (c) DF using the amorphous ring.
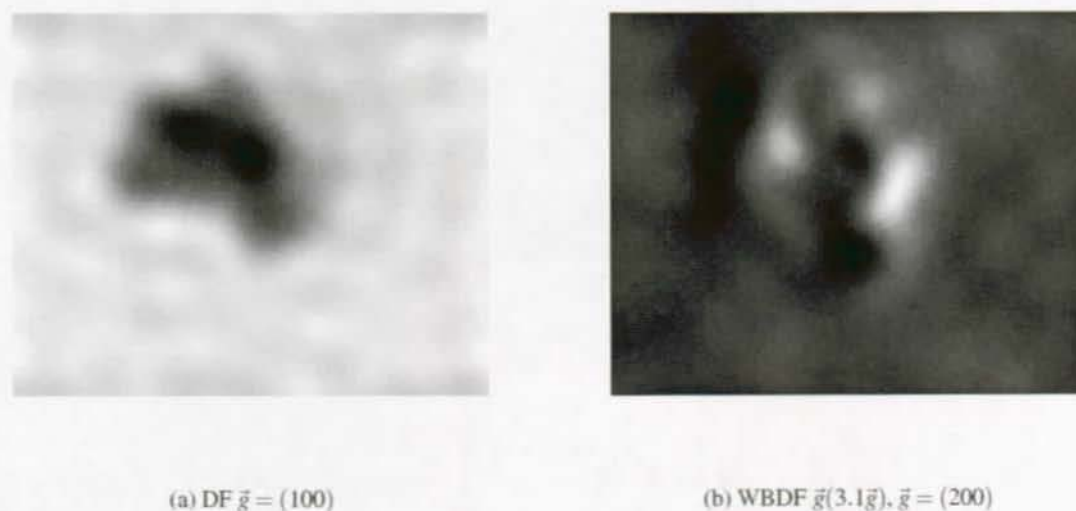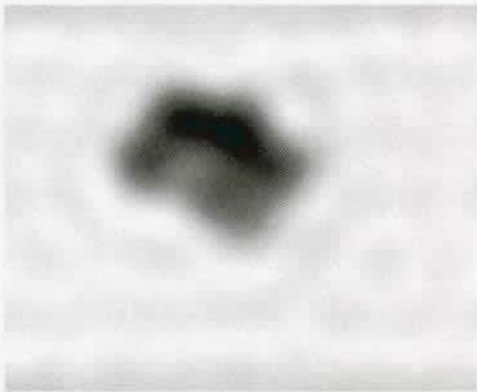
(a) DF $\vec{g} = (100)$

(b) WBDF $\vec{g}(3.1\vec{g})$, $\vec{g} = (200)$

Figure 3.19: CTEM image simulation of a cascade induced by a 15 keV PKA after 10.0 ps (weak coupling), inside a matrix of Ni_3Al $40 \times 40 \times 40$ unit cells (original box) cut and tilted to [015] ZA. (a) DF under chemical order reflection $\vec{g} = (100)$ and (b) WBDF $\vec{g}(3.1\vec{g})$, $\vec{g} = (200)$.

(a) DF $\vec{g} = (100)$

(b) WBDF $\vec{g}(3.1\vec{g})$, $\vec{g} = (200)$

Figure 3.20: CTEM image simulation of cascade damage induced by two 15 keV PKA's after 36.0 ps (no coupling), inside a matrix of NiAl $46 \times 46 \times 46$ unit cells (original box) cut and tilted to [015] ZA. (a) DF under chemical order reflection $\vec{g} = (100)$ and (b) WBDF $\vec{g}(3.1\vec{g})$, $\vec{g} = (200)$.

(a) DF $\vec{g} = (100)$

(b) WBDF $\vec{g}(3.1\vec{g})$, $\vec{g} = (200)$
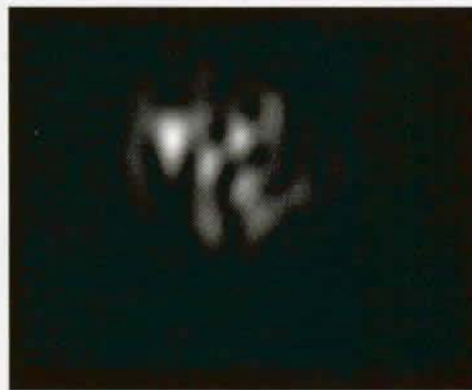
(c) DF (using the amorphous diffraction ring)

Figure 3.21: CTEM image simulation cascade damage induced by two 15 keV PKA's after 20.0 ps (weak coupling), inside a matrix of NiAl 46×46×46 unit cells (original box) cut and tilted to [015] ZA. (a) DF under chemical order reflection $\vec{g} = (100)$, (b) WBDF $\vec{g}(3.1\vec{g})$, $\vec{g} = (200)$ and (c) DF using the amorphous ring.
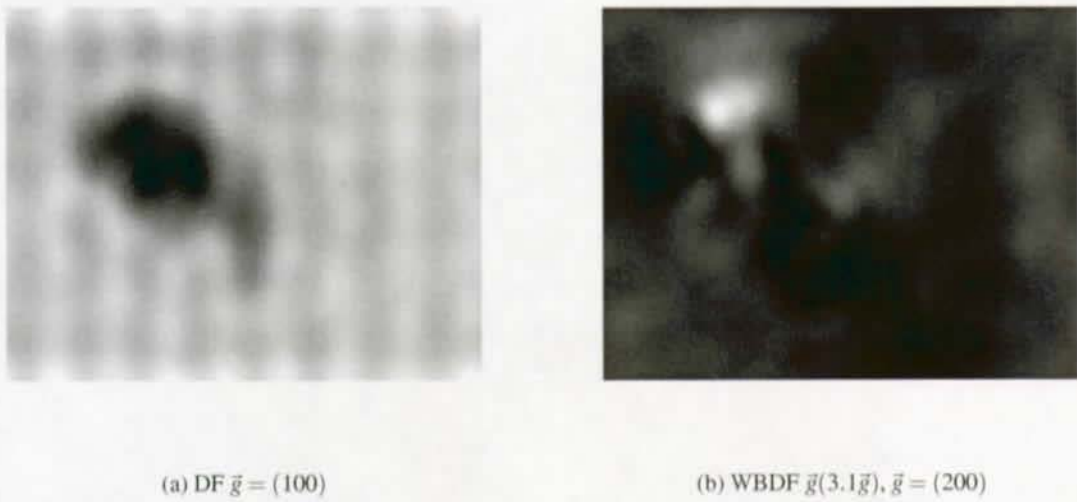
(a) DF $\vec{g} = (100)$ (b) WBDF $\vec{g}(3.1\vec{g})$, $\vec{g} = (200)$

Figure 3.22: CTEM image simulation of cascade damage induced by two 15 keV PKA's after 13.0 ps (weak coupling), inside a matrix of Ni_3Al $40 \times 40 \times 40$ unit cells (original box) cut and tilted to [015] ZA. (a) DF under chemical order reflection $\vec{g} = (100)$ and (b) WBDF $\vec{g}(3.1\vec{g})$, $\vec{g} = (200)$.

3.6   HRTEM image simulation of pure metals

Molecular dynamics (MD) computer simulation has been used to produce a 10 keV and a 30 keV displacement cascade in aluminium and nickel (Almazouzi 1999), respectively (Table 3.4). These virtual specimens were subsequently simulated in phase contrast imaging mode.

The defect production induced via a 10 keV recoil in aluminium is observable at both defoci (Figures 3.23(a) and 3.23(b)). Interstitial clusters produce a strong white contrast of uniform intensity whereas vacancy clusters produce a faint gray one. Individual interstitials produce an open circle feature and vacancies produce a white dot contrast. The nature of the defects can be identified with this technique by observing a sample at Scherzer. The same results are expected at defoci above and below Scherzer despite the contrast inversions and the reduction on image resolution. Imaging out of Scherzer can be explored with advantages in order to increase the visibility of the defect by Fresnel interference.

The image simulation of a 30 keV recoil in nickel shows the defect production distribution projected into the xy-plane visible in both defoci (Figures 3.24(a) and 3.24(b)). It is possible to identify distinct types of defects and clusters of defects. Each defect, either interstitial or vacancy, has a different fingerprint. Interstitial and vacancy clusters produce a white and a faint gray contrast, respectively, whereas individual interstitials produce an open circle feature and vacancies produce a white dot contrast.

3.7   CTEM image simulation of pure metals

Diffraction contrast image simulation of nickel and aluminium were made in similar conditions. Both images are WBDF $\vec{g}(3.1\vec{g})$, with $\vec{g} = (200)$. The tilting of the crystal box to a non-primary ZA induces an atomic surface roughness which appears in the image as low-frequency spatial noise. Nevertheless, the stress field created by the defects can be correctly imaged.

The image formed in the case of aluminium presents great detail (Figure 3.25). A defect cluster with a strong white contrast is visible as well as a background contrast oscillation, which indicates a long-range stress field. Due to the oscillations of the contrast transfer function some defects may not be visible under the chosen diffraction condition.

It is possible to identify a defect cluster in nickel (Figure 3.26) at the center of the image (strong white contrast region) surrounded by a faint gray contrast level that vanishes into the black matrix contrast. Due to the signal inversion of the contrast transfer function some of the defects present in the bulk may be invisible when performing an image at the total thickness of the sample.
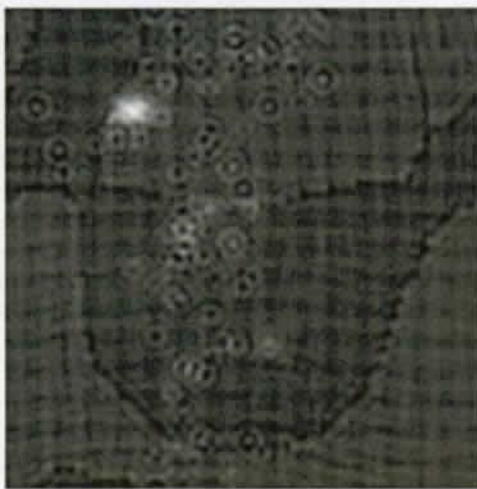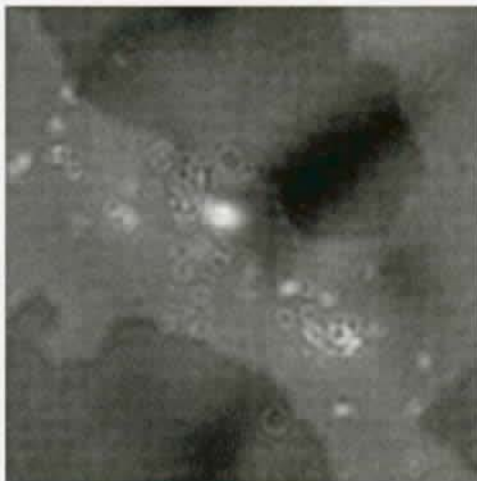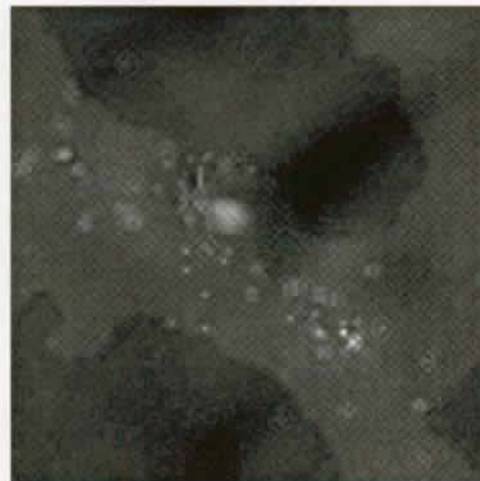
(a) -20 nm defocus

(b) Scherzer defocus, 73 nm

Figure 3.23: HRTEM image simulation of a cascade induced by a 10 keV PKA after 30.0 ps (weak coupling), inside a matrix of Al $44\times44\times44$ unit cells tilted to [001] ZA at (a) -20 nm defocus and (b) Scherzer defocus.

(a) -20 nm defocus

(b) Scherzer defocus, 73 nm

Figure 3.24: HRTEM image simulation of a cascade induced by a 30 keV PKA after 30.0 ps (weak coupling), inside a matrix of Ni $50\times50\times50$ unit cells tilted to [001] ZA at (a) -20 nm defocus and (b) Scherzer defocus.

Figure 3.25: CTEM image simulation of a cascade induced by a 10 keV PKA after 30.0 ps (weak coupling), inside a matrix of Al $44\times44\times44$ unit cells (original box) cut and tilted to [015] ZA in WBDF $\vec{g}(3.1\vec{g})$, $\vec{g} = (200)$ condition.

Figure 3.26: CTEM image simulation of a cascade induced by a 30 keV PKA after 30.0 ps (weak coupling), inside a matrix of Ni $50\times50\times50$ unit cells (original box) cut and tilted to [015] ZA in WBDF $\vec{g}(3.1\vec{g})$, $\vec{g} = (200)$ condition.

3.8 Summary

Both HRTEM and CTEM imaging modes are used on MD samples in order to extract valuable information of the microstructural evolution under cascade production which can be directly compared to real experimental results (Jenkins et al. 1976, Jenkins & English 1982, English & Jenkins 1987, Bui et al. 1995, Müller et al. 1997, Ewert 1998).

The image simulation technique proves to be a refined tool in aiding to understand the image contrast formation of irradiation-induced disordered regions and defect clusters in ordered intermetallics (de Almeida et al. 1999) and pure metals (Schäublin, de Almeida, Almazouzi & Victoria 2000).

It appears that in HRTEM imaging mode, defoci values below Scherzer are better to image crystal defects, and in particular disordered regions. For the first time a DF condition was successfully reproduced using superlattice reflections in CTEM imaging mode to assess the extent of the irradiation-induced disordered regions under cascade damage. The WBDF imaging condition was applied to image the surviving lattice defects upon quenching. A correlation between the disordered region and the loci of the defect clusters is observed.

Chapter 4

Transmission electron microscopy of the irradiated microstructure

Transmission electron microscopy of irradiation induced defects is known to be an invaluable, delicate experimental technique. Microstructural studies are, however, extremely localized. For this purpose, a certain number of imaging techniques have been explored in order to extract information regarding irradiation induced disordering and defect cluster formation in both NiAl and Ni_3Al. Disordered zones and defect clusters have different contributions to the image contrast (chapter 1) and therefore their observation can be—to a certain extent—made independently. Image contrast formation is very complex under weak-beam dark-field conditions, and in order to understand it, image simulations of an inclined disordered rod have been evaluated under chemical and fundamental reflections using CUFOUR (Appendix A). In the cases where high resolution is of primary importance it is very appropriate to form an image from the electrons which are scattered by a small fraction of the total number of atoms in the crystal. Such type of images might be obtained in dark-field using a portion of the diffracted pattern where the scattering of interest is dominant over the uninteresting signal from the surrounding crystal. For this purpose tilted illumination is used so that the scattered electron waves collected travel as close as possible to the optic axis. A significant number of experimental micrographs have been produced and analyzed in order to describe the microstructure of the above mentioned intermetallics (size distributions and densities). However, to reproduce and describe them all is not the purpose of the present chapter. A verbatim description is available as captions to Figures 4.1(a), 4.1(b), 4.1(c), 4.2(a), 4.2(b), 4.2(c), 4.3(a), 4.3(b), 4.3(c), 4.4(a), 4.4(b), 4.4(c), 4.4(d), 4.5(a), 4.5(b), 4.5(c), 4.5(d), 4.6(a), 4.6(b), 4.6(c), 4.7(a), 4.7(b), and 4.7(c). These micrographs are on the basis of the results presented in Figures 4.8, 4.9, 4.10, 4.11, 4.12, 4.13, 4.14, 4.15, 4.16, 4.17, and 4.18.
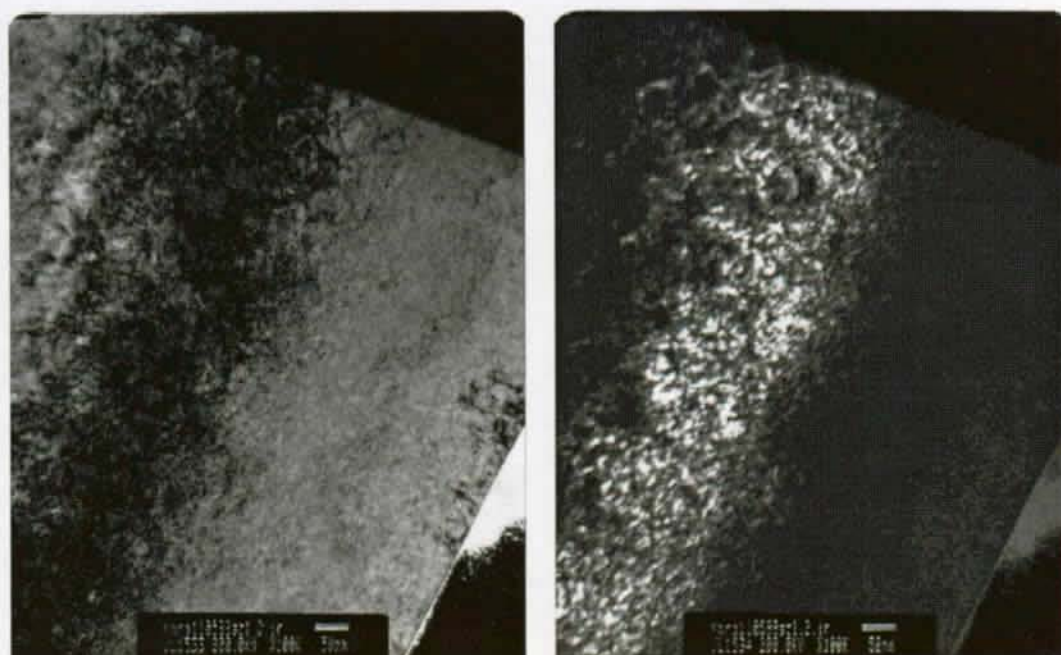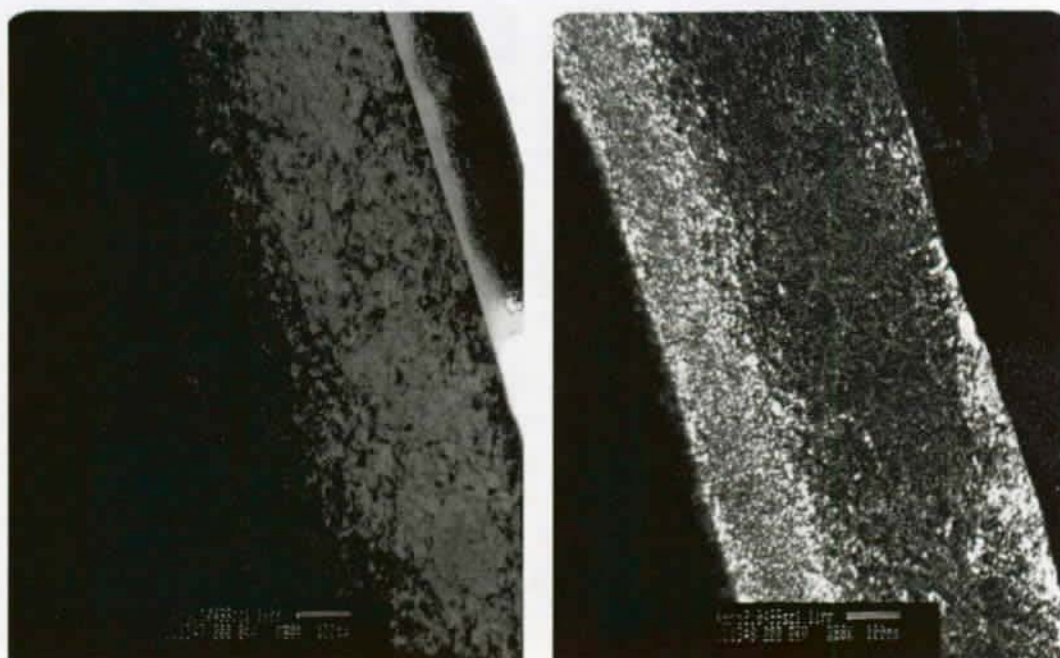
Figure 4.1: Microstructure of bulk NiAl irradiated with 700 keV single charged nickel ions at RT to 10^{14} cm^{-2} under (a) fundamental reflection, (b) chemical order reflection and (c) SAD.
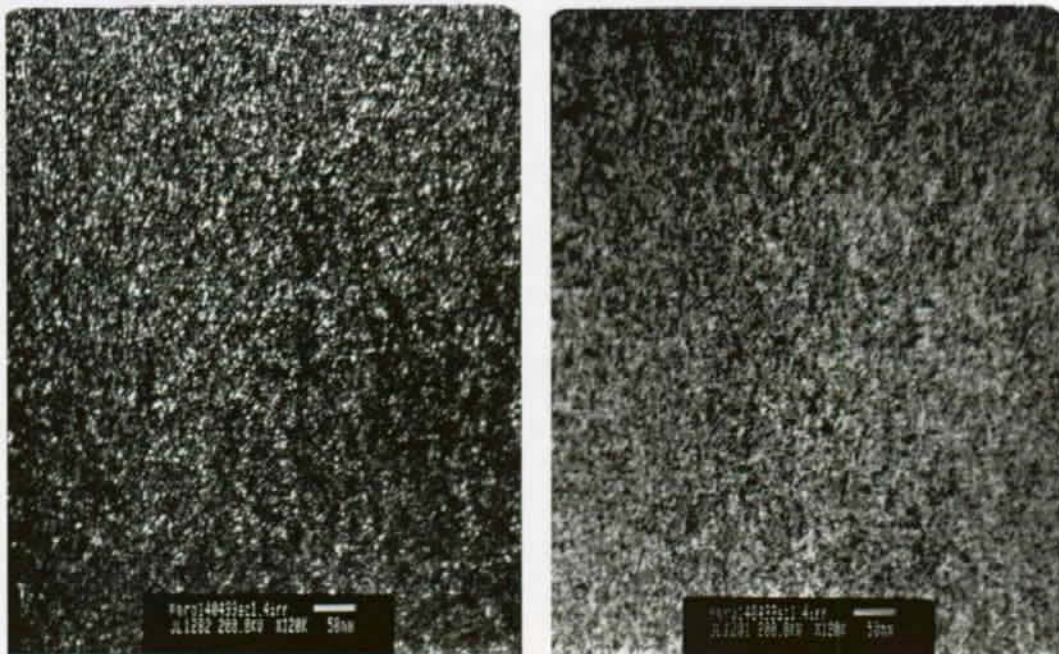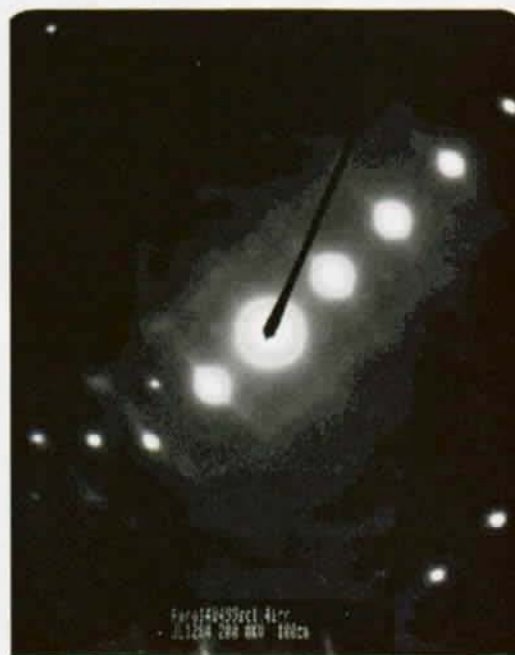
(a)

(b)

(c)

Figure 4.2: Microstructure of bulk NiAl irradiated with 700 keV single charged nickel ions at RT to 10^{15} cm^{-2} under (a) fundamental reflection, (b) chemical order reflection and (c) SAD.

(a)

(b)

(c)

Figure 4.3: Microstructure of bulk NiAl irradiated with 6 MeV double charged nickel ions at RT to 10^{14} cm^{-2} under (a) fundamental reflection, (b) chemical order reflection and (c) SAD.

(a)

(b)

(c)

(d)

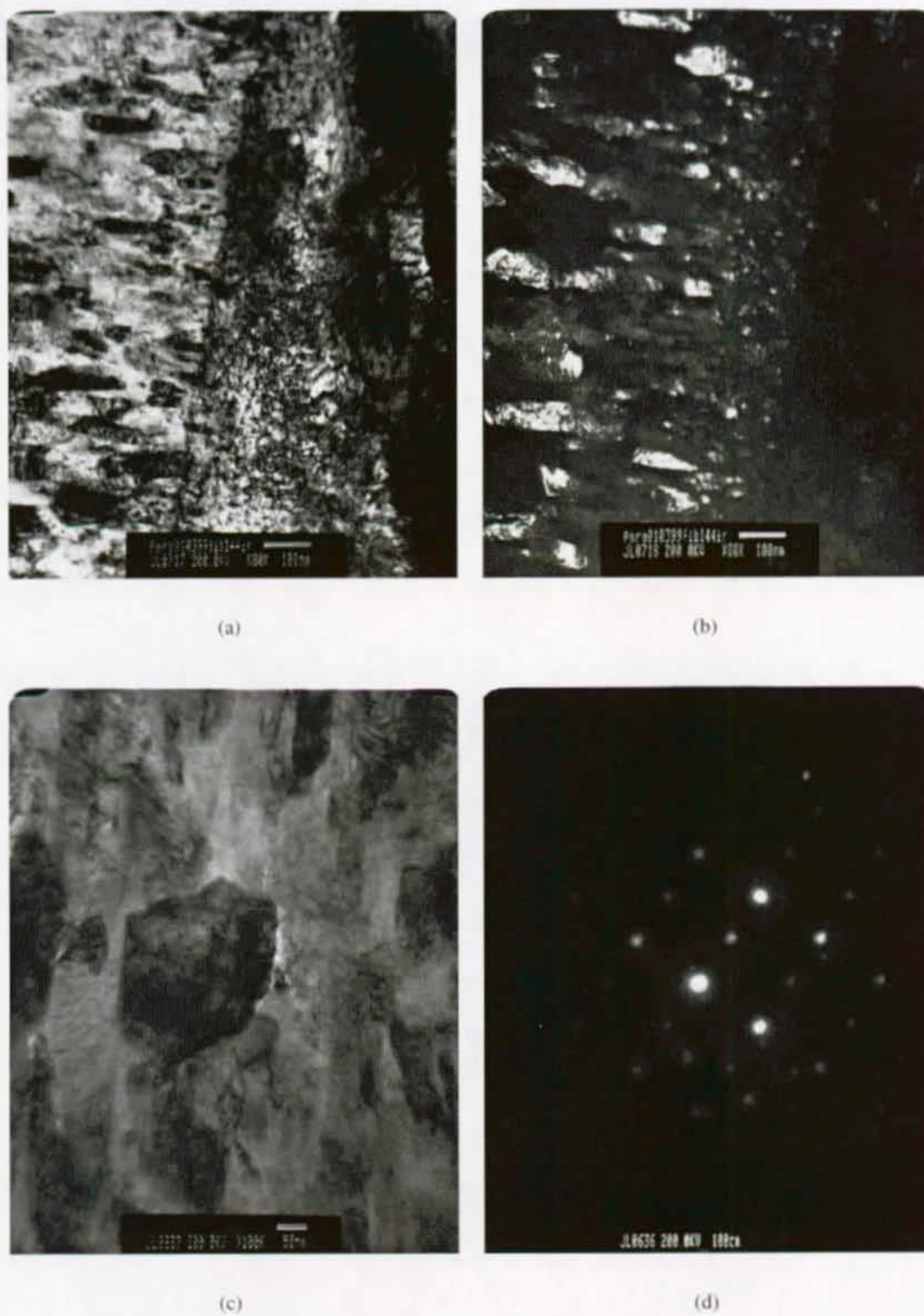Figure 4.4: Microstructure of layered NiAl irradiated with 6 MeV double charged nickel ions at liquid nitrogen temperature to 10^{15} cm^{-2} under (a) bright-field imaging, (b) dark-field imaging (c) bright-field detail imaging and (d) ND.
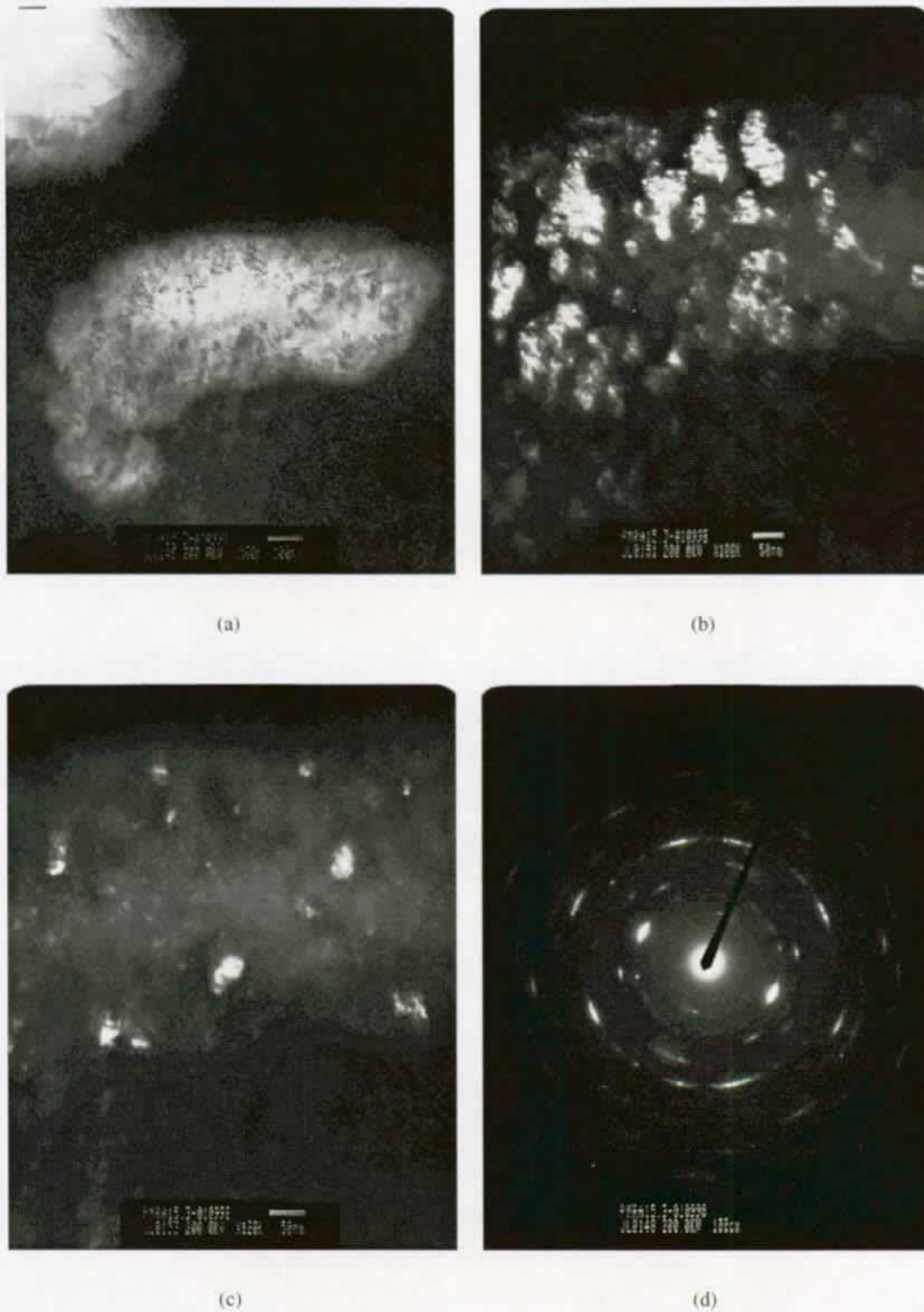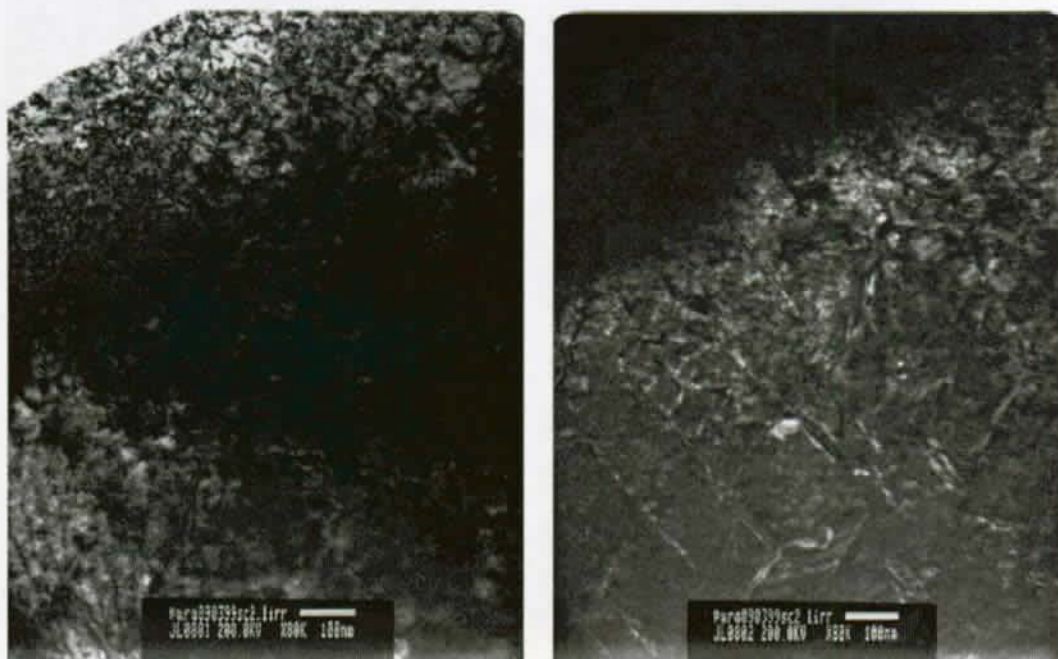
(a)

(b)

(c)

(d)

Figure 4.5: Microstructure of layered NiAl irradiated with 6 MeV double charged nickel ions at RT to 10^{14} cm^{-2} under (a) bright-field low magnification imaging, (b) fundamental reflection (c) chemical order reflection and (d) SAD.

(a)

(b)

(c)

Figure 4.6: Microstructure of bulk Ni$_3$Al irradiated with 700 keV single charged nickel ions at RT to 10^{15} cm^{-2} under (a) fundamental reflection, (b) chemical order reflection and (c) SAD.
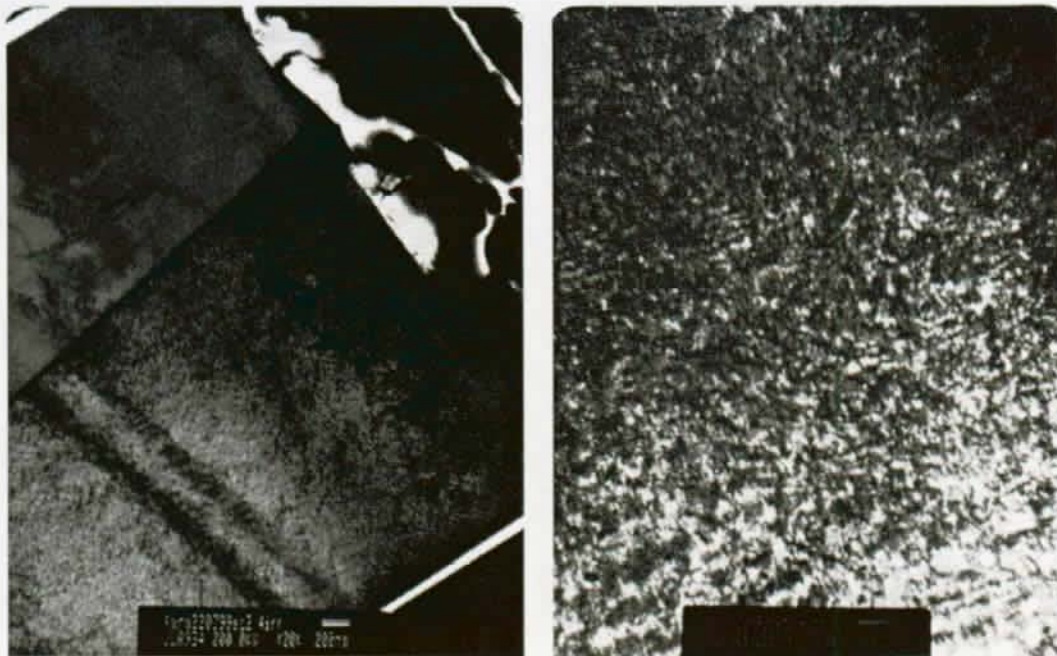
(a)

(b)

(c)
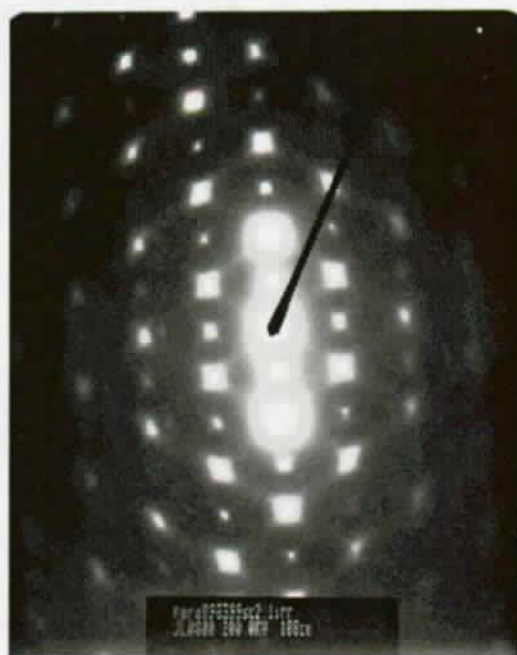
Figure 4.7: Microstructure of bulk Ni_3Al irradiated with 6 MeV double charged nickel ions at RT to 10^{14} cm^{-2} under (a) fundamental reflection, (b) chemical order reflection and (c) SAD.

4.1 CTEM characterization of induced disorder and defects

Crystalline solids exhibit long-range translational and orientational order. The irradiation-induced loss of both latter features is known as amorphization, which in fact represents a loss of topological order in the solid (Hobbs 1995). Under particle irradiation it is the displacement of atoms in the lattice which is responsible for the disordering transformation, being the displacive, rather than the ionizing radiation, which drives this process in the range of energies used in the present investigation. Topological order assessment is usually made under electron or x-ray diffraction.

Microstructural evolution under heavy-ion irradiation can be understood on the basis of the disordered zone to defect cluster densities ratio, ρ_d/ρ_c, in order to compare both intermetallics in a self-consistent approach due to different fluences (or doses), and primary ion energies. In the frame of Aronin's formulation (chapter 1), it is the long-range order parameter, described as a function of the fluence (or dose), that can be related to ρ_d as an estimator of the disordered fraction—and not the parameter ε—which is actually dependent on the primary ion recoil energy distributions, thus fully describing the mechanism. Therefore, and especially above the subcascade formation threshold, such a dimensionless analysis is better suited. Previous results have shown that below the subcascade formation threshold defect clusters outnumber those of disordered zones (Jenkins et al. 1976, Müller 1997). However, it appears that this ratio increases to a maximum value just before the breakdown of displacement cascades into subcascades. Therefore, at the subcascade regime, irradiation-induced disordering can be better described on the basis of the number of disordered zones (those which have not reordered)—afterwards the cascade collapse—and number of surviving defect clusters.

The overall results of the observations for NiAl are reported in Tables 4.1 and 4.2. They present a summary of the post-irradiated microstructure parameters (cluster mean size $\bar{x}_c$, disordered zone mean size $\bar{x}_d$, cluster density ρ_c, and disordered zone density ρ_d) which have been chosen to draw a consistent picture of the role of primary ion energy and fluence (or dose). A control group consisting of two layered samples (Table 4.2) has been prepared and these have been either irradiated at liquid nitrogen temperature or room temperature in order to investigate an eventual crystalline-to-amorphous transformation ($C \xrightarrow{a} A$) in polycrystalline microstructures.

The effect of increasing fluence on cluster mean size and density is evaluated for 700 keV primary nickel ions. At this regime the increase in fluence from 10^{14} to 10^{15} cm^{-2} results in an increase of cluster density from 7.0×10^{22} to 1.1×10^{23} m^{-3} (+57%) and an increase in cluster mean size from 2.5 to 3.5 nm (+40%). Being the former effect of straightforward understanding the latter nevertheless is indicative of

Table 4.1: NiAl irradiation matrix (room temperature).

E	Bulk				
	Φ [cm^{-2}]	$\bar{x}_c$ [nm]	$\bar{x}_d$ [nm]	ρ_c [m^{-3}]	ρ_d [m^{-3}]
700 keV	10^{15}	3.5		1.1×10^{23}	
	10^{14}	2.5	4.0	7.0×10^{22}	7.0×10^{22}
6 MeV	10^{14}	3.0	4.0	1.4×10^{23}	6.7×10^{22}

a non-saturated defect regime for clusters grow due to accumulation and not as the result of coalescence. The ratio of disordered zone density to cluster density, ρ_d/ρ_c, is approximately 1.0.

Increasing primary ion energy from 700 keV to 6 MeV and maintaining fluence constant at 10^{14} cm^{-2} results in an increase of cluster density from 7.0×10^{22} to 1.4×10^{23} m^{-3} (+100%) and an increase in cluster mean size from 2.5 to 3.0 nm (+20%). The increase in cluster density and cluster mean size is due to an overall increase in the total number of Frenkel pairs generated at the high-energy regime. The ratio of disordered zone density to cluster density, ρ_d/ρ_c, is approximately 0.5. This implies that at the high-energy regime a less effective disordering mechanism is active.

Table 4.2: Layered NiAl irradiation matrix: room temperature (high fluence) and liquid nitrogen (low fluence) cases.

E	Layered				
	Φ [cm^{-2}]	$\bar{x}_c$ [nm]	$\bar{x}_d$ [nm]	ρ_c [m^{-3}]	ρ_d [m^{-3}]
6 MeV	10^{15}		6.0–6.5		5.6×10^{21}
	10^{14}		5.0		1.2×10^{22}

The effect of decreasing the irradiation temperature from room temperature to liquid nitrogen has been studied for two layered samples (control group) irradiated with 6 MeV double charged nickel ions to 10^{15} cm^{-2}. Being the intermetallic layer thickness less than the projected range of the incoming ions—corresponding to the case of the sample irradiated at liquid nitrogen temperature—it might be shown that the actual dose in the observed region is comparable to a total fluence one decade below (Figure 2.15(b)), thus tabulated accordingly. A direct comparison among both layered samples indicate that an increase in temperature appears to be responsible for the recombination of a major fraction of defect clusters even though the fluence has been increased one decade.

At the high energy and low fluence regimes, an increase in disordered zone mean size from 4.0 to 5.0 nm (+25%) and a decrease in disordered zone density from 6.7×10^{22} to 1.2×10^{22} m^{-3} (-82%) has been registered. The increase in disordered zone mean size is thought to be due to a less efficient temperature-dependent reordering mechanism. As for the much reduced disordered zone density it might be explained

by the nanocrystalline microstructure which acts as an extra sink—which is thermally activated and more pronounced above stage II—for defect recombination at the grain boundaries. At this temperature regime a decrease in disordered zone density from 1.2×10^{22} to 5.6×10^{21} m^{-3} (-53%) has been registered, which means that a significant fraction of irradiation-induced disordered zones have reordered. Moreover, an increase in disordered zone mean size from 5.0 to 6.0–6.5 nm (+20–30%) has been observed. This trend, however, is not clear. Heavy-ion irradiation has been seen not to induce direct amorphization by the cascade in NiAl, contrary to the predicted behavior reported in the work of Spaczér (1995) based on MD results for there is no evidence of topological disorder under electron diffraction.

From a ballistic and structural point of view it is noteworthy to realize that defect accumulation in intermetallics and metals is different. Cluster density seems to scale less with dose than a pure bcc does despite its absolute value being higher and closer to that of a pure fcc (Victoria 2000). This suggests that a B2 intermetallic has a defect accumulation behavior other than a bcc material, most probably due to its chemical bond nature. Furthermore, it has been observed that at the high-energy regime higher cluster densities are measured for comparable doses.

The overall results of the observations for Ni$_3$Al are reported in Table 4.3. They present a summary of post-irradiated microstructure parameters (cluster mean size, disordered zone mean size, cluster density, and disordered zone density) which have been chosen to draw a complementary conclusion on the role of primary ion energy and fluence (or dose).

Table 4.3: Ni$_3$Al irradiation matrix (room temperature).

E	Bulk				
	Φ [cm^{-2}]	$\bar{x}_c$ [nm]	$\bar{x}_d$ [nm]	ρ_c [m^{-3}]	ρ_d [m^{-3}]
700 keV	10^{15}	3.5	4.0–4.5	1.0×10^{23}	4.5×10^{22}
6 MeV	10^{14}	2.5	4.5	1.5×10^{23}	2.2×10^{22}

Room temperature irradiations with 700 keV single charged and 6 MeV double charged nickel ions to 10^{15} and 10^{14} cm^{-2}, respectively, have been performed and studied. At the low energy and high fluence regime a cluster mean size of 3.5 nm and a disordered zone mean size of 4.0–4.5 nm have been measured. At this regime a cluster density of 1.0×10^{23} and a disordered zone density of 4.5×10^{22} m^{-3} have been estimated. The ratio of disordered zone density to cluster density, ρ_d/ρ_c, is approximately 0.5. At the high-energy and low fluence regime a cluster mean size of 2.5 nm and a disordered zone mean size of 4.5 nm have been measured. At this regime a cluster density of 1.5×10^{23} and a disordered zone density of 2.2×10^{22} m^{-3} have been estimated. The ratio of disordered zone density to cluster density, ρ_d/ρ_c, is approximately 0.2. It is therefore clear that at the high-energy regime a less efficient

disordering mechanism is active as compared to the low energy regime. This result is supported and will be further discussed on p. 112. Cluster density seems to scale less with dose than a typical pure fcc does (Victoria 2000). This suggests that a $L1_2$ intermetallic has a defect accumulation behavior other than the majority of the fcc materials, most probably due to its chemical bond nature, but comparable to the case of nickel.

From a structural view point it is indeed interesting to compare the two intermetallics under heavy-ion irradiation. Being the ratio of disordered zone density to cluster density, ρ_d/ρ_c, an estimator of irradiation-induced disordering efficiency, it is now arguable that for a predominant electronic stopping regime this ratio decreases with primary ion energy (Figure 4.19). Moreover, the ratio being higher in NiAl than in Ni_3Al for equivalent irradiation conditions means that a larger fraction of disordered zones did not reorder and therefore a lower long-range order value might be inferred. In so doing, and within the framework of Bragg and Williams (section 1.2), it directly implies that the redistribution of atomic species from the most densely populated sublattice into the less populated one do control the disordering mechanism. In NiAl, the disordering mechanism is most probably symmetric due to its two equivalent sublattices.

Estimated values for cluster and disordered zone mean sizes in both intermetallics under irradiation have been compiled after the work of Müller (1997) and further completed with data corresponding to higher energies as previously described (Table 4.4). As the recoil energy increases above the subcascade formation threshold the cascade breaks down and therefore it is mandatory to understand that at higher energies the displacement cross-section is significantly reduced as compared to the low energy regime values. Furthermore, due to this subcascade forming mechanism, the increase in cascade size is no longer verified. In spite of this mechanism, the application of a phenomenological power law (Müller 1997) describing the dependency of the disordered zone (or cluster) mean size and the displacement cross-section has been used as a quantification procedure as follows:

$$\bar{x}_{c,d} = k_2 \sigma_d^{1/\alpha_w} \tag{4.1}$$

where $\bar{x}_{c,d}$ is the cluster or disordered zone mean size, k_2 is a pre-exponential factor dependent on the primary ion energy and material, σ_d is the displacement cross-section, and α_w is a phenomenological exponential factor.

Using the above mentioned power law the cluster or disordered zone mean size has been plotted as func-

tion of the displacement cross-section (Figure 4.20) and a numerical fit has been evaluated yielding a correlation square of 86%, a pre-exponential factor $k_2 = 2.4$, and an exponential factor $\alpha_w = 2.2$, in agreement with the published value, $\alpha_w = 2.5$, reported by Müller (1997). However, if the dependency of the cluster or disordered zone mean size is described as a function of the primary ion energy instead of the displacement cross-section, a relation of type $\bar{x}_{c,d} = k_1 E^{1/\alpha_e}$, where k_1 is a pre-exponential factor, E is the primary ion energy, and α_e is a phenomenological exponential factor, a secondary type of irradiation regime arises due to subcascade formation—the displacement cross-section decreases significantly— whereby the cascade size is no longer increasing with energy. It appears, nevertheless, that the phenomenological power law described in equation 4.1 is valid even in the case of subcascade formation. Figure 4.20 might in fact be interpreted as a two-region plot; at the low displacement cross-section region which corresponds to a high-energy regime it seems that the disordered zone or cluster mean size is constant and that at the high displacement cross-section end the object size scales according to a power law as in equation 4.1. This suggests that even though the whole process can be modeled as a single mechanism (either at the subcascade regime or not) it can be divided, eventually, in two distinct mechanisms. Due to the relatively small differences in the displacement cross-sections used during the present experiments this uncertainty remains.
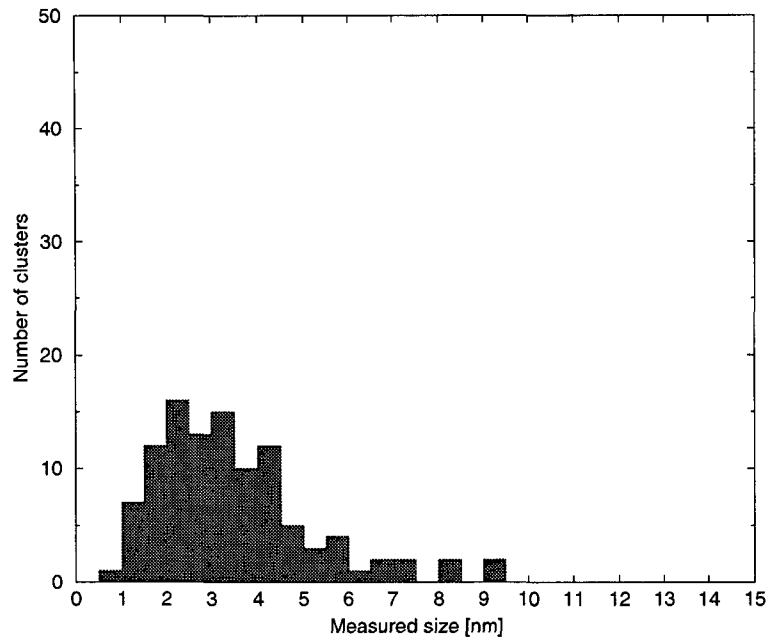
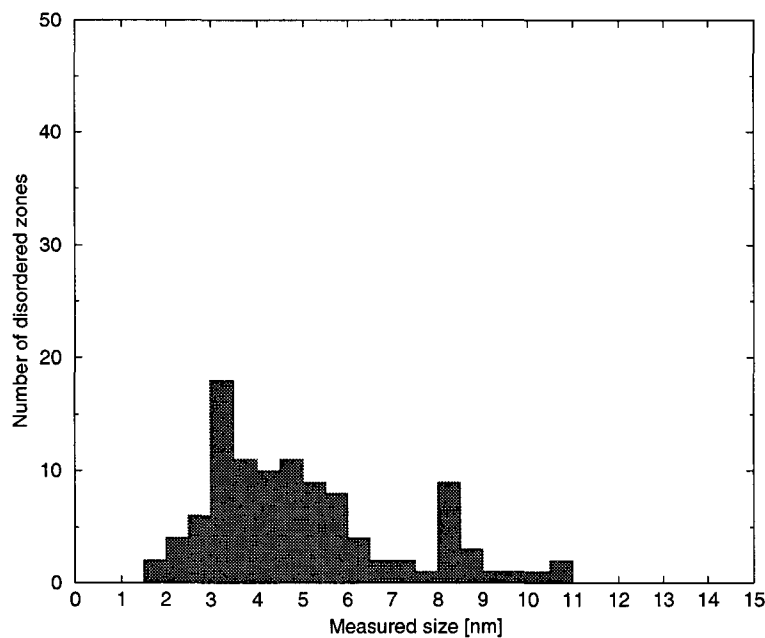Figure 4.8: Cluster size distribution for bulk NiAl irradiated with 700 keV single charged nickel ions at RT to 10^{14} cm^{-2}. Cluster mean size, $\bar{x}_c = 2.5$ nm; Number of sampled defects, $N_d = 107$; Volume sampled, $V_s = 104$ nm $\times$ 104 nm $\times$ 140 nm ($S \times t$); Cluster density, $\rho_c = 7.0 \times 10^{22}$ m^{-3}.

Figure 4.9: Disordered zone size distribution for bulk NiAl irradiated with 700 keV single charged nickel ions at RT to 10^{14} cm^{-2}. Disordered zone mean size, $\bar{x}_d = 4.0$ nm; Number of sampled zones, $N_z = 107$; Volume sampled, $V_s = 104$ nm $\times$ 104 nm $\times$ 140 nm ($S \times t$); Disordered zone density, $\rho_d = 7.0 \times 10^{22}$ m^{-3}.
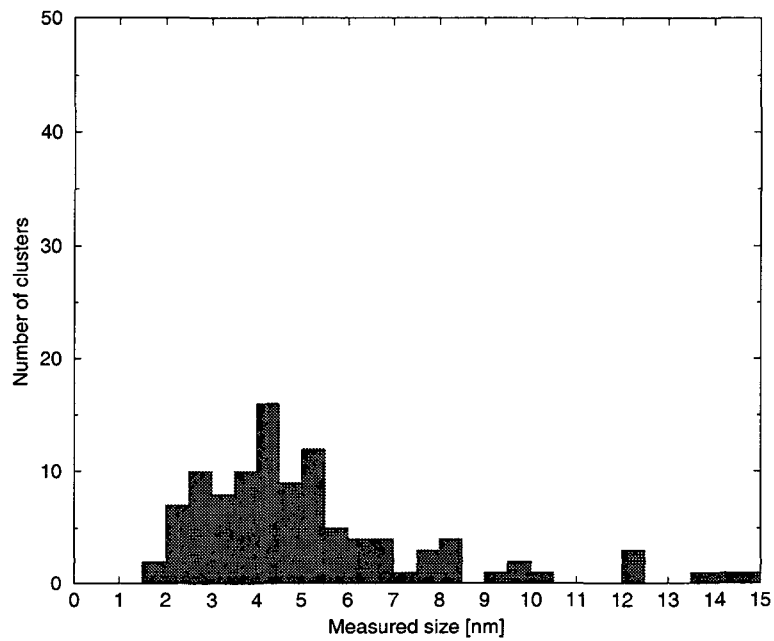
Figure 4.10: Cluster size distribution for bulk NiAl irradiated with 700 keV single charged nickel ions at RT to 10^{15} cm^{-2}. Cluster mean size, $\bar{x}_c = 3.5$ nm; Number of sampled defects, $N_d = 105$; Volume sampled, $V_s = 100$ nm $\times$ 100 nm $\times$ 100 nm ($S \times t$); Cluster density, $\rho_c = 1.1 \times 10^{23}$ m^{-3}.
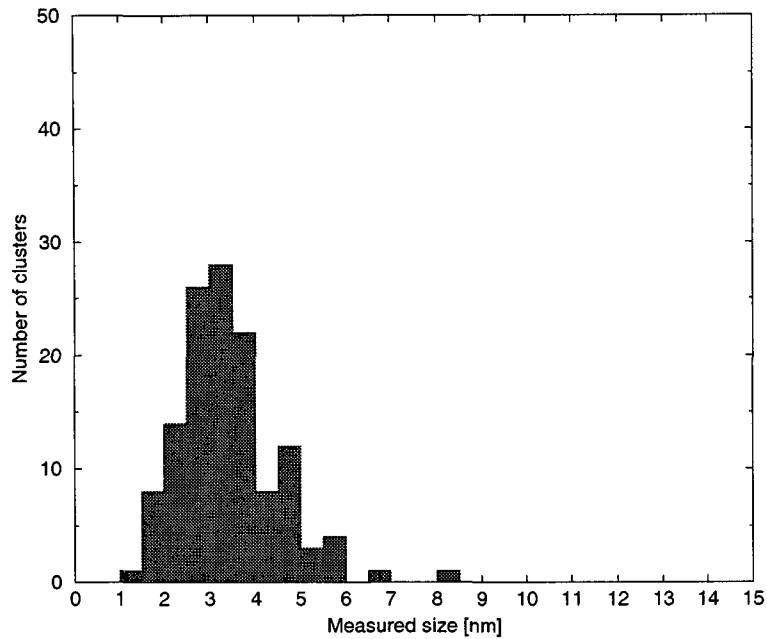
Figure 4.11: Cluster size distribution for bulk NiAl irradiated with 6 MeV double charged nickel ions at RT to 10^{14} cm^{-2}. Cluster mean size, $\bar{x}_c = 3.0$ nm; Number of sampled defects, $N_d = 128$; Volume sampled, $V_s = 100$ nm $\times$ 100 nm $\times$ 90 nm $(S \times t)$; Cluster density, $\rho_c = 1.4 \times 10^{23}$ m^{-3}.

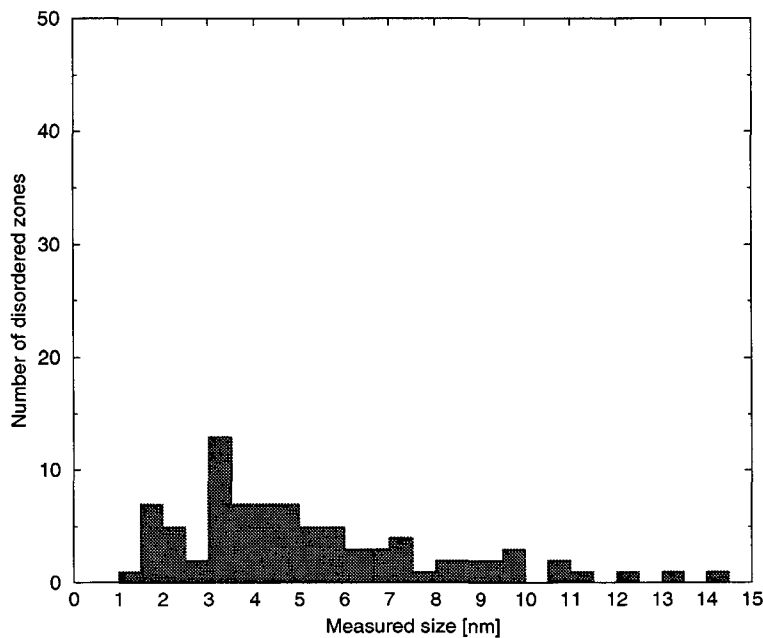Figure 4.12: Disordered zone size distribution for bulk NiAl irradiated with 6 MeV double charged nickel ions at RT to 10^{14} cm^{-2}. Disordered zone mean size, $\bar{x}_d = 4.0$ nm; Number of sampled zones, $N_z = 87$; Volume sampled, $V_s = 120$ nm $\times$ 120 nm $\times$ 90 nm $(S \times t)$; Disordered zone density, $\rho_d = 6.7 \times 10^{22}$ m^{-3}.
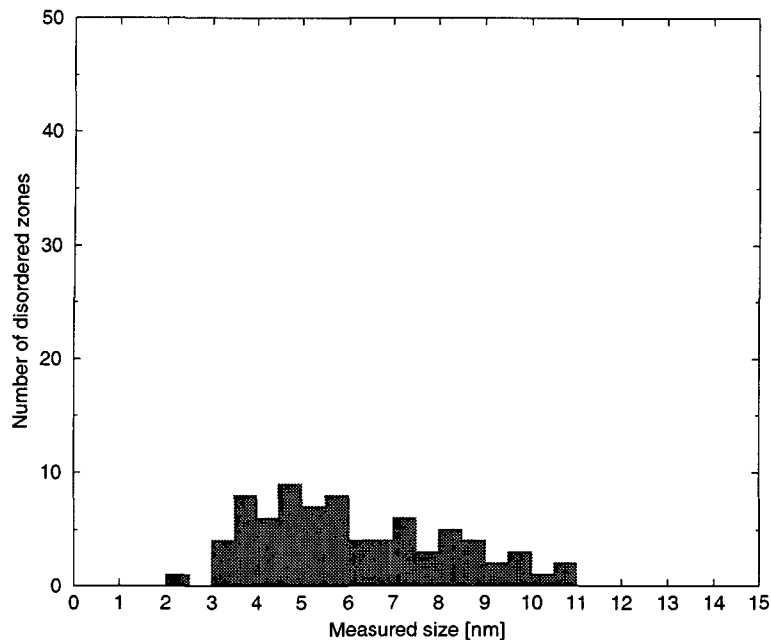
Figure 4.13: Disordered zone size distribution for layered NiAl irradiated with 6 MeV double charged nickel ions at liquid nitrogen temperature to 10^{15} cm^{-2}. Disordered zone mean size, $\bar{x}_d = 5.0$ nm; Number of sampled zones, $N_z = 78$; Volume sampled, $V_s = 250$ nm $\times$ 250 nm $\times$ 100 nm $(S \times t)$; Disordered zone density, $\rho_d = 1.2 \times 10^{22}$ m^{-3}.
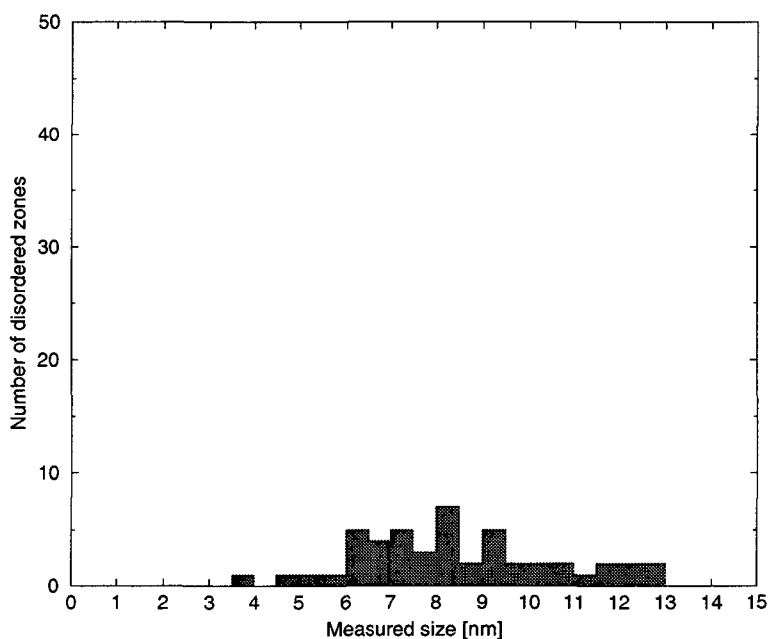

Figure 4.14: Disordered zone size distribution for layered NiAl irradiated with 6 MeV double charged nickel ions at room temperature to 10^{15} cm^{-2}. Disordered zone mean size, $\bar{x}_d = 6.0$–6.5 nm; Number of sampled zones, $N_z = 48$; Volume sampled, $V_s = 250$ nm $\times$ 250 nm $\times$ 140 nm $(S \times t)$; Disordered zone density, $\rho_d = 5.6 \times 10^{21}$ m^{-3}.
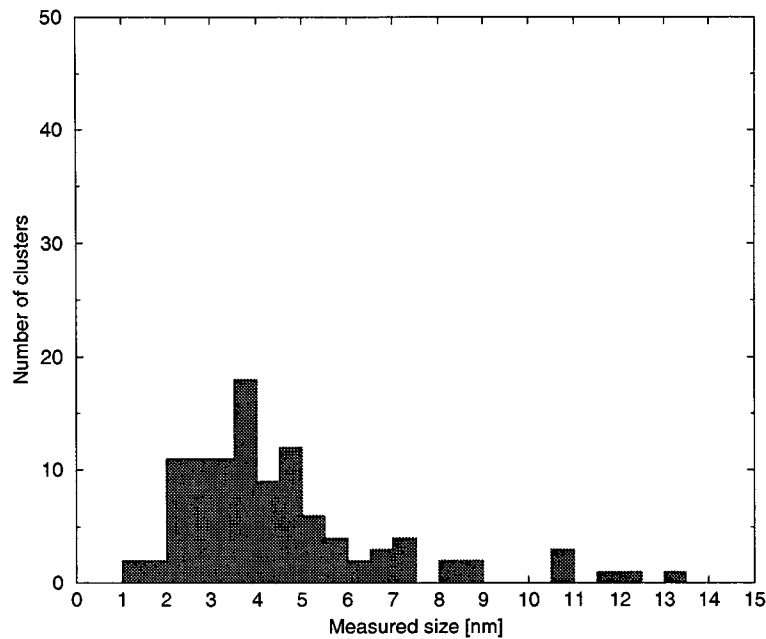
Figure 4.15: Cluster size distribution for bulk Ni_3Al irradiated with 700 keV single charged nickel ions at RT to 10^{15} cm^{-2}. Cluster mean size, $\bar{x}_c = 3.5$ nm; Number of sampled defects, $N_d = 112$; Volume sampled, $V_s = 100$ nm $\times$ 100 nm $\times$ 112 nm ($S \times t$); Cluster density, $\rho_c = 1.0 \times 10^{23}$ m^{-3}.

Figure 4.16: Disordered zone size distribution for bulk Ni_3Al irradiated with 700 keV single charged nickel ions at RT to 10^{15} cm^{-2}. Disordered zone mean size, $\bar{x}_d = 4.0$–4.5 nm; Number of sampled zones, $N_z = 50$; Volume sampled, $V_s = 100$ nm $\times$ 100 nm $\times$ 112 nm ($S \times t$); Disordered zone density, $\rho_d = 4.5 \times 10^{22}$ m^{-3}.

Figure 4.17: Cluster size distribution for bulk Ni_3Al irradiated with 6 MeV double charged nickel ions at RT to 10^{14} cm^{-2}. Cluster mean size, $\bar{x}_c = 2.5$ nm; Number of sampled defects, $N_d = 132$; Volume sampled, $V_s = 100$ nm $\times$ 100 nm $\times$ 90 nm $(S \times t)$; Cluster density, $\rho_c = 1.5 \times 10^{23}$ m^{-3}.
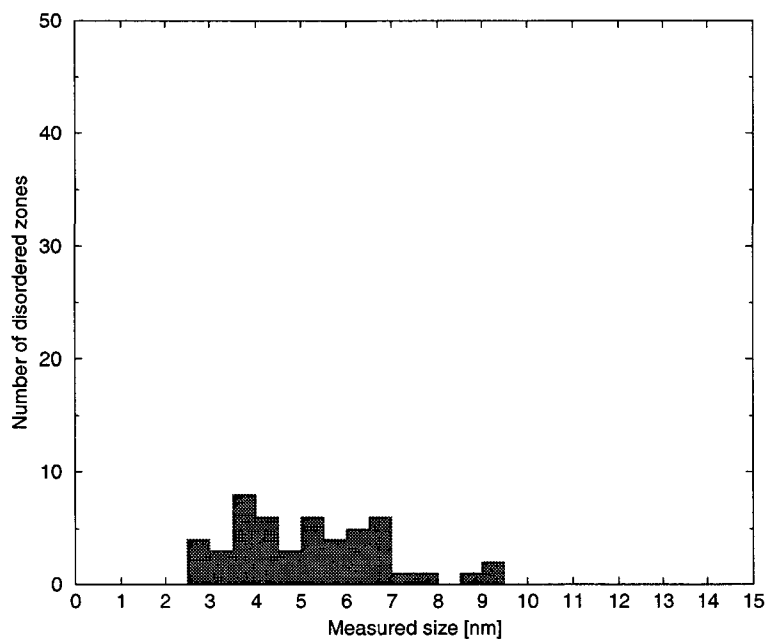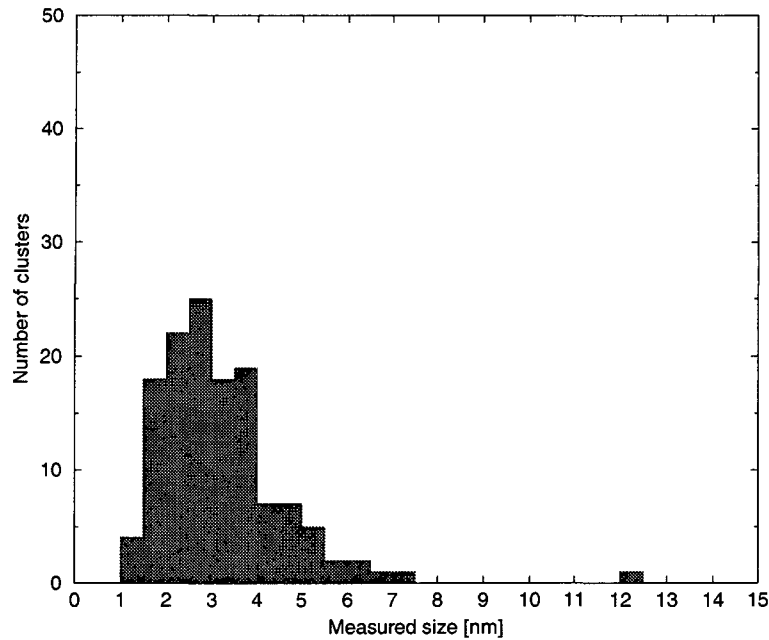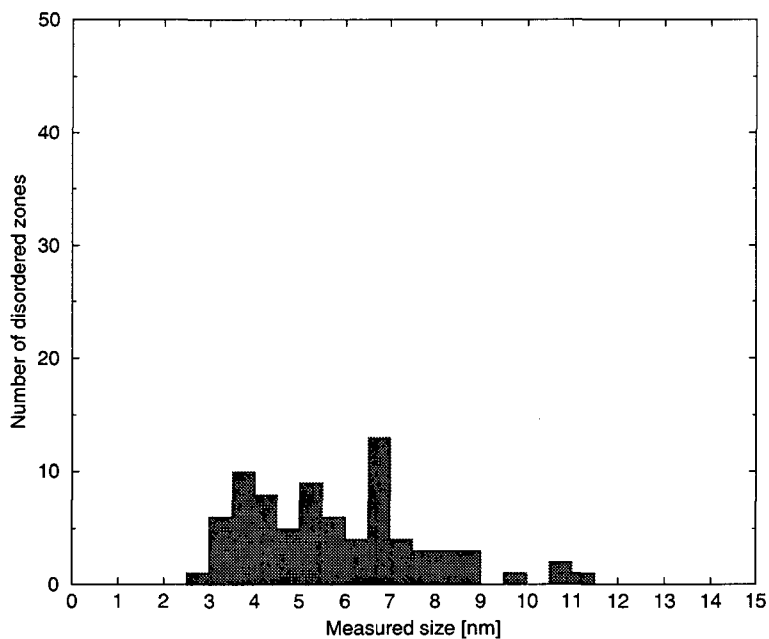

Figure 4.18: Disordered zone size distribution for bulk Ni_3Al irradiated with 6 MeV double charged nickel ions at RT to 10^{14} cm^{-2}. Disordered zone mean size, $\bar{x}_d = 4.5$ nm; Number of sampled zones, $N_z = 79$; Volume sampled, $V_s = 200$ nm $\times$ 200 nm $\times$ 90 nm $(S \times t)$; Disordered zone density, $\rho_d = 2.2 \times 10^{22}$ m^{-3}.
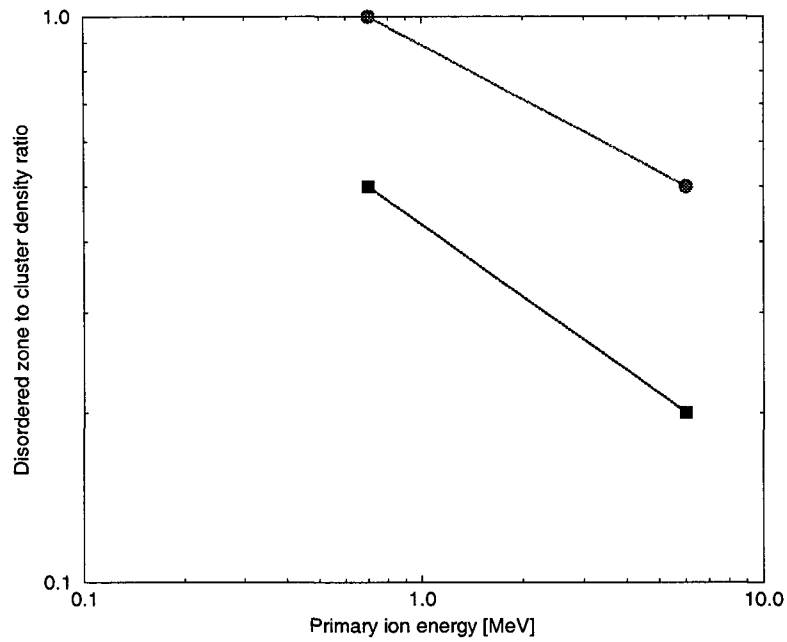
Figure 4.19: Disordered zone to cluster density ratio for irradiated NiAl (top) and Ni₃Al (down) as function of the primary ion energy.

Table 4.4: Cluster and disordered zone mean size as function of irradiation properties.

Mater.	Ion	E [keV]	σ_d [m²]	$\bar{x}_c$ [nm]	$\bar{x}_d$ [nm]
NiAl	Ni^+	700	1.48×10^{-19}	2.5	4.0
	Ni^{+2}	6000	9.52×10^{-20}	3.0	4.0
Ni₃Al	Ta^+	30	4.00×10^{-19}		6.3
	Ta^+	50	4.70×10^{-19}		7.6
	Ta^+	300	6.70×10^{-19}		12.6
	Ni^+	300	2.50×10^{-19}		2.4
	Ni^+	700	1.54×10^{-19}	3.5	4.0–4.5
	Ni^{+2}	6000	1.03×10^{-19}	2.5	4.5
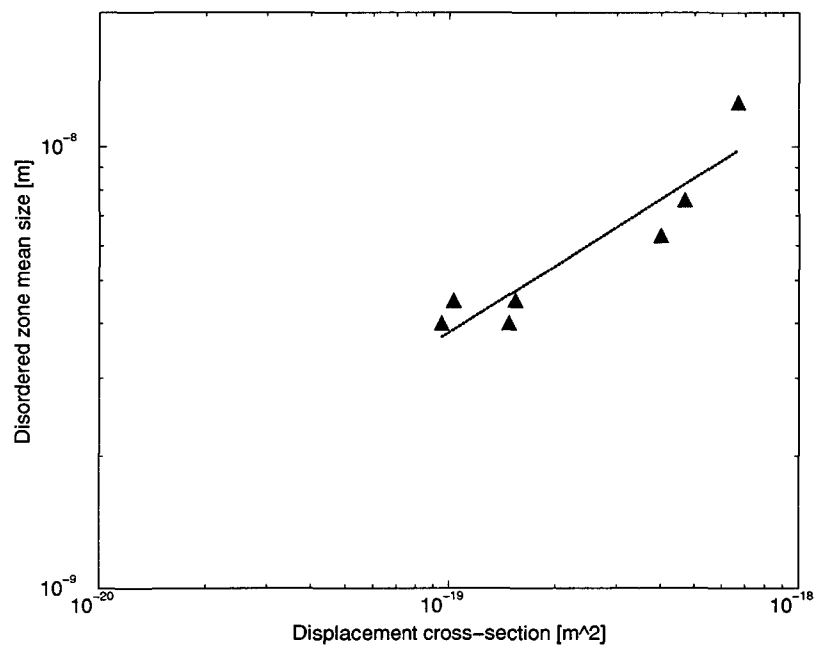
Figure 4.20: Disordered zone mean size as function of the displacement cross-section in nickel-aluminium intermetallics.

4.2 Summary

A comparative study on the behavior of NiAl and Ni_3Al under heavy-ion irradiation has shown that in fact these intermetallics are rather similar regarding disordered zone and defect cluster mean sizes. However, it must be noted that although such similarity exists, their distinct disordering mechanisms are evidenced through the differences in disordered zone and defect cluster densities measured. This behavior is mostly understood in the frame of the order-disorder theory of Bragg & Williams (1934), which is based on a concept arising from the sitting probability distributions associated with the (constrained) rearrangement of the atomic species into the crystalline structure.

Despite the success of this theory in quantifying long-range order, it does not take into account the possibility of describing non-lattice site structural defect formation. Therefore, topological information concerning the irradiated intermetallic should be assessed from long-range order and defect cluster density measurements.

Chapter 5

Discussion and Conclusions

The truth is more important than the facts.

— Frank Lloyd Wright

A comparative study on the behavior of NiAl and Ni$_3$Al under heavy-ion irradiation has been conducted as follows:

- Study of the microstructure and growth modes of stoichiometric NiAl and Ni$_3$Al thin films deposited by r.f.-magnetron co-sputtering as proper irradiation media in order to quantify the ion-mixing at high primary ion energies and evaluate an eventual crystalline-to-amorphous transformation (directly induced by the cascade);

- A numerical link between previous molecular dynamics results and transmission electron microscopy image simulation, thus establishing under cascade damage conditions which type of defects are created and how do the above mentioned intermetallics compare regarding the effect of primary ion energy and damage accumulation (cascade overlap);

and

- a microstructural investigation using transmission electron microscopy of heavy-ion irradiated NiAl and Ni$_3$Al samples in order to establish a set of physical parameters (defect visibility, disordered zone and defect densities, and respective mean sizes) to be directly compared in a self-consistent approach to the results obtained through image simulation of damaged intermetallics.

99

In contrast to earlier experiments (Van Swygenhoven et al. 1994), the present results show that the intermetallic thin films deposited onto silicon (100) are polycrystalline with chemically ordered individual grains a few nanometers in typical size. Despite the small grain size, electron ND techniques allow to identify the superlattice reflection spots due to an ordered arrangement of the atomic sublattices. The strong lattice mismatch between the silicon substrate and the intermetallic thin films excludes the possibility of an epitaxial structure. Nevertheless, a specific two-dimensional texture develops as a result of interfacial energy minimization between the substrate and the deposit in the early stages of nucleation (Szpunar 1997), and because a crystal tends to expose surfaces having low Miller indices. These minimum stress surfaces correspond to the $\{110\}$ lattice planes in a bcc structure and to the $\{111\}$ planes in a fcc. They tend to orient parallel with the substrate plane during the growth. As observed with SAD, NiAl crystallizes in a bcc structure and Ni_3Al in a fcc. As expected, the preferential growth directions are the $\langle 110 \rangle$ and the $\langle 111 \rangle$, respectively. A three-dimensional island growth following the Volmer-Weber (VW) mode (Smith 1995) induces a columnar structure ($d/t < 1$, where d and t are the characteristic linear dimensions of a non-equiaxed crystallite (Hentzel et al. 1984, Thompson 1990)) giving rise to a fiber textured layer. This mechanism of nucleation is typically found during the growth of metals onto non-metallic substrates (Cahn et al. 1993).

In an energy-enhanced deposition process like sputtering the impinging species reaches the substrate with kinetic energies of the order of 1000 kJ/mol, higher than the chemical reaction energy (Du & Clavaguera 1996, Huang & Chang 1998), and are therefore adsorbed into the chemisorbed state (Eley-Rideal mechanism). Both aluminium and nickel have sputtering yields of the same order of magnitude (Smith 1995). This condition imposes an almost immediate steady state of atomic concentration in the deposit. As neither aluminium nor nickel have high atomic solubility into silicon at the substrate temperatures used, an abrupt interface forms between the substrate and the film, as it is indeed confirmed by SIMS and cross-sectional TEM observations. The substrate temperature can be kept high enough thus increasing the grain size of the thin film and enhancing structural order of the deposit through the mobility of the adatoms. Consequently, the polycrystalline intermetallic thin films are deposited with compositions close to the stoichiometric, being chemically ordered, textured, and showing great surface smoothness of the order of the nanometer.

The investigation of the microstructure and orientation of intermetallic nickel-aluminium thin films deposited onto nickel (110) shows that:

- NiAl exhibits an inverse Nishiyama-Wassermann (NW) granular-heteroepitaxial relationship of type $(\bar{2}11)[\bar{2}11]_{B2} \parallel (\bar{1}10)[\bar{1}10]_{fcc}$, although this growth mode is mixed with a distribution of poly-

crystalline grains of small sizes. This mechanism can be understood as a dynamic balance between the surface energies γ_s, γ_f and γ_{in}, which stand for the substrate surface energy, the surface energy for a monolayer and the interface energy, respectively. Monolayer-by-monolayer growth occurs only in the Frank-van der Merwe (FvdM) mode (Smith 1995) which is induced when $\Delta\gamma_n = \gamma_{fn} + \gamma_{in} - \gamma_s \leq 0$ for all n monolayers (thickness independent). This condition is fulfilled only in the case of homoepitaxy but can be partially satisfied in the heteroepitaxial case ($\gamma_s \neq \gamma_f$) until a given n-th monolayer. Beyond this point the growth switches to the Stranski-Krastanov (SK) mode (Smith 1995) through the formation of three-dimensional crystals. The FvdM mode is achieved from the first monolayer, $\gamma_s = 2.364$ J/m^2 (Bauer & van der Merwe 1986), $\gamma_f = 1.4$ J/m^2 (Miracle 1993), $\gamma_{in} \approx 0.746$ J/m^2 (Miracle 1993) and $\gamma_f + \gamma_{in} - \gamma_s = -0.218$ J/m^2. This layer-by-layer growth mode continues until the balance of the surface energies is no longer verified due to accumulation of strain energy (the lattice mismatch is 5.3%) leading to an increase of the interface energy. Assuming the rigidity modulus to scale with $\sqrt{n}$ this corresponds to a transition from FvdM to SK after the third monolayer. The energy mismatch, $\Gamma_{sf} = 2|(\gamma_s - \gamma_f)/(\gamma_s + \gamma_f)|$, is equal to 0.51. The ratio of the nearest-neighbor distances is 0.8202, which is in the range of values in order to eventually grow a layer in a NW orientation relationship with the substrate (van der Merwe 1982, Bauer & van der Merwe 1986, Hellwig et al. 1998);

and

- Ni$_3$Al forms a single-crystalline layer and exhibits a simple heteroepitaxial relationship of type $(\bar{1}10)[\bar{1}10]_{L1_2} \| (\bar{1}10)[\bar{1}10]_{fcc}$. The nucleation mode is induced by a positive surface energy balance, $\Delta\gamma = \gamma_f + \gamma_{in} - \gamma_s > 0$, where $\gamma_f \approx 2.08$ J/m^2 (Du & Clavaguera 1996, Huang & Chang 1998) is the thin film surface energy for a monolayer, $\gamma_{in} \approx 1.2$ J/m^2 (Lu & Kioussis 1997) is the interface energy and $\gamma_s = 2.364$ J/m^2 (Bauer & van der Merwe 1986) is the substrate surface energy. A three-dimensional epitaxial island growth corresponding to a VW mode is achieved during the deposition process. The surface energy mismatch, Γ_{sf}, is equal to 0.13. The critical value defined for the formation of a superlattice structure is $\Gamma_{sf} \leq 0.5$ (Bauer & van der Merwe 1986). Therefore, the growth of a superlattice structure is energetically favored.

A microstructure diagram has been established relating the deposition rate and substrate temperature of both intermetallics onto silicon (100) and nickel (110) to their thin film growth orientation (Figure 5.1). The diagram shows, at deposition rates between 0.1 and 0.2 nm/s and substrate temperature below 300 K, the formation of polycrystalline intermetallic films onto silicon, whereas at low deposition rate and in a

range of temperatures between 300 and 750 K a fiber texture develops. When the intermetallics are deposited onto nickel (110) single-crystals, a granular- and a heteroepitaxial mode of growth is evidenced.
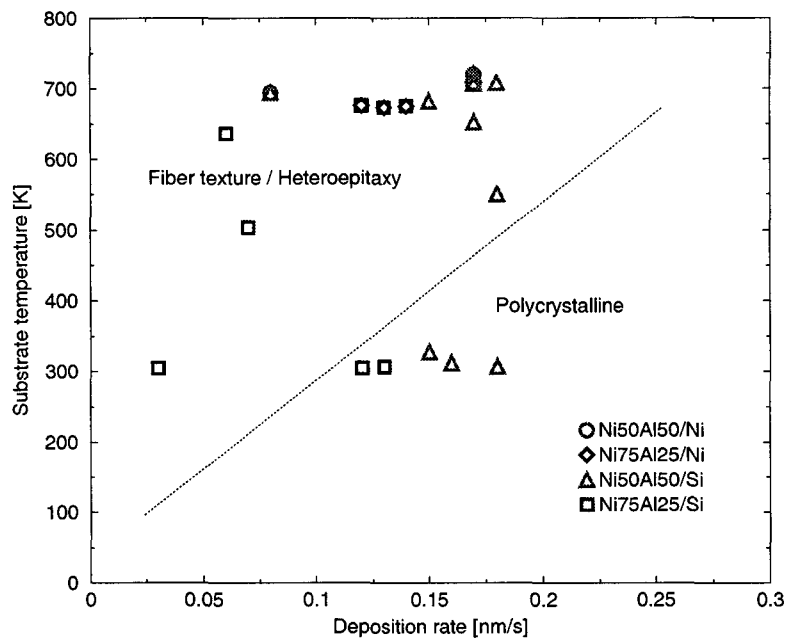

Figure 5.1: Thin film orientation as function of deposition rate and substrate temperature.

The present results contribute to the systematic studies of the influence of the deposition parameters during the condensation of metallic elements onto semiconductors and metallic substrates and their influence on the thin film orientation. They demonstrate the inverse NW relationship for NiAl grown onto nickel (110) and the heteroepitaxy of Ni_3Al. Furthermore, they show that the observed orientation relations depend on the lattice parameter misfits, which are relatively small for the intermetallics onto nickel and therefore prompting a heteroepitaxial mode of growth. The nearest-neighbor distances ratio for NiAl onto nickel is close to the optimal values defined for the NW orientation relation of a bcc deposit onto a fcc substrate. This appears to be an indicator to predict the epitaxial growth of bcc-type intermetallic superlattices onto metallic substrates.

Inherent to the deposition technique, and at the low substrate temperature regime, is the formation of defect structures and polycrystalline materials which are not the most convenient for post-irradiation microstructure assessment. Therefore, special attention has been given to bulk single-crystals which have been irradiated and prepared in cross-section for transmission electron microscopy (TEM) observations.

Molecular dynamics simulations have been previously performed in order to understand irradiation-induced disordering and defect formation at high primary ion energies in ordered nickel-aluminium intermetallics and its elements (Spaczér et al. 1994a, Spaczér et al. 1994b, Spaczér, Caro, Victoria

& de la Rubia 1995, Spaczér, Caro & Victoria 1995, Spaczér 1995, Spaczér et al. 1997, Almazouzi et al. 1998, Almazouzi 1999, Almazouzi et al. 1999). The majority of these simulation studies have used recoil energies in the range 10–30 keV. The choice of a representative recoil energy within these values is validated on the basis of the statistical distribution of the recoil spectra these reactions have.

A series of Monte Carlo simulations using TRIM have been calculated yielding the recoil distributions as functions of ion penetration (depth), which have been further processed in order to evaluate the probability of occurrence for a specific recoil event. These recoil energy distributions, being representative of the irradiations performed in this work, are plotted in Figures 5.2(a), 5.2(b), 5.3(a), 5.3(b), 5.4(a), 5.4(b), 5.5(a), and 5.5(b). The mean recoil energies are reported in Table 5.1.

Table 5.1: Mean recoil energies.

| Mater.	$\bar{E}_{PKA}$ [keV]	
	700 keV-nickel	6 MeV-nickel
NiAl	4.2	12.2
Ni$_3$Al	4.4	12.8

It should be noted, however, that 100% of the recoil events are below 10 keV for irradiations with 700 keV-nickel primary ions (Figures 5.2(b) and 5.3(b)). Therefore, the choice of a recoil energy of 10 keV used in molecular dynamics computer simulations appears to be representative, although over-estimated in comparison to the mean recoil. For irradiations with 6 MeV-nickel primary ions, the corresponding choice of a 10 or 15 keV recoil is subject to further assessment for only 40% of the total number of events has an energy below 15 keV (Figures 5.4(b) and 5.5(b)). Despite of the representativity these numbers might have, it must be understood that molecular dynamics simulation results are not numerous enough to draw reasonable conclusions on the basis of statistical evidence. They are valid and valuable, though, in estimating the maximum disordered zone and defect cluster sizes and their respective numbers.

Molecular dynamics predict the microstructure evolution under a variety of simulation conditions at 0 K. Under nickel-ion irradiation these results have supported the existence of a highly disordered core in both NiAl and Ni$_3$Al (pair distribution function analysis). Equivalent simulation conditions show that NiAl evolves faster to a highly disordered state, eventually becoming amorphous at high recoil energy (15 keV), which does not happen in Ni$_3$Al, remaining crystalline. The total number of anti-site, non-lattice site atoms and vacancies produced is higher in NiAl than in Ni$_3$Al, being the number of atoms involved in clustering higher in NiAl although a higher number of small clusters form in Ni$_3$Al.
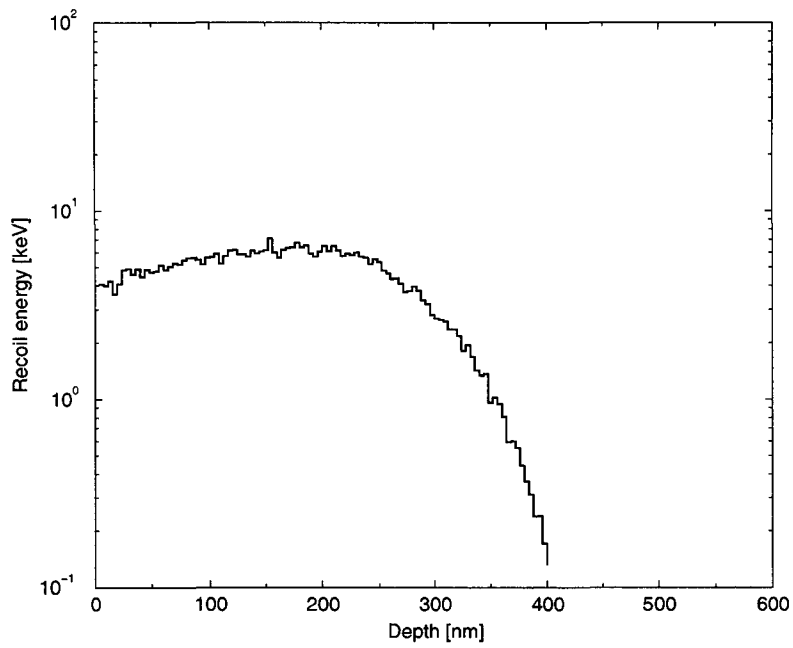
(a) Recoil energy
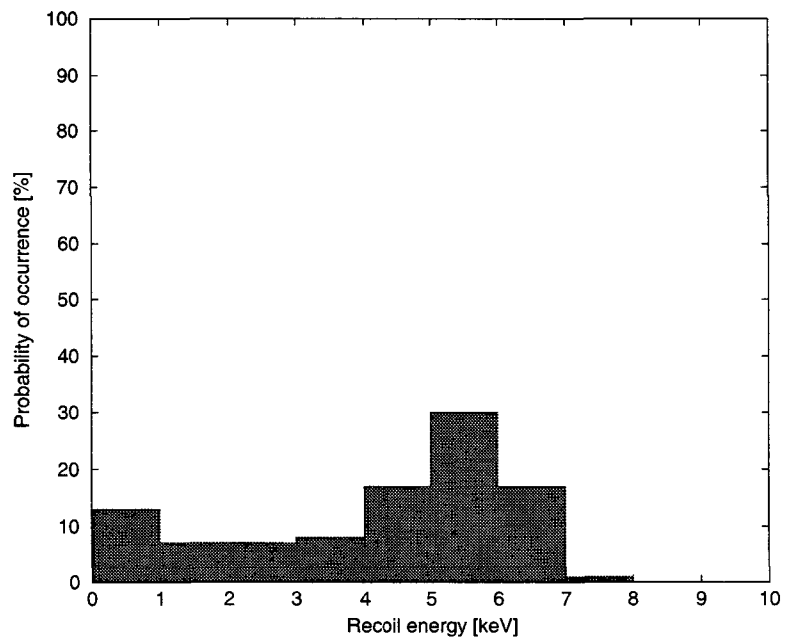
(b) Probability of occurrence

Figure 5.2: Monte Carlo computer simulations of the (a) recoil energy and (b) probability of occurrence distributions in NiAl for 700 keV-Ni primary ions.

(a) Recoil energy

(b) Probability of occurrence

Figure 5.3: Monte Carlo computer simulations of the (a) recoil energy and (b) probability of occurrence distributions in Ni_3Al for 700 keV-Ni primary ions.

(a) Recoil energy

(b) Probability of occurrence

Figure 5.4: Monte Carlo computer simulations of the (a) recoil energy and (b) probability of occurrence distributions in NiAl for 6 MeV-Ni primary ions.
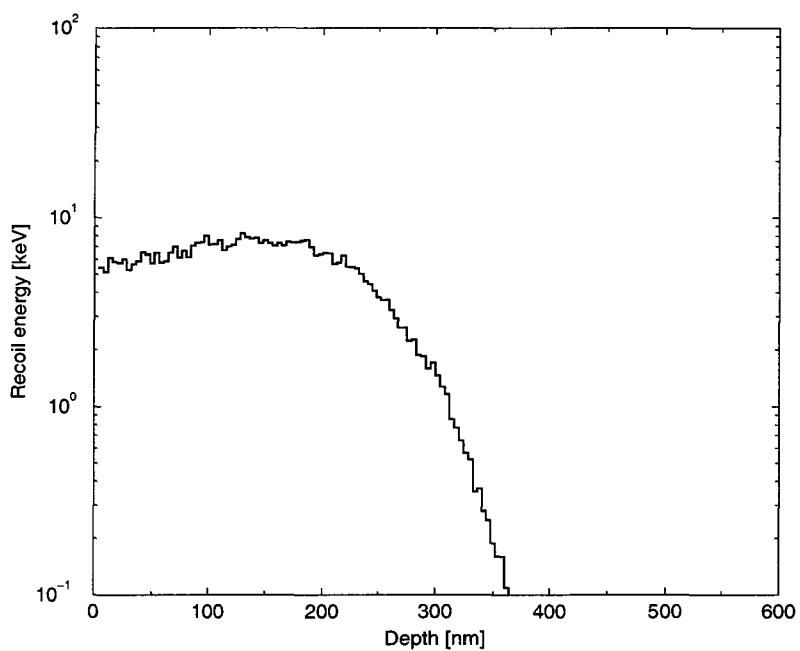
(a) Recoil energy

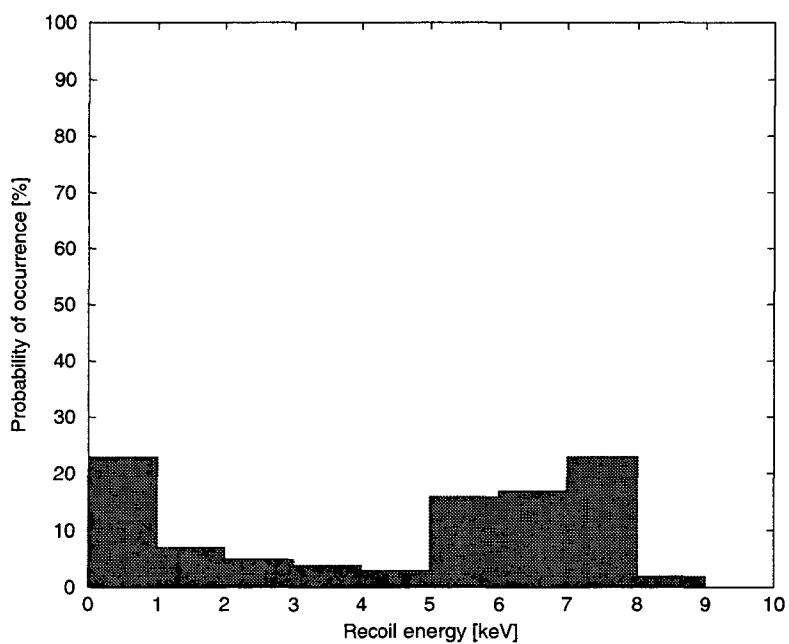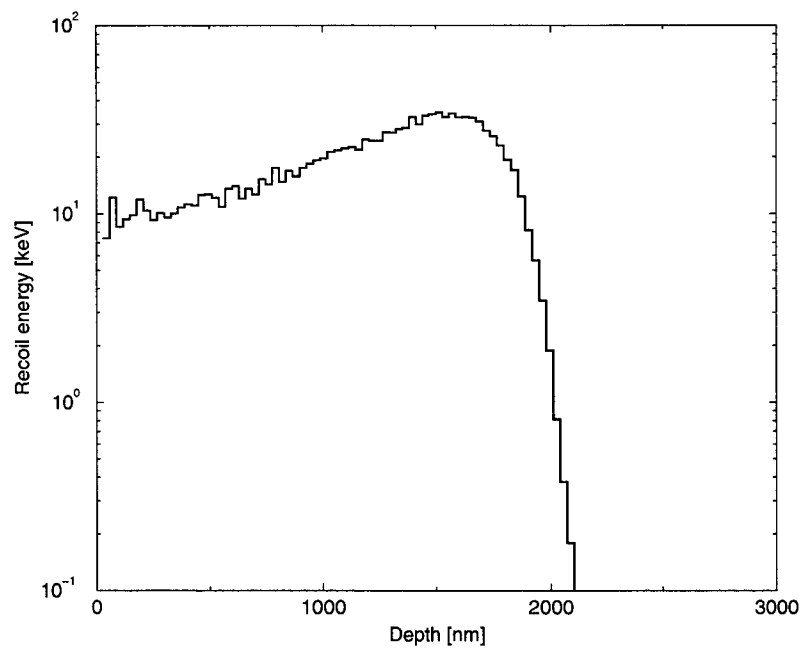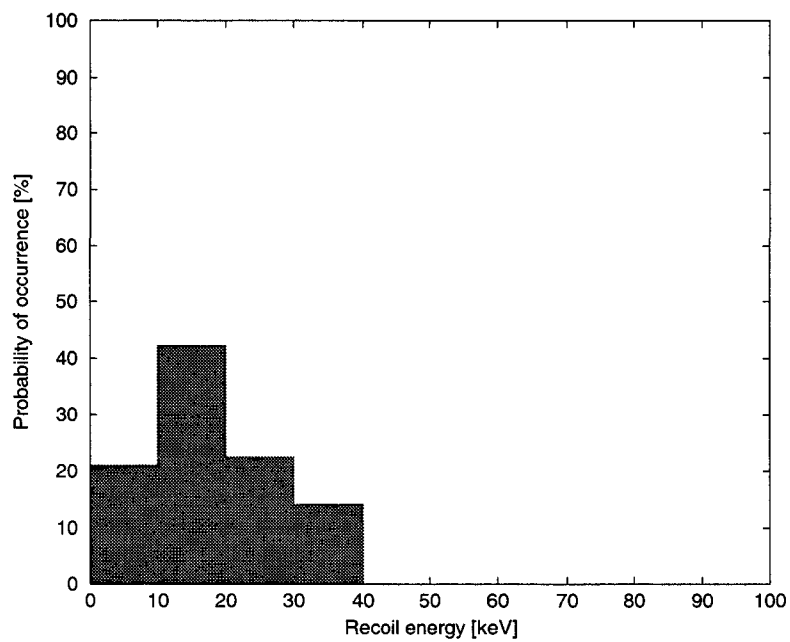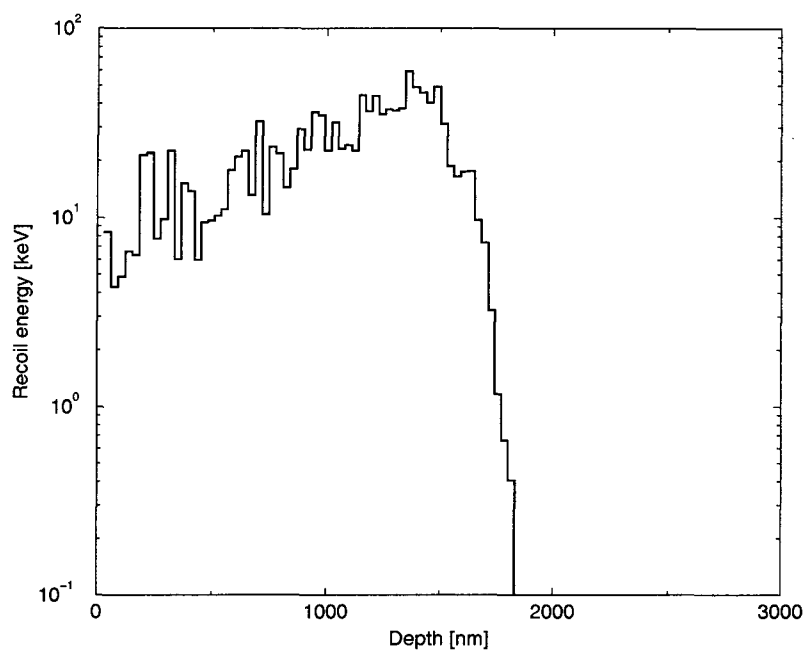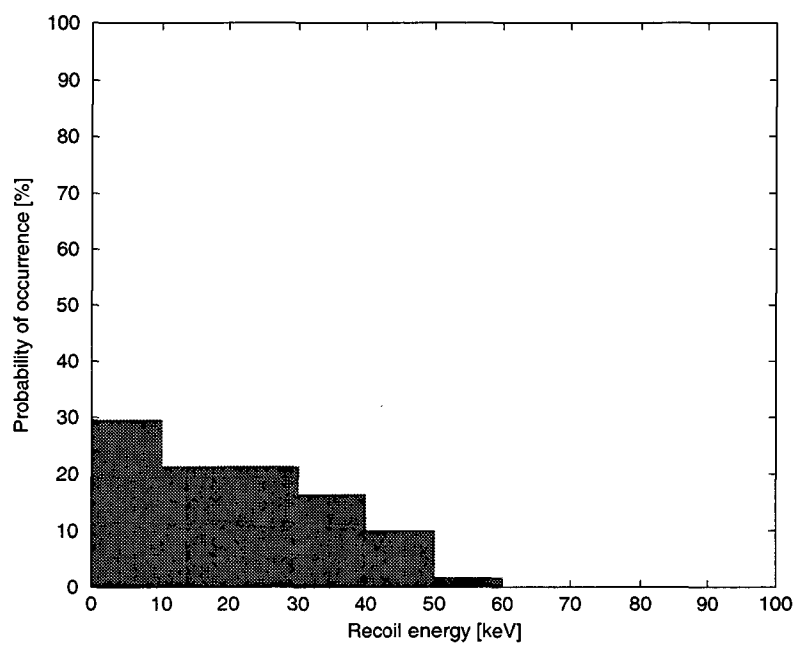(b) Probability of occurrence

Figure 5.5: Monte Carlo computer simulations of the (a) recoil energy and (b) probability of occurrence distributions in Ni_3Al for 6 MeV-Ni primary ions.

Cascade damage accumulation has been explored introducing a second energetic particle into the system (overlap) and following its evolution until the crystal is quenched. An overall increase in the number of anti-site atoms and of interstitial- and vacancy-type clusters is registered.

Image simulation has been applied to generate transmission electron microscopy micrographs of damaged intermetallic samples corresponding to a certain number of molecular dynamics simulation cases (de Almeida et al. 1999, Schäublin, de Almeida, Almazouzi & Victoria 2000). This technique has shown that high resolution and conventional transmission electron microscopy imaging are valuable in correlating cascade damage to actual microscopy micrographs. However, being these simulations quenched to 0 K, it is not straightforward to compare them to a set of experimental micrographs. It is possible, nevertheless, to describe what type of defects are formed and under which conditions they are visible.

High resolution appears to be very appropriate to imaging disordered zones at defoci below Scherzer so that Fresnel interference arises to form an image of enough contrast. This imaging mode, which has been shown to be able to identify individual point defects and clusters in pure metals (either nickel or aluminium), is not able to resolve the ambiguity between a disordered zone and a defect cluster and therefore should not be used in experimental observations except for very localized analyses. It has been shown, however, that either interstitial- or vacancy-type clusters can be imaged (or not), being their visibility dependent on the contrast transfer function intensity value.

Conventional transmission electron microscopy (CTEM) imaging mode is appropriate to differentiate these two types of objects for their imaging has two distinct origins: structure factor induced contrast and stress induced contrast. The former is used to identify disordered zones under a kinematical (preferred) or dynamical condition and the latter is used to image a defect due to its associated stress field. This imaging mode is important in order to understand how these defects are distributed on a two-dimensional projection and what the correlation is between the loci of disordered zones and defect clusters formed during the cooling of the cascade. Being the cascade subsequently quenched to 0 K it is not surprising to register a local correlation between disordered zones and defect clusters in the frozen microstructure. Regarding this mode, it is of particular interest the possibility of imaging an amorphous cluster and to be able to escape the experimental caveat of misinterpreting it for a crystalline defect under incorrect diffraction conditions.

A morphological characterization of disordered zones and defect clusters is possible through a direct measurement of these objects on the virtual micrographs (chapter 3). Information compiled from CTEM simulated images of molecular dynamics cascades (weak coupling) and liquid droplet model calculations (Almazouzi et al. 1999) is reported in Table 5.2 for both intermetallics and its elements, namely the

cluster mean size $\bar{x}_c$, disordered zone mean size $\bar{x}_d$, disordered zone to defect cluster densities ratio ρ_d/ρ_c, and maximum molten size $\bar{x}_m$.

Table 5.2: CTEM object maximum size, densities ratio, and maximum molten size (spherical approximation).

Mater.	$\bar{x}_c;\bar{x}_d$ [nm];ρ_d/ρ_c				$\bar{x}_m$ [nm]		
	10 keV	15 keV	2×15 keV	30 keV	10 keV	15 keV	20 keV
NiAl	1.1;4.2;0.5	1.8;4.6;1.0	1.5;5.3;0.5		4.6	5.3	5.8
Ni$_3$Al	1.6;3.4;0.7	1.2;2.3;0.3	1.6;4.8;1.0		4.6	5.3	5.8
Ni				1.4;—;—			
Al	1.4;—;—						

Results from molecular dynamics computer simulations of heavy-ion induced damage in NiAl and Ni$_3$Al indicate a higher number of interstitials than vacancies involved in clustering and therefore it is arguable that at 0 K the probability of rendering the former cluster visible is higher than for the latter. Under heavy-ion irradiation, low fluences (or doses), and temperatures below $0.3T_m$, where T_m is the melting temperature of the intermetallic, the observed defect densities (corresponding to visible objects) are at least one decade below the values reported in molecular dynamics simulations (Almazouzi et al. 1998). This information might be interpreted as due to partial defect invisibility under a certain diffraction condition and/or as evidence for a higher number of atoms preferably involved in anti-site occupation rather than non-lattice or vacant sitting. There is still experimental controversy on whether the actual type of defect clusters surviving after the cascade collapse are of interstitial- or vacancy-type. In most experiments these defect clusters have been identified as of vacancy-type (Jenkins et al. 1976, Jenkins & English 1982, Bui et al. 1995), thus resulting from the collapse of the vacancy rich cascade cores. The coupling of molecular dynamics simulations with image simulation results (defect contrast analysis) cannot provide us a self-consistent reply to this question. Simulation results report on the cascade damage effects pertaining to a recovery stage I, in which predominates the recombination of near vacancy-interstitial atom pairs and the free migration of interstitial atoms, accompanied by the formation of their clusters. Actual transmission electron microscopy observations are usually done at room temperature, and therefore at a recovery stage III, in which the free migration of mono- and divacancies predominates, leading to their annihilation on clusters of interstitial atoms and to formation of vacancy clusters.

From the set of comparative results (Table 5.2) on the behavior of NiAl and Ni$_3$Al under heavy-ion irradiation it can be inferred from the coupling of molecular dynamics and image simulations that defect cluster and disordered zone sizes appear to increase with increasing recoil energy in the case of NiAl, the opposite trend being registered for Ni$_3$Al (within 5 and 10% maximum error, respectively). A different

kinetics so that NiAl remains in a highly disordered state (which increases with increasing recoil energy) contrary to Ni_3Al, in which either an enhanced recombination of defects or reorder takes place at a higher recoil energy. This hypothesis is consistent with the fact that NiAl is known to undergo a crystalline-to-amorphous transformation (defect accumulation induced transformation), which does not occur in Ni_3Al, remaining in a disordered state. A liquid droplet treatment (chapter 1) reported, though, a distinct trend. Both intermetallics apparently have the same molten volume (or its projected diameter), which increases with increasing recoil energy.

The experimental fact that a defect cluster (of vacancy-type) has always a disordered zone associated with it, whereas a disordered zone might be (or not) associated with such a defect, has been previously reported (Jenkins et al. 1976, Jenkins & English 1982), which can be partly understood due to the reordering process occurring at stage III, when vacancies migrate freely, promoting clustering towards a disordered zone, which acts as driving force to the recombination process. Image simulation results have shown, however, that during stage I—which is representative of the molecular dynamics simulation conditions— though defect clusters (not necessarily of vacancy-type) are formed in the vicinity of the disordered zone, their quantity outnumbers those of the latter.

Irradiation-induced disordering and defect accumulation in NiAl and Ni_3Al has been studied by conventional transmission electron microscopy from two distinct sets of cross-sectional samples. A first set consisting of intermetallic thin films of stoichiometric NiAl and Ni_3Al, the main purpose of which being a direct measure of ion-mixing and the assessment of a direct crystalline-to-amorphous transformation. However, due to the choice of fluences (or doses) in the range 10^{14}–10^{15} cm^{-2} (0.1–1.5 dpa), these objectives could not be fully accomplished. A direct measurement of the ion-mixing value, which was technically insubstantial, is probably within the range 1.0-10.0 nm^2/dpa (Naundorf 1999). A second set of bulk intermetallic single-crystals has been prepared, the main purpose of which being the comparative morphological description of damaged NiAl and Ni_3Al. Disordered zones have been identified by selecting an appropriate superlattice reflection in dark-field imaging (tilted illumination) either from kinematical or dynamical diffraction conditions. Defect clusters have been identified under weak-beam dark-field imaging conditions which evidence best their elastic displacement field.

For the range of primary ion energies chosen in this work—700 keV and 6 MeV—the displacement cross-section, which is the controlling parameter during the collisional phase of the cascade, is in the range 9.52×10^{-20}–1.54×10^{-19} m^2. Both NiAl and Ni_3Al have been irradiated up to fluences of 10^{14}–10^{15} cm^{-2} (0.1–1.5 dpa) at room temperature. A control group of layered NiAl has been used in order to evaluate a direct crystalline-to-amorphous transformation, which did not take place either at liquid nitro-

gen or room temperature. At these regimes it has been shown that the electronic stopping dominates over the nuclear one and that subcascade formation must play a major role in disordered zone and defect cluster formation for their sizes do not scale according to a phenomenological power law. A morphological estimation of defect clusters and disordered zones indicate that their mean sizes are 2.5 and 4.5 nm, respectively, and the corresponding densities 1.5×10^{23} and 7.0×10^{22} m^{-3}. These values are comparable to the defect cluster and disordered zone sizes estimated with image simulation of molecular dynamics of damaged intermetallics lying in the range 1.0–3.0 nm and 3.0–5.0 nm, respectively, and consistent with Monte Carlo simulations using TRIM, yielding maximum cascade sizes in the range 1.1–1.8 nm (spherical approximation).

A direct comparison between cascade damage accumulation and fluence (or dose) is severed due to an inherently limited statistical confidence in molecular dynamics dose simulation. Despite this serious limitation, it is possible to estimate fluence (or dose) values from the number of primary recoils introduced in the molecular dynamics simulation box, supposing that those recoils are representative of 700 keV-nickel and 6 MeV-nickel primary ions recoil distributions. In so being, fluence to dose conversions can be consistently evaluated, as reported in Table 5.3. These results indicate that those molecular dynamics computer simulations are dose comparable for a specific recoil energy, within 10 to 30% error. However, fluence determination is measured within 20% experimental error—which is therefore propagated to the dose—validating then the coupling of molecular dynamics results and image simulation.

Table 5.3: Fluence to dose conversion.

Mater.	Φ [cm^{-2}]			G [dpa]		
	10 keV	15 keV	2×15 keV	10 keV	15 keV	2×15 keV
NiAl	5.7×10^{11}	7.5×10^{11}	1.1×10^{12}	8.6×10^{-4}	7.5×10^{-4}	1.1×10^{-3}
Ni$_3$Al	4.9×10^{11}	4.9×10^{11}	9.8×10^{11}	7.4×10^{-4}	4.9×10^{-4}	9.8×10^{-4}

Transmission electron microscopy of irradiated NiAl has proved amorphization does not occur at high energies and low fluences (or doses), and therefore a defect accumulation threshold should exist which drives the crystalline-to-amorphous transformation. In this context molecular dynamics computer simulations must probably be reviewed in order to evaluate the electron-phonon coupling validity domain. A more complete study should be required for the low fluence regimes in which cascades are isolated so that a more detailed comparison with molecular dynamics computer simulations can be made.

Microstructural evolution under heavy-ion irradiation must be thought on the basis of the disordered zone to defect cluster densities ratio, ρ_d/ρ_c, in order to compare both intermetallics in a self-consistent approach due to different fluences (or doses), and primary ion energies. From a structural point of view it

is indeed interesting to compare the two intermetallics. Being ρ_d/ρ_c an estimator of irradiation-induced disordering efficiency, it is now arguable that at the high energy regime this ratio decreases with increasing primary ion energy. This fact is best understood knowing that subsequently to the collisional phase of the displacement cascade up to 80–90% of defects are annihilated either through recombination at sinks or due to reordering into their corresponding sublattices in a thermally activated process. Moreover, as the ratio is higher in NiAl than in Ni_3Al for equivalent irradiation conditions, a larger fraction of disordered zones did not reorder and therefore a lower (higher) long-range order (disordering efficiency) value might be inferred. These results corroborate the estimated disordering efficiency parameter ε determined for Ni_3Al (as compared to other authors) and the decreasing defect cluster and disordered zone sizes predicted in the frame of image simulations.

Radiation damage effects on order-disorder in intermetallics have been first studied and quantified in the seminal works of Siegel (1949) and Aronin (1953), and subsequently reviewed in the framework of ordering and disordering of solid solutions under irradiation by Schulson (1979). The study of radiation damage in ordered intermetallics has been of paramount importance in understanding alloy stability in structural materials for nuclear and future fusion reactors (Nelson et al. 1972, Hudson 1975), namely of precipitate dissolution and disordering mechanisms in nickel-based superalloys (Abromeit et al. 1995, Camus et al. 1996). From a fundamental research point of view intermetallics constitute controllable systems for the assessment of radiation-induced phase transitions (order → disorder, amorphization) and defect production (Nastasi & Mayer 1991, Abromeit & Naundorf 1996).

Experimental work on ion induced disordering and precipitate dissolution as well as the production and development of displacement cascades in nickel aluminides has been reported in the work of Abromeit & Naundorf (1996), Müller (1997), Müller et al. (1997), Müller et al. (1999), Ewert (1998), and Ewert et al. (1998). A series of molecular dynamics computer simulations and image simulation studies on heavy-ion induced disordering on the nickel-aluminium system have been presented by Spaczér et al. (1997) and de Almeida et al. (1999), respectively, in order to establish valid links between experimental data and cascade damage models. Long-range order precise quantification using transmission electron microscopy in selected area diffraction mode was first developed by Kimoto & Saito (1994), which is based on the evaluation of superlattice to fundamental reflection intensity ratios. An equivalent experimental setup has been used to determine the amount of amorphous material in irradiated intermetallics and reviewed by Motta (1997).

Aronin's exponential law $S = S_0 \exp(-\varepsilon\Phi)$ is characterized by the initial long-range order value S_0, the dose in dpa Φ, and the disordering efficiency ε, which is in the range of 1–3 /dpa for electrons and 10–

100 /dpa for ions. Müller (1997) and Ewert et al. (1998) have separately reported equivalent 300 keV nickel room temperature ion irradiations in bulk Ni_3Al, but their values for ε differ by a factor of 2. Fluence to dpa conversion is normally made under the assumption that the displacement cross-section, σ_d, is constant within the projected range of the incoming ions, which happens to be the case in the low primary energy regime they have used. However, the authors differ almost by a factor of 3/2 on the displacement threshold energy value E_d (Zhu et al. 1995) for Ni_3Al and therefore, as the vacancy production distributions evaluated with TRIM (Biersack & Haggmark 1980) are not equal, a discrepancy between the displacement cross-sections and the corresponding fluence to dpa conversion factors arise and might explain a systematic error in their estimated doses and consequently of the long-range order values measured.

Müller (1997) and Ewert et al. (1998) have used equivalent quantifications of superlattice to fundamental reflection intensity ratios, being $S = f(I_s/I_f)$ in the context of dynamic diffraction theory (Hirsch et al. 1977), which have been simulated as a function of sample thickness using the EMS software package (Stadelmann 1987). Their approaches being valid from a fundamental view point are nonetheless limited due to sample geometry and its inherent thickness variation, and due to a selected area aperture minimum size which collects high-order diffracted electron beams in a main zone axis orientation, not accounted for in the simulation. The ratios of superlattice to fundamental reflection intensities reported are then used to indirectly quantify the long-range order parameter based on image simulation information for an estimated thickness range. In the present chapter, a self-consistent long-range order quantification method for ion-irradiated intermetallics is described.

At the low primary ion energy regime used in the work of Müller (1997) and Ewert et al. (1998), the displacement cross-section is almost constant within the projected range of the incoming ions, whereas at the high primary ion energy regime used in the present investigation, the displacement cross-section increases by almost a decade (Figure 2.16(b)) due to the behavior of nuclear and electronic stopping power with energy (Figure 2.17(b)).

Information on the superlattice to fundamental reflection ratio has been established on the basis of selected area dynamic diffraction orienting the crystal to a $[\bar{1}12]$ zone axis and evaluating the intensities of the (110) and (220) reflections, I_{110} and I_{220}, respectively, with a Gatan CCD camera. Being $S = f(I_{110}/I_{220})$, the validity of an approximation of type $S^2 \propto I_{110}/I_{220}$, including the absorption effect, has been tested in the thickness range corresponding to the specific crystal as described. Having knowledge on the intensity ratio $(I_{110}/I_{220})_n$ for the non-irradiated bulk, and therefore for $S = 1$, it has been possible to precisely quantify the estimated crystal thickness yielding 103 nm and to conduct a series

of transmission electron microscopy simulations using EMS in order to assess this approximation within the experimental conditions. The dependency of the normalized amplitude ratio A_{110}/A_{220} with S, where A_{hk0} stands for the beam amplitude ($I_{hk0} = A_{hk0}^2$), has been plotted and compared to the approximation (Figure 5.6). In so doing, S can be estimated within a relative error of 9%. A minimum size selected area aperture has been chosen and measured using the CCD camera yielding approximately 150 nm in diameter. This value therefore defined our maximum spatial resolution and corresponds to 0.3% of the one used in the work of Müller (1997).

An automatic electron probe displacement control in image mode has been implemented in order to measure superlattice to fundamental intensity ratios from the surface of the incoming ions down to the non-irradiated bulk. Using the above mentioned procedure the long-range order parameter may be plotted as function of depth (Figure 5.7) and consequently of dose (Figure 5.8) which is directly proportional to the displacement cross-section, σ_d.

For a total fluence of 10^{14} cm^{-2}, equivalent doses of 0.02 and of 0.10 dpa are obtained close to the surface of the incoming ions and at the projected range, respectively. Aronin's exponential law is fitted to the set of data measured (Figure 5.8) yielding a correlation square of 99.8% and a disordering efficiency constant ε, in the range of 10.0±0.7 /dpa. This value is below the ones estimated from the data of Müller (1997) and Ewert (1998), 30 /dpa and 16 /dpa, respectively (Figure 5.9). However, in the high primary energy regime the maximum displacement cross-section is 40% of the equivalent one in the low primary energy regime.

Monte Carlo computer simulation (TRIM) of the recoil distributions for both energies show a comparatively reduced number of Frenkel pairs being produced at high-energy, the smaller cross-section value being a direct consequence of this fact. Moreover, it is well known that the defect recombination in the thermal spike phase of the cascade evolution reduces the number of surviving defects to 10–20% of those produced in the collisional phase (Spaczér et al. 1994a), and therefore a less effective disordering mechanism should be active (Komarov 1992). Maximum disordering is measured at the projected range (Figure 5.7), in accordance with the displacement cross-section distribution behavior. Long-range order is observed to recover to its maximum value due to the asymptotic decay of the displacement cross-section beyond the projected range. Aronin's exponential law does not explicit any knowledge on the nature of ε. The disordering efficiency ε is certainly a function of the disordered zone to defect cluster densities ratio, $\varepsilon = f(\rho_d/\rho_c)$. Further validation of such a relation would be of paramount importance in order to understand irradiation-induced disordering at high primary ion energies and to establish the fact that a less effective disordering process takes place in a regime of dominant subcascade formation.

The long-range order measurement technique here discussed is very appropriate to estimate disordering efficiency in the high primary energy ion-irradiation regime where the projected range is located far from the surface of the incoming ions (de Almeida, Schäublin, Almazouzi, Victoria & Döbeli 2000). It is a unique method to measure precisely long-range order as function of dose for a single total fluence using selected area diffraction depth profiling. This method can be applied to the low primary energy regime provided electron nano-diffraction is used. Measurements of chemical long-range order in non-irradiated nickel aluminides using nano-diffraction have been recently reported (de Almeida, Schäublin, Almazouzi, Victoria & Lévy 2000) using a probe resolution of 10 nm, confirming its applicability to a variety of primary ion energies.
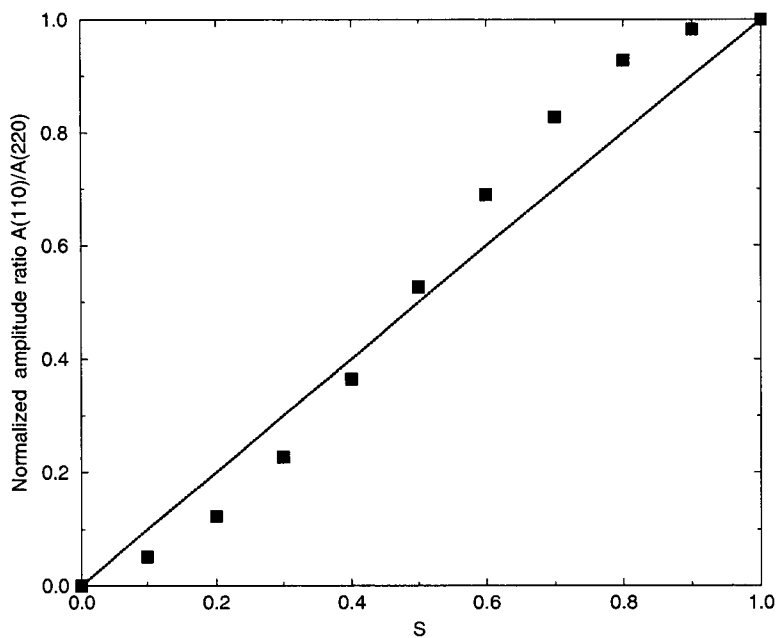
Figure 5.6: Normalized amplitude ratio A_{110}/A_{220} dependency with the long-range order parameter S for a $[\bar{1}12]$ zone axis.
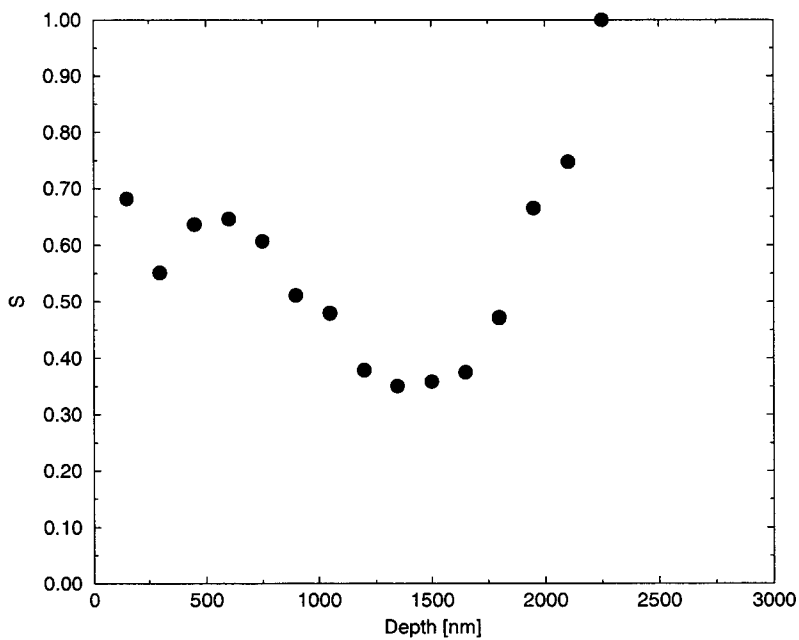

Figure 5.7: Long-range order as function of depth (minimum at the projected range) for bulk Ni_3Al irradiated with 6 MeV double charged nickel ions at RT to 10^{14} cm^{-2}.
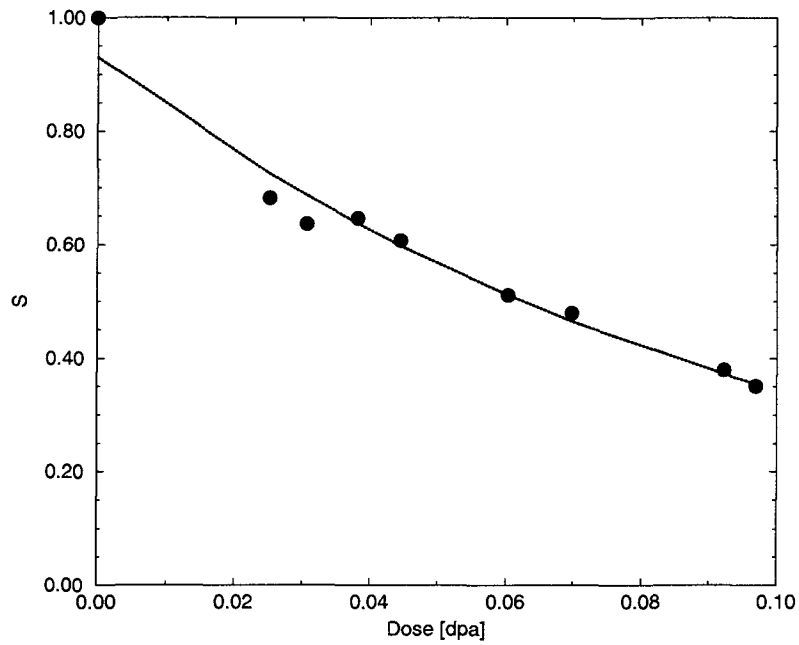
Figure 5.8: Long-range order as function of dose for bulk Ni_3Al irradiated with 6 MeV double charged nickel ions at RT to 10^{14} cm^{-2}.

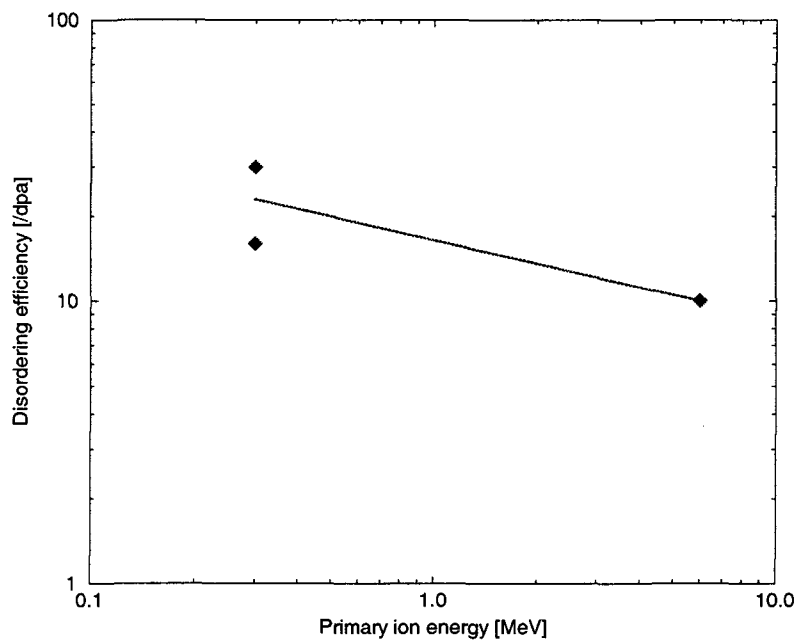
Figure 5.9: Disordering efficiency in Ni_3Al as function of the primary nickel ion energy.

Within the framework of Bragg and Williams these results suggest that the redistribution of atomic species from the most densely populated sublattice into the less populated one does control the disordering mechanism. In NiAl, the disordering mechanism is most probably symmetric due to its two equivalent sublattices. Molecular dynamics results, however, have indicated that approximately the same number of nickel and aluminium anti-site atoms are created under cascade damage in both NiAl and Ni_3Al (Spaczér et al. 1997). In spite of the pertinent formulation described in chapter 1 after Bragg and Williams—which does not account for the existence of interstitial- and vacancy-type defects—the ratio of the probabilities of anti-site occupation due to the latter compound stoichiometry is not being respected. Actually, this could imply that the number of anti-site aluminium atoms created under cascade conditions is over-estimated for Ni_3Al (or in equivalent form, that the number of non-lattice site aluminium atoms is reduced). The current results indicate that both NiAl and Ni_3Al have a defect accumulation behavior (Figure 5.10) other than iron (bcc) or copper (fcc), respectively, although it might be comparable to pure nickel (fcc), close to the saturation regime. Being the data scarce it is not yet possible to draw a definitive conclusion on why do these intermetallics have a comparable defect accumulation behavior, within experimental error, despite their distinct B2 and $L1_2$ lower symmetry crystalline structures.
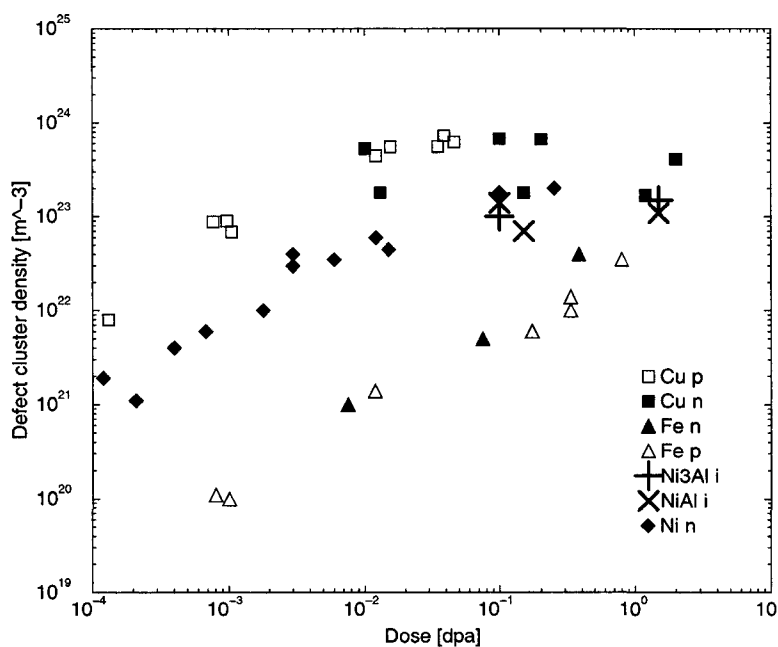

Figure 5.10: Defect cluster densities measured for Cu (Victoria et al. 2000), Fe (Victoria et al. 2000), Ni (Kiritani et al. 1990, Zinkle & Snead 1995), NiAl (this work), and Ni_3Al (this work).

It has been clearly demonstrated that NiAl has a disordering kinetics faster than Ni_3Al, which is measurable by the ratio ρ_d/ρ_c and the disordering efficiency parameter ε. At a predominant electronic stopping irradiation regime it appears that neither fluence (within a decade) nor energy (within a decade) have a

significant influence on the observed object sizes or densities within experimental error. It is the ratio of densities itself which correlates to the primary ion energy (or in an equivalent form to the displacement cross-section). These observations can be compared to similar ones in copper and nickel at low fluences (or doses) in which defect mean sizes do not change within 3 decades.

5.1 Conclusions

The study of the microstructure and growth modes of stoichiometric NiAl and Ni$_3$Al thin films deposited by r.f.-magnetron co-sputtering as proper irradiation media has remarkably demonstrated the heteroepitaxial inverse Nishiyama-Wassermann relationship for NiAl grown onto nickel single-crystals and the heteroepitaxy of Ni$_3$Al.

A numerical link between molecular dynamics and transmission electron microscopy image simulation of cascade damage in NiAl and Ni$_3$Al has been objectively established (from a microscopist perspective) for a morphological and quantitative analysis of irradiation-induced effects has been systematically applied in order to evaluate the influence of primary ion energy and damage accumulation (cascade overlap) in their microstructures.

A microstructural investigation using transmission electron microscopy of heavy-ion irradiated NiAl and Ni$_3$Al reported two different disordering processes. The existence of a direct crystalline-to-amorphous transformation in the former has been rejected on the basis of experimental evidence, stressing a defect accumulation driven transformation. Microstructural evolution after heavy-ion irradiation is better described on the basis of the disordered zone to defect cluster densities ratio, ρ_d/ρ_c, in order to compare both intermetallics in a self-consistent approach due to different fluences (or doses), and primary ion energies. This ratio has been seen to decrease with increasing primary ion energy. Furthermore, under equivalent irradiation conditions NiAl has been seen to disorder faster than Ni$_3$Al.

5.2 Prospects

The present results can be further expanded into two new directions, namely:

- The heavy-ion irradiation of bulk nickel aluminides at fluences in the range 10^{12}–10^{13} cm^{-2} (0.001–0.015 dpa) in order to fully characterize and identify individual cascades and defect clusters using conventional transmission electron microscopy;

and

- the heavy-ion irradiation of layered nickel aluminides at fluences in the range 10^{16}–10^{17} cm^{-2} (10.0–150.0 dpa) in order to quantify the ion-mixing at high primary ion energies using cross-sectional secondary ion mass spectrometry and evaluate an eventual crystalline-to-amorphous transition (defect accumulation induced transformation) using cross-sectional conventional transmission electron microscopy.

Appendix A

Many-beam dynamical calculation of CTEM contrasts

In many cases where high resolution is of primary importance it is very appropriate to form an image from the electrons which are scattered by a small fraction of the total number of atoms in the crystal. Such type of images might be obtained in dark-field using a portion of the diffracted pattern where the scattering of interest is dominant over the uninteresting signal from the surrounding crystal. For this purpose tilted illumination is used so that the scattered electron waves collected travel as close as possible to the optic axis.

A well known example is described in the article of Cockayne et al. (1969), to obtain high resolution images of lattice defects such as dislocations by the strain contrast mechanism. In this case a dark-field image is formed from a weak Bragg reflection located far from the reflecting position in the surrounding crystal.

Weak beam methods of slightly different type have been employed by Jenkins et al. (1976), which use one of a family of superlattice reflections in an ordered matrix to detect disordered regions at displacement cascades formed after irradiation by the structure factor mechanism.

CUFOUR is an image simulation program developed to quantitatively evaluate conventional transmission electron microscopy (CTEM) images of multiple linear and planar defect configurations (Schäublin & Stadelmann 1993, Schäublin 1998).

Many-beam calculation of CTEM images has been deployed and reported in the works of Schäublin & Stadelmann (1993) and Baluc & Schäublin (1996) for simulating electron microscope dislocation images

and superdislocations, respectively.

In the present work, CUFOUR has been used to study CTEM contrast formation in an inclined rod of a chemically disordered intermetallic (first medium) embedded into a fully ordered matrix of the same material (second medium). A dislocation line 2.5 nm in core radius with zero Burger's vector modulus has been defined for that purpose. Foil thickness has been set to 100 nm. Diffraction conditions have been selected in order to evidence the structure factor contrast difference between the disordered and ordered media. The elastic constants C_{11}, C_{12}, and C_{44} are reported from the works of Lequeux (1979) and Baluc (1990). Tables A.1 and A.2 summarize the input data used in the calculations and a set of parameters of interest (namely, the real part of the structure factor, $\Re(F_{hkl})$, and the extinction distance, ξ_g) in order to understand how peculiar ordered structures are.

Table A.1: CUFOUR input data.

Mater.	Acc. [kV]	$C_{11}/C_{12}/C_{44}$ [GPa]	Foil norm.	Disl. dir.	Syst. row	LCC
NiAl	200	206.4/134.1/116.0	[011]	[211]	[100]	(0.6,0,0)
Ni$_3$Al	200	220.1/146.0/123.6	[$\bar{1}$12]	[021]	[110]	(0.6,0.6,0)

Table A.2: Structure factors and extinction distances data.

Mater.	$\vec{g} = (hkl)$	g [nm^{-1}]	$d_{(hkl)}$ [nm]	$\Re(F_{hkl})$ [V]	ξ_g [nm]
NiAl	(001)	3.46	0.2887	-3.24	185.2
	(101)	4.90	0.2041	12.87	45.6
	(111)	6.00	0.1667	-2.98	201.2
	(002)	6.93	0.1444	8.66	69.3
Ni$_3$Al	(001)	2.80	0.3570	-1.65	362.4
	(101)	3.96	0.2524	-1.72	348.7
	(111)	4.85	0.2061	15.44	38.8
	(002)	5.60	0.1785	13.40	44.8

Many-beam calculations under the above mentioned diffraction conditions enable a detailed evaluation of the object contrast variation within the foil depth.

Figures A.1(a) and A.1(b) represent superlattice (100) and fundamental (200) dark-field images, respectively, for NiAl. Figures A.2(a) and A.2(b) represent superlattice (110) and fundamental (220) dark-field images, respectively, for Ni$_3$Al.
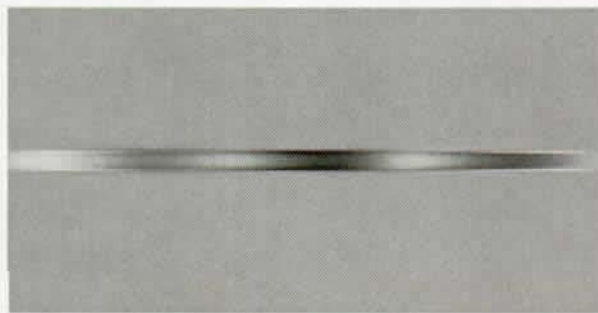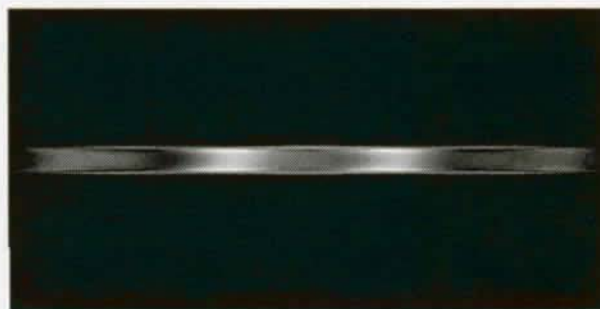
(a) DF (100)

(b) DF (200)

Figure A.1: Many-beam calculation of CTEM contrast in dark-field imaging mode for NiAl under (a) superlattice reflection (100) and (b) fundamental reflection (200). Scale bar is 10 nm.

(a) DF (110)

(b) DF (220)

Figure A.2: Many-beam calculation of CTEM contrast in dark-field imaging mode for Ni_3Al under (a) superlattice reflection (110) and (b) fundamental reflection (220). Scale bar is 10 nm.

Bibliography

Abromeit C, Müller S & Wanderka N 1995 *Scripta Metal. Mater.* **32**, 1519–1523.

Abromeit C & Naundorf V 1996 *Intermetallics* **4**, 441–446.

Alexander D E, Was G S & Rehn L E 1991 *J. Appl. Phys.* **69**, 2021–2028.

Almazouzi A 1999. Private communication.

Almazouzi A, Spaczér M, Alurralde M & Victoria M 1998 *Mat. Res. Soc. Symp. Proc.* **481**, 371–376.

Almazouzi A, Spaczér M, Alurralde M & Victoria M 1999 *in* 'Proceedings of the International Conference on Solid-Solid Phase Transformations (JIMIC-3)' pp. 421–424.

Alurralde M, Caro A & Victoria M 1991 *J. Nucl. Mater.* **183**, 33–45.

Alurralde M, Caro A & Victoria M 1993 *J. Mater. Res.* **8**, 449–454.

Aoki K & Izumi O 1975 *Phys. Stat. Sol. (a)* **32**, 657–664.

Aronin L R 1953 *J. Appl. Phys.* **25**, 344–349.

Ball A 1967 *Met. Sci. J.* **1**, 47–48.

Baluc N L 1990 Contribuition a l'etude des defauts et de la plasticite d'un compose intermetallique ordonne: Ni₃Al Ph.D. Dissertation No. 886 Swiss Federal Institute of Technology Lausanne.

Baluc N & Schäublin R 1996 *Phil. Mag. A* **74**, 113–136.

Bauer E & van der Merwe J H 1986 *Phys. Rev. B* **33**(6), 3657–3671.

Bethe H A & Wills H H 1935 *Proc. Roy. Soc. A* **150**, 552–575.

Biersack J P & Haggmark L G 1980 *Nucl. Instr. and Meth.* **174**, 257–269.

Birchenall C E 1952 *in* 'Physical factors affecting order in metallic systems' American Society for Metals, Cleveland, Ohio.

Bragg W L & Williams E J 1934 *Proc. Roy. Soc. A* **145**, 699–730.

Bragg W L & Williams E J 1935 *Proc. Roy. Soc. A* **151**, 540–566.

Brimhall J L, Kissinger H E & Charlot L A 1983 *Radiat. Eff.* **77**, 273–293.

Brimhall J L & Simonen E P 1986 *Nucl. Instr. and Meth. Phys. Res.* **B16**, 187–192.

Bui T X, Robertson I M & Kirk M A 1995 *Mat. Res. Soc. Symp. Proc.* **373**, 63–68.

Bunshah R F, ed. 1994 *Handbook of Deposition Technologies for Films and Coatings* second edn Noyes Publications.

Buschow K H J 1977 *Rep. Prog. Phys.* **40**, 1179–1256.

Cahn R W, Haasen P & Kramer E J, eds 1993 *Processing of Metals and Alloys* Vol. 15 of *Materials Science and Technology* VCH.

Camus E, Abromeit C, Bourdeau F, Wanderka N & Wollenberger H 1996 *Phys. Rev. B* **54**(5), 3142–3150.

Caro A & Victoria M 1989 *Phys. Rev. A* **40**, 2287–2291.

Caro A & Victoria M 1990 *J. Mater. Res.* **5**, 1409–1413.

Caro M, Ardelea A & Caro A 1990 *J. Mater. Res.* **5**, 2652–2657.

Chakravorty S & Wayman C M 1976*a* *Met. Trans. A* **7A**, 555–568.

Chakravorty S & Wayman C M 1976*b* *Met. Trans. A* **7A**, 569–582.

Cockayne D, Ray I & Whelan M 1969 *Phil. Mag. A* **20**, 1265.

Corey C L & Lisowsky B 1967 *Trans. Met. Soc. AIME* **239**, 239–243.

Cottrell A H 1962 *Theoretical Structural Metallurgy* second edn Edward Arnold (Publishers) Ltd.

Cowley J & Moodie A 1957 *Acta Cryst.* **10**, 609.

Czanderna A W, ed. 1975 *Methods of surface analysis* Elsevier Scientific Publishing Company.

Daw M S, Foiles S M & Baskes M I 1993 *Mater. Sci. Reports* **9**, 251–310.

de Almeida P, Schäublin R, Almazouzi A & Victoria M 1999 *in* J. M Aragonés, C Ahnert & O Cabellos, eds, 'Mathematics and Computation, Reactor Physics and Environmental Analysis in Nuclear Applications, Madrid' Vol. 2 pp. 1162–1172. ISBN 84-699-0943-6.

de Almeida P, Schäublin R, Almazouzi A, Victoria M & Döbeli M 2000 *Appl. Phys. Lett.* **77**, 2680–2682.

de Almeida P, Schäublin R, Almazouzi A, Victoria M & Lévy F 2000 *Thin Solid Films* **368**, 26–34.

de la Rubia T D 1989 The Structure and Dynamics of Energetic Displacement Cascades in Cu and Ni. A Molecular Dynamics Computer Simulation Study Ph.D. Dissertation State University of New York at Albany.

de la Rubia T D, Caro A & Spaczér M 1993 *Phys. Rev. B* **47**, 11483–11486.

de la Rubia T D, Caro A, Spaczér M, Janaway G A & Guinan M W 1993 *Nucl. Instr. and Meth. Phys. Res.* **B80/81**, 86–90.

de la Rubia T D & Guinan M W 1990 *J. Nucl. Mater.* **174**, 151–157.

de la Rubia T D, Guinan M W & Caro A 1994 *Radiat. Eff. Def. Sol.* **130/131**, 39–54.

de Novion C 1994 *in* J. H Westbrook & R. L Fleischer, eds, 'Intermetallic Compounds' John Wiley & Sons Ltd.

Delavignette P, Richel H & Amelinckx S 1972 *Phys. Stat. Sol. (a)* **13**, 545–555.

Dimitrov C, Sitaud B, Zhang X, Dimitrov O, Dedek U & Dworschak F 1992*a J. Phys.: Condens. Matter* **4**, 10199–10210.

Dimitrov C, Sitaud B, Zhang X, Dimitrov O, Dedek U & Dworschak F 1992*b J. Phys.: Condens. Matter* **4**, 10211–10226.

Du Y & Clavaguera N 1996 *J. Appl. Cryst.* **237**, 20–32.

Ehrhart P 1991 *in* H Ullmaier, ed., 'Atomic Defects in Metals' Vol. 25 Springer-Verlag.

Ellner M, Kek S & Predel B 1989 *J. Less-Common Met.* **154**, 207–215.

Enami K & Nenno S 1971 *Met. Trans.* **2**, 1487–1490.

English C A & Jenkins M L 1987 *Mater. Sci. Forum* **15-18**, 1003–1022.

Eridon J & Was G S 1988 *J. Mater. Res.* **3**, 626–638.

Ewert J C 1998 Ionenbestrahlungsinduzierte Phasenumwandlungen im System Nickel-Aluminium Ph.D. Dissertation Georg-August-Universität zu Göttingen.

Ewert J C, Schmitz G, Harbsmeier F, Uhrmacher M & Haider F 1998 *Appl. Phys. Lett.* **73**, 3363–3365.

Finnis M W 1988 MOLDY6—A Molecular Dynamics Program for Simulation of Pure Metals Technical Report HL88/1362(C17) Theoretical Physics Division, Harwell Laboratory.

Gao F & Bacon D J 1995*a* *Phil. Mag. A* **71**, 43–64.

Gao F & Bacon D J 1995*b* *Phil. Mag. A* **71**, 65–84.

Girgis K 1983 *in* R. W Cahn & P Haasen, eds, 'Physical Metallurgy' third edn Vol. 1 Elsevier Science Publishers BV chapter Structure of Intermetallic Compounds.

Glocker D A & Shah S I, eds 1995 *Handbook of Thin Film Process Technology* Institute of Physics Publishing.

Haasen P 1996 *Physical Metallurgy* third edn Cambridge University Press.

Hangen U, Bögershausen H & Sauthoff G 1996 *Prakt. Metallogr.* **33**, 531–539.

Harper J M E & Rodbell K P 1997 *J. Vac. Sci. Technol. B* **15**(4), 763–779.

Hellwig O, Theis-Bröhl K, Wilhelmi G & Zabel H 1998 *Thin Solid Films* **318**, 201–203.

Hentzel H T G, Grovenor C R M & Smith D A 1984 *J. Vac. Sci. Technol. A* **2**(2), 218–219.

Hessler A 1999 Étude de zones amorphes induites dans l'aluminium par implantation de nickel Ph.D. Dissertation No. 1966 Swiss Federal Institute of Technology Lausanne.

Hirsch P B, Howie A, Nicholson R B, Pashley D W & Whelan M J 1977 *Electron Microscopy of Thin Crystals* Robert E. Krieger Publisher Co., Inc.

Hobbs L W 1995 *J. Non-Cryst. Solids* **182**, 27–39.

Hofmann S 1992 *J. Vac. Sci. Technol. B* **10**(1), 316–322.

Howe L M 1994 *in* J. H Westbrook & R. L Fleischer, eds, 'Intermetallic Compounds' John Wiley & Sons Ltd.

Huang W & Chang Y A 1998 *Intermetallics* **6**, 487–498.

Hudson J A 1975 *J. Br. Nucl. Energy Soc.* **14**(2), 127–136.

Hughes T, Lautenschlager E P, Cohen J B & Brittain J O 1971 *J. Appl. Phys.* **42**, 3705–3716.

Hung L S, Nastasi M, Gyulai J & Mayer J W 1983 *Appl. Phys. Lett.* **42**, 672–674.

Ishida M, Yuda S, Kamigaki K, Terauchi H, Hiyamizu S & Sano N 1992 *Surf. Sci.* **267**, 54–56.

Jaouen C, Rivière J P, Bellara A & Delafond J 1985 *Nucl. Instr. and Meth. Phys. Res.* **B7/8**, 591–596.

Jaouen C, Rivière J P & Delafond J 1987 *Nucl. Instr. and Meth. Phys. Res.* **B19/20**, 549–553.

Jaouen C, Ruault M O, Bernas H, Rivière J P & Delafond J 1987 *Europhys. Lett.* **4**, 1031–1035.

Jenkins M L & English C A 1982 *J. Nucl. Mater.* **108/109**, 46–61.

Jenkins M L, Katerbau K H & Wilkens M 1976 *Phil. Mag. A* **34**, 1141–1153.

Kapinos V G & Bacon D J 1995 *Phil. Mag. A* **72**, 1413–1420.

Kimoto T & Saito T 1994 *J. Nucl. Mater.* **212-215**, 275–280.

Kiritani M, Yoshiie T, Kojima S, Satoh Y & Hamada K 1990 *J. Nucl. Mater.* **174**, 327.

Kirkland E J 1998 *Advanced Computing in Electron Microscopy* Plenum Press, New York.

Kittel C 1966 *Introduction to Solid State Physics* third edn John Wiley & Sons, Inc.

Kizuka T, Mitarai N & Tanaka N 1994 *J. Mater. Sci.* **29**, 5599–5606.

Komarov F F 1992 *Ion beam modification of metals* Gordon and Breach Science Publishers, United States of America.

Kuroda K, Takahashi M, Kato T, Saka H & Tsuji S 1998 *Thin Solid Films* **319**, 92–96.

Larsen K K, Karpe N & Bøttiger J 1992 *J. Mater. Res.* **7**, 861–866.

Leifer K P G 1997 Refinement of parallel electron energy loss spectroscopy, electron diffraction and high resolution TEM techniques and their application to Ni/Ti multilayers and AlGaAs heterostructures Ph.D. Dissertation No. 1635 Swiss Federal Institute of Technology Lausanne.

Lequeux M J 1979 The Influence of Composition on the Structure and Mechanical Properties of the Compound NiAl Ph.D. Dissertation Université de Paris-Sud.

Liebl H 1975 *J. Vac. Sci. Technol.* **12**(1), 385–390.

Liu B X 1985 *Nucl. Instr. and Meth. Phys. Res.* **B7/8**, 547–551.

Liu B X 1987 *Mater. Letters* **5**, 322–327.

Liu B X, Johnson W L & Nicolet M A 1983 *Nucl. Instr. and Meth.* **209/210**, 229–234.

Liu B X, Ma E, Li J & Huang L J 1987 *Nucl. Instr. and Meth. Phys. Res.* **B19/20**, 682–690.

Liu H C & Mitchell T E 1983 *Acta Metall.* **31**, 863–872.

Lu G & Kioussis N 1997 *Mat. Res. Soc. Symp. Proc.* **472**, 21–26.

Machlin E S 1995 *The relationships between thin film processing and structure* Vol. I of *Materials Science in Microelectronics* Giro Press, Croton-on-Hudson, N.Y. 10520.

Mankins W L & Lamb S 1992 *in* H Baker, ed., 'Alloy Phase Diagrams' Vol. 3 ASM International.

Matteson S & Nicolet M A 1983 *Ann. Rev. Mater. Sci.* **13**, 339–362.

Matthews J W, ed. 1975*a* *Epitaxial Growth: Part A* Academic Press, New York.

Matthews J W, ed. 1975*b* *Epitaxial Growth: Part B* Academic Press, New York.

Miracle D B 1993 *Acta Metall. Mater.* **41**, 649–684.

Motta A T 1997 *J. Nucl. Mater.* **244**, 227–250.

Müller S 1997 Elektronenmikroskopische Untersuchungen der Entordnung von Ni_3Al unter Ionenbestrahlung Ph.D. Dissertation Technischen Universität Berlin.

Müller S, Abromeit C, Matsumura S, Wanderka N & Wollenberger H 1999 *J. Nucl. Mater.* **271/272**, 241–245.

Müller S, Jenkins M, Abromeit C & Wollenberger H 1997 *Phil. Mag. A* **75**, 1625.

Nastasi M, Hung L S & Mayer J W 1983 *Appl. Phys. Lett.* **43**, 831–833.

Nastasi M & Mayer J W 1991 *Mater. Sci. Reports* **6**, 1–51.

Nastasi M & Mayer J W 1994 *Radiat. Eff. Def. Sol.* **130-131**, 367–385.

Nastasi M, Williams J M, Kenik E A & Mayer J W 1987 *Nucl. Instr. and Meth. Phys. Res.* **B19/20**, 543–548.

Naundorf V 1999. Private communication.

Nelson R S, Hudson J A & Mazey D J 1972 *J. Nucl. Mater.* **44**, 318–330.

Ng H P, Meng X K & Ngan A H W 1998 *Scripta Mater.* **39**, 1737–1742.

Norgett M J, Robinson M T & Torrens I M 1975 *Nucl. Eng. and Design* **33**, 50–54.

Potter D I 1983 *in* F. V Nolfi Jr, ed., 'Phase transformations during irradiation' Applied Science Publishers Ltd.

Predel B 1991 *in* O Madelung, ed., 'Phase Equilibria, Crystallographic and Thermodynamic Data of Binary Alloys' Vol. 5 Springer-Verlag.

Ramesh R 1992 Crystal Structure Changes in Ni₃Al and its Anomalous Temperature Dependence of Strength Ph.D. Dissertation Universiteit Twente.

Reynaud F 1976 *J. Appl. Cryst.* **9**, 263–268.

Rivière J P, Jaouen C & Delafond J 1987 *Mater. Sci. Forum* **15-18**, 1111–1116.

Robertson I M & Wayman C M 1984 *Met. Trans. A* **15A**, 1353–1357.

Robinson M T 1994 *Radiat. Eff. Def. Sol.* **130-131**, 3–20.

Robinson M T & Torrens I M 1974 *Phys. Rev. B* **9**, 5008–5024.

Rosen S & Goebel J A 1968 *Trans. Met. Soc. AIME* **242**, 722–724.

Schäublin R 1998 CUFOUR user guide (version 1.5).

Schäublin R, Almazouzi A, Osetsky Y N & Victoria M 2000 *J. Nucl. Mater.* **276**, 251–257.

Schäublin R, Dai Y & Victoria M 1998 *in* H Calderón Benavides & M Yacamán, eds, 'Proceedings of the 14th International Congress on Electron Microscopy, Cancún, México' Vol. I pp. 173–174. ISBN 0-7503-0564-9.

Schäublin R, de Almeida P, Almazouzi A & Victoria M 2000 *J. Nucl. Mater.* **283-287**, 205–209.

Schäublin R & Gotthardt R 1996 *Phil. Mag. A* **74**, 593–615.

Schäublin R & Stadelmann P 1993 *Mater. Sci. Eng.* **A164**, 373–378.

Schryvers D, Yandouzi M & Toth L 1998 *in* 'Trinoculaire 98 des Microscopies, Strasbourg-Illkirch' pp. 31–32.

Schulson E M 1979 *J. Nucl. Mater.* **83**, 239–264.

Siegel S 1949 *Phys. Rev.* **75**(12), 1823–1824.

Smialek J L & Hehemann R F 1973 *Met. Trans.* **4**, 1571–1575.

Smith D L 1995 *Thin-Film Deposition: Principles and Practice* McGraw-Hill, Inc.

Spaczér M 1995 Computer simulations of kinetic effects on the evolution of the displacement cascade in ordered intermetallics Ph.D. Dissertation No. 1340 Swiss Federal Institute of Technology Lausanne.

Spaczér M, Almazouzi A, Schäublin R & Victoria M 1997 *Radiat. Eff. Def. Sol.* **141**, 349–362.

Spaczér M, Caro A & Victoria M 1995 *Phys. Rev. B* **52**, 7171–7178.

Spaczér M, Caro A, Victoria M & de la Rubia T D 1994a *Phys. Rev. B* **50**, 13204–13213.

Spaczér M, Caro A, Victoria M & de la Rubia T D 1994b *J. Nucl. Mater.* **212-215**, 164–167.

Spaczér M, Caro A, Victoria M & de la Rubia T D 1995 *Nucl. Instr. and Meth. Phys. Res.* **B102**, 81–85.

Stadelmann P A 1987 *Ultramicroscopy* **21**, 131–146.

Stoeckinger G R & Neumann J P 1970 *J. Appl. Cryst.* **3**, 32–38.

Szpunar J A 1997 *Mat. Res. Soc. Symp. Proc.* **472**, 45–61.

Thomé L, Jaouen C, Rivière J P & Delafond J 1987 *Nucl. Instr. and Meth. Phys. Res.* **B19/20**, 554–558.

Thompson C V 1990 *Ann. Rev. Mater. Sci.* **20**, 245–268.

Thornton J A 1977 *Ann. Rev. Mater. Sci.* **7**, 239–260.

van der Merwe J H 1982 *Phil. Mag. A* **45**(1), 145–157.

Van Dyck D 1998 *Thin Solid Films* **319**, 148–152.

van Gunsteren W F & Berendsen H J C 1990 *Angew. Chem. Int. Ed. Engl.* **29**, 992–1013.

Van Swygenhoven H, Grimmer H, Paschoud F, Victoria M & Hauert R 1994 *NanoStruct. Mater.* **4**, 409–415.

Van Vlack L H 1989 *Elements of Materials Science and Engineering* sixth edn Addison-Wesley Publishing Company.

Victoria M 2000. Private communication.

Victoria M, Baluc N, Bailat C, Dai Y, Luppo M I & Schäublin R 2000 *J. Nucl. Mater.* **276**, 114–122.

Visnov R, Alonso J A & Girifalco L A 1980 *Met. Trans. A* **11A**, 1747–1753.

Was G S & Eridon J M 1987 *Nucl. Instr. and Meth. Phys. Res.* **B24/25**, 557–561.

Window B & Sharples F 1985 *J. Vac. Sci. Technol. A* **3**(1), 10–13.

Wolff I M & Sauthoff G 1996 *Z. Metallkd.* **87**, 111–119.

Wu W T 1996 Structural and Optical Properties of Intermetallic Compounds: Pd-In and Pd-Al Sputtered Thin Films Ph.D. Dissertation No. 1461 Swiss Federal Institute of Technology Lausanne.

Yandouzi M, Toth L & Schryvers D 1998 *NanoStruct. Mater.* **10**, 99–115.

Zhu H, Averback R S & Nastasi M 1995 *Phil. Mag. A* **71**, 735–758.

Zinkle S J & Snead L L 1995 *J. Nucl. Mater.* **225**, 132.

Biography

Pedro Miguel Rodrigues de Almeida was born in Luanda, in 1972. He graduated in engineering physics from the Technical University of Lisbon (IST), in 1995. Since 1996 he has been with CRPP Fusion Technology preparing his Ph.D. in materials physics (radiation damage in solids) at the Paul Scherrer Institute site, in Villigen.

Mr de Almeida has participated in undergraduate experimental physics teaching activities at IST (1993–1996) and has been with the IST Centre for Microsystems as a research engineer (1994–1996) working on the conception and design of a low-jitter A/D channel using sub-sampling for wireless applications. In 1994 he has been a research trainee at the von Karman Institute for Fluid Dynamics, Brussels, working on the design and implementation of a DSP-based hot-wire anemometer.

Mr de Almeida has published in the areas of transmission electron microscopy image simulation of irradiation-induced defects, intermetallic thin film synthesis and characterization, and on the assessment of the order-disorder transformation and microstructure evolution in ion-irradiated intermetallics. Contact him at `pedro@ieee.org`. ∎

Publications

- R. Schäublin, P. de Almeida, A. Almazouzi, M. Victoria, Correlation of simulated TEM images with irradiation induced damage, J. Nucl. Mater. **283-287**, 205–209 (2000);

- P. de Almeida, R. Schäublin, A. Almazouzi, M. Victoria, M. Döbeli, Quantitative long-range order measurement and disordering efficiency estimation in ion-irradiated bulk Ni_3Al using cross-sectional conventional transmission electron microscopy, Appl. Phys. Lett. **77**, 2680–2682 (2000);

- P. de Almeida, R. Schäublin, A. Almazouzi, M. Victoria, F. Lévy, Microstructure and growth modes of stoichiometric NiAl and Ni_3Al thin films deposited by r.f.-magnetron sputtering, Thin Solid Films **368**, 26–34 (2000);

- P. de Almeida, R. Schäublin, A. Almazouzi, M. Victoria, Molecular dynamics of displacement cascades in intermetallics and their TEM image simulation, in Mathematics and Computation, Reactor Physics and Environmental Analysis in Nuclear Applications, Madrid, edited by J. M. Aragonés, C. Ahnert, O. Cabellos, Vol. 2, pp. 1162–1172, 1999. ISBN 84-699-0943-6;

- D. Danailov, D. Karpuzov, A. Almazouzi, P. de Almeida, M. Victoria, Mask-edge distributions produced by 80 keV As^+ ion implantation into Si, MRS Symp. Proc. **438**, 149–153 (1997).

Acknowledgments